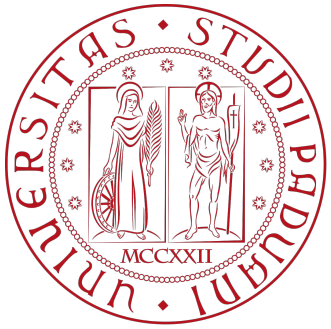

UNIVERSITÀ DEGLI STUDI DI PADOVA

Dipartimento di Fisica e Astronomia "Galileo Galilei"

Master Degree in Astrophysics and Cosmology

Final dissertation

Multiwavelength study of the gamma-ray blazar PKS 1424+240: a neutrino candidate

Supervisor:
Dr. Elisa Prandini

Candidate:
Sara Fogliacco

Co-supervisor:
Dr. Ilaria Viale
Giuseppe Silvestri

Academic Year 2023/2024

Abstract

Aims. The gamma-ray blazar PKS 1424+240 has been recently associated with neutrino emission with the IceCube Observatory, making it an extragalactic neutrino candidate. The observation by MAGIC telescope were triggered by *Fermi*-LAT that reported a high hardness in the spectrum. This thesis is centered around the investigation of a flaring state that took place in 2017, the evaluation of multiwavelength data, and the simulation of emission.

Methods. MAGIC data of the flaring episode have been analyzed, and the results have been compared with MAGIC archival data and data from multiple instrument covering the electromagnetic spectrum from radio up to gamma rays. Afterward, the emission of PKS 1424+240 has been modelled using the `agnpy` software, to confirm past result and evaluate the need to add a hadronic component.

Results. From the comparison with MAGIC archival data of PKS 1424+240, the result of the analysis at very high energy gamma rays is compatible with a flaring state, the event was also detected by *Swift*-XRT. The study of multiwavelength light curves shows that there are two distinct emitting zones, which is a confirmation of previous studies.

Summary

This thesis concerns the study of the very high energy (VHE; E>100 GeV) gamma-ray emission of the blazar PKS 1424+240 observed with the MAGIC telescopes.
Blazars, a subclass of Active Galactic Nuclei (AGN) with jets aligned with our line of sight, show intense, variable emissions across the spectrum. Their Spectral Energy Distribution (SED) features two peaks: the first from electron synchrotron emission, and the second possibly from leptonic or hadronic processes. Hadronic processes could link gamma-ray emission with neutrinos and cosmic rays, though the emission mechanisms remain debated.
PKS 1424+240, a high synchrotron peak BL Lac, is among the most distant VHE blazars known (z=0.603). It has been associated with a neutrino excess by IceCube at a 3.7σ level, suggesting it might be an extragalactic neutrino source, similar to TXS 0506+056. This association arise from analyzing a decade of IceCube data for neutrino hot-spots.
This thesis has three original objectives: (i) the data analysis with MAGIC software, (ii) the multiwavelength data analysis and comparison of the light curves, and (iii) the SED modelling.

The first chapter, Introduction, is given an overview on the fundamental topics required to fully understand this work. The diverse forms of radiation coming from outside the solar system, including cosmic rays, gamma rays, and neutrinos, are delineated alongside their respective detection methodologies. Following this, an overview of jetted AGN and their subclasses is provided to establish a foundational context for examining the focal subject of this thesis, the gamma-ray blazar PKS 1424+240.

The second chapter, The MAGIC Telescopes, include a detailed description of the MAGIC telescopes and their functionalities, both hardware and software. Starting from a characterization of the technical component of the Imaging Array Cherenkov Telescope (IACTs); and eventually, describe the standard data analysis.

The third chapter, MAGIC analysis PKS 1424+240, concerns the MAGIC data analysis of a flaring state of the blazar PKS 1424+240, center of this thesis. Additionally, the obtained results were compared by a cross-check analysis, and with MAGIC archival data, to verifying the consistency of the results.

The fourth chapter, Multiwavelength Analysis PKS 1424+240, is related to the mul-

tiwavelength analysis. In order to have a complete view of the source behavior, data from different instrument were requested. A multiwavelength light curve was built covering the electromagnetic spectrum from the radio band up to the VHE gamma-ray band.

The fifth chapter, Spectral Energy Distribution modelling has the focus on the modelling of the SED of PKS 1424+240. The result obtained by the multiwavelength comparison are used to build a meaningful model that reproduces the source emission. It was chosen to use a simple leptonic model in order to compare and check the result with the past model; and to evaluate if the hadronic component is needed to improve the model.

The last chapter, Conclusions, provides a summary of this work and a perspective that will guide future research on this source.

Contents

1 Introduction **1**
- 1.1 Cosmic Rays . . . 1
- 1.2 Gamma-rays . . . 4
  - 1.2.1 Leptonic Processes . . . 5
  - 1.2.2 Hadronic Processes . . . 9
- 1.3 Neutrinos . . . 12
- 1.4 Detection of Gamma Rays . . . 13
  - 1.4.1 Indirect Detection . . . 16
  - 1.4.2 Direct Detection . . . 20
- 1.5 Active Galactic Nuclei . . . 21
  - 1.5.1 Blazars . . . 23
- 1.6 PKS 1424+240 . . . 25

2 The MAGIC Telescopes **28**
- 2.1 MAGIC Hardware . . . 28
  - 2.1.1 Structure and drive system . . . 28
  - 2.1.2 Mirrors . . . 29
  - 2.1.3 Active Mirror Control . . . 30
  - 2.1.4 Camera . . . 30
  - 2.1.5 Trigger System . . . 31
  - 2.1.6 Weather instrumentation . . . 32
- 2.2 MAGIC software . . . 33
  - 2.2.1 Central Control . . . 33
  - 2.2.2 Automatic Alert System . . . 33
  - 2.2.3 Data and Analysis at the MAGIC site . . . 34
- 2.3 MAGIC data taking . . . 35
  - 2.3.1 Night conditions . . . 35
  - 2.3.2 Pointing configurations . . . 36
- 2.4 Data analysis . . . 37
  - 2.4.1 Monte Carlo γ-ray analysis . . . 37
  - 2.4.2 Low level analysis . . . 38
  - 2.4.3 Intermediate level analysis . . . 41
  - 2.4.4 High level analysis . . . 46

3 MAGIC analysis PKS 1424+240 **51**
3.1 Analysis Period . . . 51
3.2 Crab Check . . . 53
3.3 PKS 1424+240 analysis results . . . 56
3.3.1 Signal Search . . . 56
3.3.2 Spectral Energy Distribution and Light Curve . . . 59
3.3.3 Deabsorbed Spectral Energy Distribution . . . 60
3.3.4 Crosscheck Analysis . . . 62
3.4 MAGIC past observations . . . 64

4 Multiwavelength Analysis PKS 1424+240 **69**
4.1 Radio Band . . . 69
4.2 Optical Band . . . 71
4.3 X-Ray Band . . . 73
4.4 High Energy Gamma-Ray Band . . . 75
4.5 Very High Energy Gamma-Ray Band . . . 77
4.6 Neutrinos . . . 78
4.7 Multiwavelength Light Curve . . . 79
4.7.1 Fractional Variability . . . 80
4.7.2 Multiwavelength Light Curve Interpretation . . . 82

5 Spectral Energy Distribution modelling **84**
5.1 Single-zone Models . . . 85
5.2 Two-zone Models . . . 86
5.3 SED Modelling . . . 89
5.3.1 Software: `agnpy` . . . 89
5.3.2 Modelling of PKS 1424+240 . . . 90

6 Conclusions **96**

Chapter 1

Introduction

This opening chapter provides an overview of the essential topics needed to fully comprehend the content of this work. It outlines the various types of radiation originating from beyond the solar system, such as cosmic rays, gamma rays, and neutrinos, along with the methods used to detect them. Additionally, it offers a summary of jetted Active Galactic Nuclei and their different subclasses, setting the stage for the main focus of this thesis: the gamma-ray blazar PKS 1424+240.

1.1 Cosmic Rays

Primary Cosmic rays (CR) are high energy particles originated from outside the Solar System. CRs are mostly charged particles; protons and nuclei (∼98%), out of which protons represent the majority; plus a minor component of electrons, and anti-matter, (Ave et al., 2008). Electrons can be easily decelerated by local magnetic field, therefore, protons are the dominant component of CRs. **Primary CRs** can be identified by experiment outside the Earth's atmosphere, such as satellite. Although, **secondary CRs** are particle produced in the interaction between the primary CRs and the nuclei in the atmosphere, (Spurio, 2014).

CRs were discovered in the beginning of the 20th century, thanks to the combined studies on the ionized radiation made by Wulf, Pacini and Hess, the latter gave the most significant contribution through balloon experiments, (Spurio, 2014). Hess, in 1912, discovered that the CRs origin was extra-terrestrial, (Hess, 1912), this hypothesis was already suggested by Millikan, who first named these particles *cosmic rays*. The results from Hess were later confirmed by Kolhöster, and Hess was awarded the Nobel Prize in physics in 1936 for the discovery of CRs. Afterward, study of Clay, Rossi, and Compton provided evidence that CRs were charged particles. More specific, positively charged particles, since the *East-West effect*; the variation of CRs intensity with latitude. The discovery of secondary CRs comes later, by Auger, who notices that groups of particles arriving at coincident time on detectors separated by few hundreds meters. This was the first indication of particle induced by a common primary CR, (Longair, 2011).

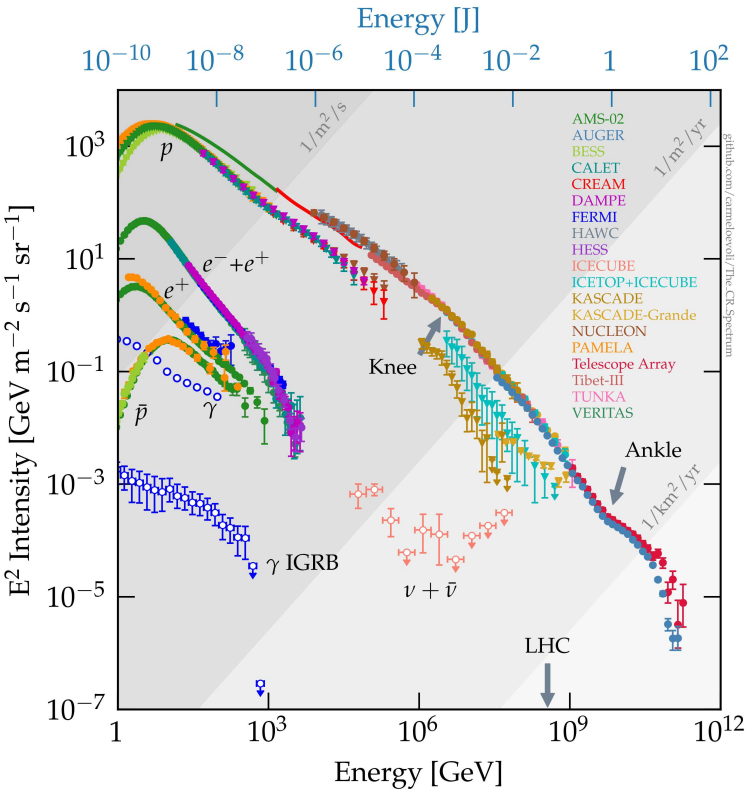

Figure 1.1: The all particles spectrum of CRs. The plot shows the all particles CRs spectrum energy (both GeV and J) vs. flux intensity (GeV m^{-2} s^{-1} sr^{-1}) measured by several experiments. In order to mention the relevant ones for this thesis, the Imaging Array Cherenkov Telescopes H.E.S.S. and VERITAS; the hybrid experiment Auger (fluorescent technique and water Cherenkov tanks); the Extensive Air Showers array HAWK, the neutrino detector (ice Cherenkov tank) IceCube and space detector *Fermi*. The two feature of the spectrum, the knee and the ankle, are highlighted by arrows. It is clearly visible that the flux is steeply falling with increasing energy. The integral flux is defined for three energy range, in the lower energy range is 1 particle m^{-2} s^{-1}, in the intermediate energy range is 1 particle m^{-2} yr^{-1}, and finally, in the higher energy range is 1 particle km^{-2} yr^{-1}. From Evoli (2023).

The CRs' **energy spectrum** ranges between 10^9 eV up to 10^{21} eV, see Fig. 1.1; the Sun contributes with low energy CRs (below the GeV scale), mainly associated with *solar flares*, (Perkins, 2009). However, the lower threshold at 1 GeV is due to the *solar modulation*, since at low energy the magnetic field of the Sun deflects the CRs, (Spurio, 2014).
The all particle non-thermal spectrum can be approximated to a **power-law**:

$$\Phi(E) = K\left(\frac{E}{E_0}\right)^{-\alpha} \qquad \text{particles cm}^{-2}\ \text{s}^{-1}\ \text{sr}^{-1}\ \text{GeV}^{-1} \tag{1.1}$$

$$\Phi(>E) = \frac{KE_0}{\alpha - 1}\left(\frac{E}{E_0}\right)^{-\alpha+1} \qquad \text{particles cm}^{-2}\ \text{s}^{-1}\ \text{sr}^{-1} \tag{1.2}$$

where the *spectral index* α is energy dependent, K is a normalization factor and E_0 is the energy cut usually set at 1-3 GeV. The Eq. 1.1 is known as *differential energy spectrum*, while the Eq. 1.2 is known as *integral energy spectrum*, (Spurio, 2014; Longair, 2011).
Different energy ranges are characterized by different processes of CRs production. In the Figure (1.1) it is possible to see the main structures of the CRs spectrum. At $E \sim 10^{15}$ eV the value of α changes from $\simeq 2.7$ to $\simeq 3.1$, this break is called the **knee**. At higher energy, at the so-called **ankle** $E \sim 10^{18.5}$ eV, the index changes again from $\simeq 3.1$ eV to $\simeq 2.6$ eV. For even higher energy the spectrum has the Greisen, Zaptsepin, Kuzmin (GZK) cut-off $E \simeq 5 \times 10^{19}$ eV, due to the interaction between CRs and the *cosmic microwave background (CMB)*, (Greisen, 1966; Kuzmin and Zatsepin, 1968).
Currently, there is no definite physical explanation for the index variations. The two changes in the steepness of the power law spectrum are thought to be transitions between different kinds of emitters. The knee could be explained by a population of Galactic CR emitters reaching the maximum acceleration capability at 10^{15} eV, the so-called *PeVatron* sources. Above the ankle the contributing source are supposed to be of extragalactic origin, CRs at these energies are not confined to our Galaxy, therefore, it is quite improbable that are generated by Galactic objects, (Spurio, 2014; Longair, 2011).
The **acceleration mechanism** is still under debate, nevertheless, in order to explain the features observed by experimental data, CRs must be accelerated by non-thermal processes. In the human-made accelerator, particles are accelerated by electric field and then deflected by magnetic fields, nonthelsess, no Earth experiment could possibly accelerate to energies comparable to the CRs energies. In astrophysical environment, the matter is in the state of a plasma, no static electric field can be maintained, (Longair, 2011).
Present model for acceleration mechanism are based on recursive stochastic mechanisms in which low energy particle gain energy through numerous interaction with a *shock wave*. Since this, the first order Fermi mechanism seems to satisfy all the criteria, (Rieger et al., 2007). This mechanism, first proposed by Fermi (1949), is based on the acceleration of energetic particles by energy gain due to scattering off magnetic turbulence and/or irregularities.
Moreover, even the sources for CRs production are still unknown, there are candidates for Galactic CRs as Supernova Remnants (SNRs), Pulsar Wind Nebulae (PWNe) and for extra-galactic CRs as Active Galactic Nuclei (AGN).

Charged particles are deflected by intergalactic magnetic fields, therefore, their arrival direction is not linked to the producing source. Neutral particles, instead, are not affected by the magnetic field and their path is directed toward the source. A simplified rappresentation of the particles' trajectory can be seen in Fig. 1.2. Anyhow, the deflection of particles at energy above EeV, **UHECRs (Ultra High Energy Cosmic Rays)**, is less effective since the deflection angle is inversely proportional

to the energy, (Spurio, 2014):

$$\theta_{\text{defl}} \sim 0.5^{\circ}\left(\frac{E}{10^{20}\text{eV}}\right)^{-1}\left(\frac{d}{\text{kpc}}\right)\left(\frac{B}{\mu\text{G}}\right); \tag{1.3}$$

where E and d are respectively the energy and the distance travelled of the particle, and B is the magnetic intergalactic field.
Several studies have been done to find a correlation between UHECRs and nearby source, e.g., AGN; but, the origin of such high energetic particles is still under debate, (Spurio, 2014; Longair, 2011).

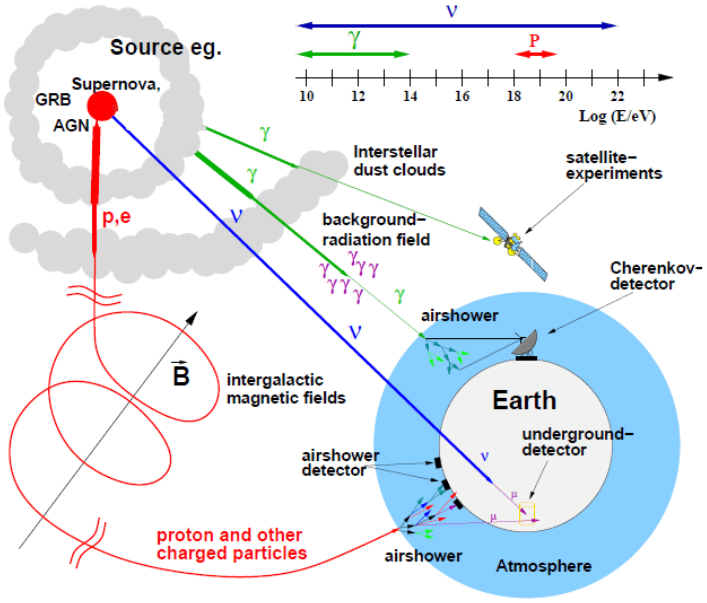

Figure 1.2: The journey of the CRs from their source to their detection. In this simplified model, the source of CRs can be an AGN, a SN or a Gamma Ray Burst. The emitted particles follow different path regarding their charge and type of interaction. Charged particles like protons are deflected by the presence of galactic and intergalactic magnetic field. Instead, electron are strongly suppressed in the vicinity of the source since they are less massive than other charged particle, and therefore, they are subjected to radiative process, e.g., synchrotron emission. Neutral particles are not deflected by the magnetic field, however, photons can interact with the CMB and EBL photons, or they can be absorbed by the interstellar medium. Neutrinos, being weekly interacting particles, can travel to the Earth without undergoing interaction. From Backes (2012).

1.2 Gamma-rays

There exists a correlation between charged CRs and **γ-rays**; since the accelerated CRs are progenitor particles via radiative processes and particle interaction for γ-rays, they share the same origin, (Spurio, 2014). Therefore, the properties of CRs and

γ-rays are closely bound, allowing information about one to be used to deduce details about the other. Differently from charged particle, neutral particle are not affected by the presence of intergalactic magnetic field and their path is not deflected, see Fig. 1.2. Their arrival direction is directly linked to the source, they carry information about the source, and they conserve time information, (Longair, 2011).

The classification of γ-rays is based on their energy:

- **High Energy (HE)** γ-rays: from tens of MeV up to 100 GeV;
- **Very High Energy (VHE)** γ-rays: from 100 GeV up to 100 TeV;
- **Ultra High Energy (UHE)** γ-rays: above 100 TeV.

Below, the MeV energy range, γ-rays are considered low energy.
The production processes for γ-ray can be distinguished into **leptonic** and **hadronic** mechanism, (Rybicki and Lightman, 1986). The leptonic processes are *synchrotron radiation*, *Inverse Compton scattering*, while the hadronic one are *pion decay* and *proton synchrotron radiation*.

1.2.1 Leptonic Processes

Synchrotron radiation

The **synchrotron radiation** is the electromagnetic radiation emitted when relativistic **charged particles**, e.g., electrons, are subject to an acceleration perpendicular to their velocity, see Fig 1.3.
The radiated power is given by the *Larmor formula*, (Rybicki and Lightman, 1986):

$$P = -\frac{dE}{dt} = \frac{2e^2}{3c^3}a^2, \tag{1.4}$$

where a and E are respectively the particle acceleration and its energy. The Eq. 1.4, can be re-written by making explicit the acceleration term:

$$-\frac{dE}{dt} = \frac{2e^2}{3c^3}a^2 = \frac{2e^2}{3c^3}\left(\gamma^2\frac{v^2}{r^2}\right)^2, \tag{1.5}$$

where $\gamma = \left(1 - \frac{v^2}{c^2}\right)^{-1}$ is the *Lorentz factor*, v the particle's velocity and r the accelerator radius.
In astrophysical environments, the radius is determinate by the magnetic field. By using the *Larmor radius*:

$$r_L = \frac{E}{eB} = \frac{\gamma m_e c^2}{eB}, \tag{1.6}$$

the electron energy loss rate reads:

$$-\frac{dE}{dt} = \frac{2e^4}{3m_e^2c^4}c\gamma^2B^2 = \frac{\sigma_T E^2}{4\pi m_e^2 c^3}B^2, \tag{1.7}$$

where in the last equivalence the Thomson cross-section σ_T was introduced.
Finally, the Eq. 1.7 can be written as:

$$-\frac{dE}{dt} = \frac{4}{3}\sigma_T c\beta^2\gamma^2 U_B, \tag{1.8}$$

where $U_B = B^2/8\pi$ is the magnetic energy density.
If the electron velocity is not perpendicular to the magnetic field, the Eq. 1.8 can be generalized by the addition of a $\sin^2\psi$, the motion is then a spiral path at a constant pitch angle ψ.
An observer would see an amplification of the radiation when the accelerated particle has velocity toward the observer itself; generating an effect called *beaming effect*, that corresponds to a pulse of radiation. The beaming effect is relevant when:

$$\theta \simeq \gamma^{-1} \tag{1.9}$$

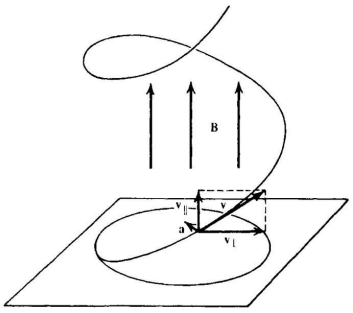

Figure 1.3: Helical motion of a charged particle in a uniform magnetic field. The velocity of the particle is decomposed in the parallel and perpendicular component with respect to the magnetic field, represented by the vertical arrows. The acceleration is perpendicular to the velocity. From Rybicki and Lightman (1986).

The **spectrum** of synchrotron emission results from summing the emission spectra of individual electrons. The synchrotron emission has a characteristic spectrum, and it is found by summing the spectra from the individual electrons, see Fig. 1.4. The flux steadily declines with frequency according to the relation:

$$F \propto \nu^{\alpha} \tag{1.10}$$

where α is the spectral index.

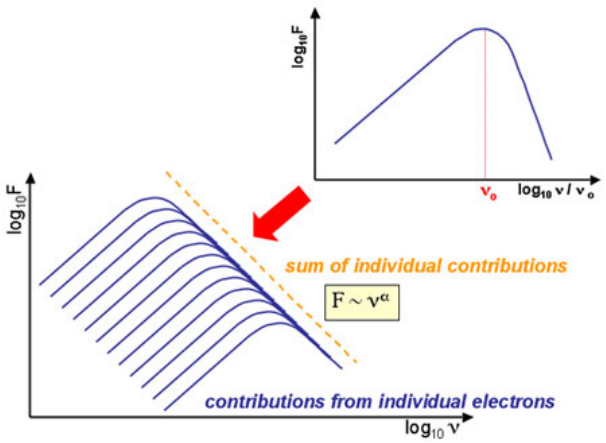

Figure 1.4: The synchrotron emission spectrum follows a power-law decay, and is constructed by adding the contributions from individual electrons. The synchrotron emission has a characteristic spectrum, obtained by summing the spectra from the individual electrons. From Cosmos, the SAO encyclopedia of Astronomy[1].

The mechanism for the **proton synchrotron radiation** is the same as defined above; however, protons are more massive than electrons of a factor ~ 2000. This makes the proton synchrotron radiation less efficient, (Rybicki and Lightman, 1986). Intense magnetic fields ($B \geq 10$ G) or high proton densities are necessary in order to make the proton synchrotron effective.

Inverse Compton scattering

The **Inverse Compton (IC) scattering** is the process in which high energy electrons scatter low energy photons. The photons gain energy as the electrons loses it, (Rybicki and Lightman, 1986). The energy of the photon can be written as:

$$h\nu = \frac{m_e c^2}{1 - \cos\theta + \alpha^{-1}}, \tag{1.11}$$

where ν is the frequency of the photon after the scattering, θ is the angle of the scattered photon, α is the ratio between the rest mass of the electron and the photon energy, (Rybicki and Lightman, 1986).

[1] https://astronomy.swin.edu.au/cosmos/S/Synchrotron+Emission

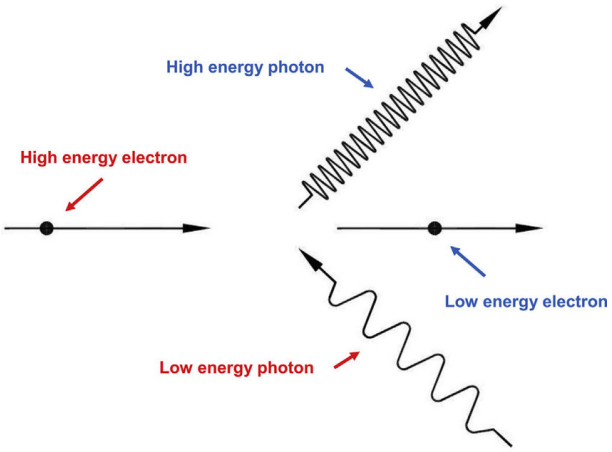

Figure 1.5: Graphical representation of the Inverse Compton scattering. The initial state is represented by red label, the incoming electron has higher energy with respect the photon. In the final state, repainted by blue label, the scattered photon has gained energy while the electron lost it. From Wright (2015).

The cross-section is evaluated at three different regimes, (Spurio, 2014):

- the *Klein-Nishina cross-section* when $\alpha \ll 1$, i.e., the energy of the scattered photon is smaller than the electron rest mass, VHE:

$$\sigma_{KN} \simeq \pi r_e^2 \frac{m_e c^2}{\epsilon}(\ln(2\epsilon) + 0.5); \tag{1.12}$$

- the *Compton cross-section* when $\alpha \geq 1$:

$$\sigma_C = \frac{8\pi r_0^2}{3}(1 - 3\alpha^2 + 9.4\alpha^2 + ...); \tag{1.13}$$

- the *Thompson cross-section* when $\alpha \gg 1$:

$$\sigma_T = \frac{8\pi r_0^3}{3} = 6.65 \times 10^{-25}\text{cm}^2 \tag{1.14}$$

The only relevant case for γ-rays is the one in the Klein-Nishina regime.
For the IC scattering, the *loss rate* of electron can be written as, (Blumenthal and Gould, 1970):

$$\frac{dE}{dt} = \frac{4}{3}\sigma_T c U_{rad} \beta^2 \gamma^2 \tag{1.15}$$

where U_{rad} is the energy density of radiation. This equation is very similar to the one for the synchrotron, Eq. 1.8. The reason for the similarity is that, in both cases, the electron is accelerated by the electric field which it observes in its instantaneous rest-frame. The electron is unaffected by the source of the electric field. For synchrotron radiation, the continuous accelerating electric field arises from the electron's motion through the magnetic field. In the case of inverse Compton scattering, the

electric field is the cumulative effect of all the electric fields from the incident waves, (Blumenthal and Gould, 1970).
The expression for the **spectrum** of the scattered radiation was found by Blumenthal and Gould (1970):

$$I(\nu)d\nu = \frac{3}{16}\frac{\sigma_T c N(\nu_0)}{\gamma^4 \nu_0}\nu\Big[2\nu \ln\Big(\frac{\nu}{4\gamma^2\nu_0}\Big) + \nu + 4\gamma^2\nu_0 - \frac{\nu^2}{2\gamma^2\nu_0}\Big]d\nu \tag{1.16}$$

where ν_0 is the frequency of the radiation field, $N(\nu_0)$ is the number density of photons. The IC spectrum is illustrated in Fig. 1.6.

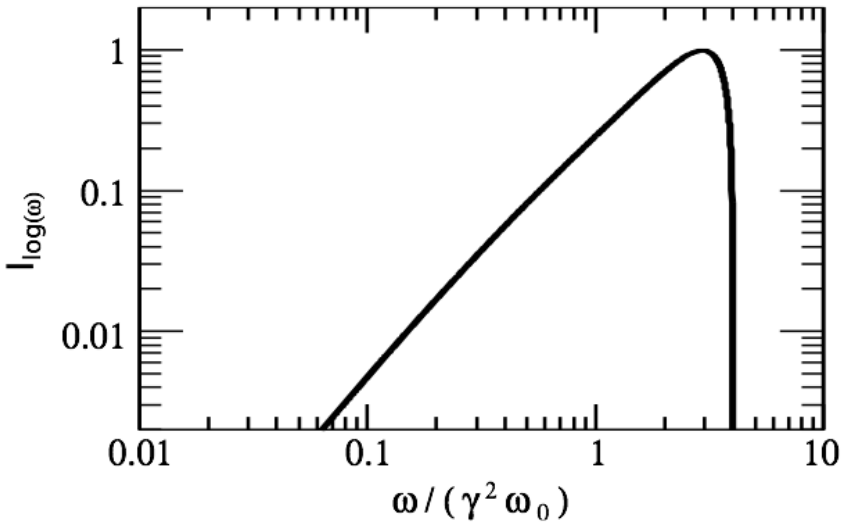

Figure 1.6: The spectrum produced by Inverse Compton scattering of photons by high energetic electrons. For a single high energy electron scattering off low energy photons, the scattered photon spectrum is broad and depends on the angle of scattering. For a distribution of electrons, the resulting photon spectrum can also follow a power law distribution over a range of energies, with the spectral index related to the electron distribution index. From Ertley (2014).

1.2.2 Hadronic Processes

Photo-meson Interactions

The **photo-meson** process involves relativistic protons interacting with low energy radiation, (Longair, 2011). From the photo-meson interaction secondary particle, e.g., pions and muons, are produced. The interaction between a proton and a photon produce a Δ-resonance that decay into hadrons and pions, (Spurio, 2014):

$$p + \gamma \rightarrow \Delta^+ \rightarrow \begin{cases} p + \pi^0 & 2/3 \text{ times} \\ n + \pi^+ & 1/3 \text{ times} \end{cases} \tag{1.17}$$

The produced pion will then decay:

$$\begin{aligned} &\pi^+ \to \mu^+ \nu_\mu \to e^+ + \nu_e + \bar{\nu}_\mu + \nu_\mu, \\ &\pi^- \to \mu^- \nu_\mu e^- + \bar{\nu}_e + \bar{\nu}_\mu + \nu_\mu, \\ &\pi_0 \to \gamma + \gamma. \end{aligned} \tag{1.18}$$

The photons produced by the $\boldsymbol{\pi_0}$ **decay** are highly energetic.
Relativistic protons can produce pions, both charged and neutral, when interact with matter. The probability of pion production is the same for all the three case, meaning that one third are neutral pions. Neutral pions have a very short lifetime ($\sim 10^{-17}$ ns), therefore they decay rapidly in to two high energy photons. They provide the main channel of conversion of the kinetic energy of protons in to high energy γ-rays. In order to achieve this production, the kinetic energy of protons must be at least, (Spurio, 2014):

$$E_{p;kin} = 2m_\pi c^2 \left(1 + \frac{m_\pi}{4m_p}\right) \approx 280\text{MeV}, \tag{1.19}$$

where $m_\pi \simeq 132.97$ MeV is the neutral pion's mass.
Both photons have energy $m_\pi c^2$ in their reference frame, to find the observed energy it is necessary to do a Lorentz boost:

$$E_\gamma = \frac{1}{2} m_\pi c^2 \frac{1 + \beta \cos\theta_\gamma}{\sqrt{1-\beta^2}}, \tag{1.20}$$

where θ_γ is the angle between the direction of the pion and the photon.
Charged pions have a longer lifetime, and the decay leads to the production of muons and neutrinos. The spectra are similar to the neutral pions one. At VHE the interaction timescale can be shorter than the decay timescale. In this situation, charged pions would more probably interact rather than decay; this results with a decrease of neutrinos flux, (Spurio, 2014).
The π^0 decay **spectrum** has a distinct signature of the differential energy spectrum of γ-rays between 100 MeV and 1 GeV produced in hadronic interactions; see Fig. 1.7. The shape of the bump is related to the cross-section of proton-proton inelastic interactions and the energy distribution of non-thermal protons. It is generally considered as a key signature for identification of the hadronic component of radiation, (Yang et al., 2018).

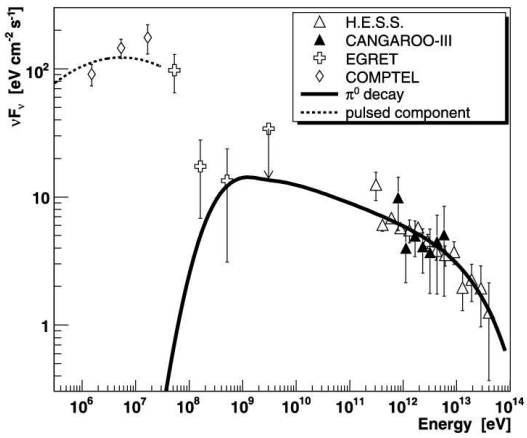

Figure 1.7: Spectral energy distribution and model curve of the neutral pion decay. The solid line represents the best-fit model curve. The study were done with H.E.S.S, EGRET and other experiment. From Nakamori et al. (2008).

Bethe-Heitler pair production

The interaction between relativistic proton and photon, at low energy, is dominated by the **Bethe-Heitler process**, (Kelner and Aharonian, 2008):

$$p + \gamma \rightarrow p + e^+ + e^-, \tag{1.21}$$

the process is allowed when: $\gamma_p \epsilon > m_e c^2$, where γ_p is the proton Lorentz factor, and ϵ the energy of the photon. The $e^{\pm}$ pair produced is energetic enough to initiate a electromagnetic cascade, (Mastichiadis et al., 2005).
The maximum energy of the produced electron (or positron) is given by the kinematics of the process and results, (Kelner and Aharonian, 2008):

$$E_{max,e} = \begin{cases} 4\gamma_p^2 \epsilon & \text{if} m_e c^2 \ll \gamma_p \epsilon \ll m_p c^2 \\ \gamma_p m_p \epsilon & \text{if} \gamma_p \epsilon \gg m_p c^2 \end{cases} \tag{1.22}$$

Therefore, these relations are valid if $\gamma_p \gg 1$ and $\epsilon \ll \gamma_p m_p c^2$, and if $\gamma_p \epsilon \gg m_p c^2$ the total energy of the proton is transferred to a produced lepton.
Considering ultrarelativistic proton, the energy spectrum is given by, Kelner and Aharonian (2008):

$$\frac{dN}{dE_e} = \frac{1}{2\gamma_p^3} \int_{\frac{(\gamma_p + E_e)^2}{4\gamma_p^2 E_e}}^{\infty} d\epsilon \frac{f_p h(\epsilon)}{\epsilon^2} \int_{\frac{(\gamma_p + E_e)^2}{4\gamma_p^2 E_e}}^{2\gamma_p \epsilon} d\omega\omega \int_{\gamma_p^2 + \frac{E_2^2}{2\gamma_p E_p}}^{\omega - 1} \frac{dE_-}{p_-} W(\omega, E_-, \zeta), \tag{1.23}$$

where E_e and E_- are the electron energy, respectively laboratory frame and proton frame; $f_p h(\epsilon)$ is the energy distribution of target photons; p_- is the momentum of the electron in the proton frame; $W(\omega, E_-, \zeta)$ is the cross-section of the interaction; and ω is the energy of the photon in the proton frame.

1.3 Neutrinos

Neutrinos are elementary particles, they were firstly hypothesized by Pauli in 1930 to explain how the β decay could conserve energy, momentum, and spin, (Perkins, 2009). In 1956, the first neutrino was observed in a nuclear reactor, (Cowan et al., 1956); and in 1965 and 1968 were observed the first atmospheric neutrino and the first solar neutrino, respectively, (Dass and Sarma, 1984; Dar et al., 1987). Neutrinos are particles that interact through *weak interaction*, this make the detection non-trivial. Together with γ-rays, neutrinos are neutral messenger that can bring to us important information on the source, (Perkins, 2009).

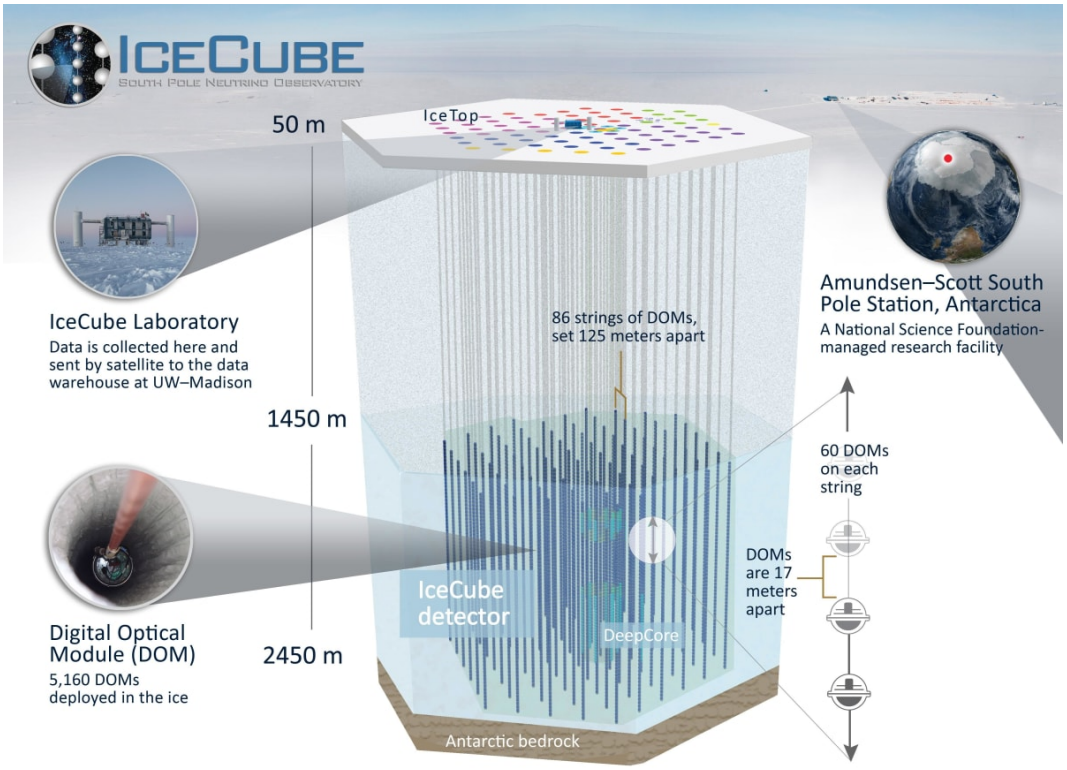

Figure 1.8: IceCube Observatory, South Pole. It is the most important experiment to observe astrophysical neutrino. The image shows a schematic representation of the main structures of the experiment. On the surface (Ice Top) is located the IceCube laboratory, where data are collected. The dimension are reported on the left side of the image, the photomultipliers are located at a depth between 1450 m and 2450 m. From IceCube web page[2].

Nowadays, **IceCube** observatory is the most important experiment to observe astrophysical neutrino. IceCube is operating since 2011, and it is located at the South Pole, see Fig. 1.8. It consists of an array of photomultipliers in 1 km^3 of pure ice,

[2]https://icecube.wisc.edu

this is needed to compensate the small cross-section of neutrino interaction. The detection of VHE (TeV-PeV) diffuse astrophysical neutrino flux by IceCube, opens new question on neutrino production. The first astrophysical neutrino was detected in 2017, (Aartsen et al., 2018), the observed neutrino was associated to the source TXS 0506+056, a blazar. Then, several works have been carried out to identify the sources of these astrophysical neutrinos. After 10 years of time integrated data analysis, two other candidates emerged: the Seyfert galaxy NGC 1068 and the blazar PKS 1424+240, (Aartsen et al., 2020; Abbasi et al., 2021, 2022).
PKS 1424+240 and TXS 0506+056 share different similarities, that will be illustrated in a further section, see Sec. 1.6.

1.4 Detection of Gamma Rays

The detection technique can be **direct** or **indirect**, (Longair, 2011).
Direct detection must be done by satellites orbiting around the Earth, collecting primary CRs. However, since the number of particle decreases rapidly with increasing energy, the collection area of satellites is not large enough to collect CRs with energies above 100 GeV. This limit on the area of detector in orbits is due to the transport mechanism and cost of the detector. The decreases of number of particles is related to the power-law energy spectrum. At energy $\sim 10^9$ eV, the integral flux is $\sim$1000 particles cm^{-2} s^{-1}; while at energy $\sim 10^{20}$ eV, the integral flux is $\sim$1000 particles km^{-2} century^{-1}. Therefore, direct detection is not possible for such energies, (Spurio, 2014).
To collect CRs above 100 GeV are used ground-based telescope based on the production of **Cherenkov light** emitted by secondary CRs. The indirect detection from ground is made by ground-based instruments, divided in two kinds: **Imaging Atmospheric Cherenkov Telescopes** (IACTs) and **Extensive Air Showers arrays** (EAS), (Spurio, 2014).

Cherenkov Radiation

The **Cherenkov radiation** is a beamed pulsed light in the UV/optical band. It occurs when charged particles in a dielectric medium move faster than the velocity of light in that medium. The radiation is emitted along a cone, characterized by an *opening angle* θ_C, (Spurio, 2014):

$$\cos\theta_C = \frac{1}{\beta n(\lambda)} \qquad \beta = \frac{v}{c} \tag{1.24}$$

the refraction index n depends on the wavelength λ of the Cherenkov light emitted. The opening angle has a maximum when $\beta = 1$, and the Cherenkov radiation is relevant if $n > 1$, see Fig. 1.9. This radiation was first detected and studied by Cherenkov (1937).

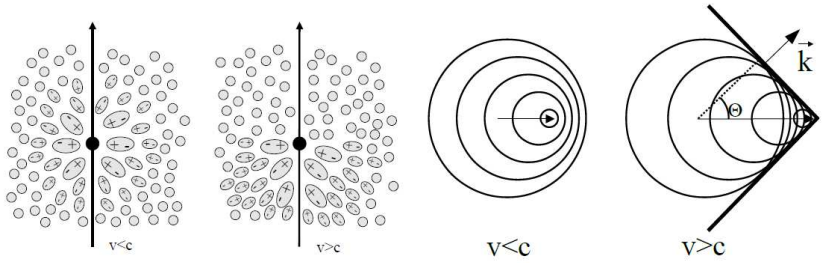

Figure 1.9: Simplified illustration of Cherenkov effect. Left: polarized medium by a particle with velocity v. Right: Construction of Cherenkov wave-front, the opening angle θ is linked with the velocity and the refraction index as mentioned in Eq. 1.24. the Cherenkov radiation is relevant when $n > 1$. From de Naurois and Mazin (2015).

The number of photons produced per unit path length dx and per unit energy interval dE (or equivalently wavelength interval $d\lambda$ by a particle with charge $Z_p e$ at the maximum angle is given by the formula, (Spurio, 2014):

$$\frac{d^2N_{ph}}{dEdx} = \frac{2\pi\alpha Z_p^2}{hc}\sin^2(\theta_c) \approx 370\sin^2(\theta_c(\lambda)) \quad \text{eV}^{-1}\ \text{cm}^{-1}, \tag{1.25}$$

or equivalently:

$$\frac{d^2N_{ph}}{d\lambda dx} = \frac{2\pi\alpha Z_p^2}{\lambda}\sin^2(\theta_c). \tag{1.26}$$

Most of the photons are seen in blue/violet and UV band. The Cherenkov photon density detected on the ground is proportional to the energy of the primary γ-ray photon. Indeed, this relation is fundamental to reconstruct main features of the incoming γ-ray, (Perkins, 2009).

Extensive Air Showers

When particles of CRs interact with the atmospheric nuclei, a cascade of particles is generated. There are two types of Extensive Air Showers (EAS), depending on the nature of the primary particle that initiates the process; the **electromagnetic showers (EM)** and the **hadronic showers**, (Spurio, 2014; Longair, 2011).

A incoming photon, or electron/positron, generates an EM shower; the main emission mechanisms in the cascade are **pair production** of $e^{\pm}$ by the conversion of high energy photons, and **bremsstrahlung emission** when $e^{\pm}$ interact with the Coulomb field of the nuclei, producing a photon. The cascade propagate through the atmosphere via these processes, then, it stops when a *critical energy* E_c is reached and the energy of the secondary particle is dissipated via ionization or excitation. In air at standard condition (NTP[3], temperature 20° and pressure 1 atm) the value of E_c is roughly 80 MeV. Below this limit, radiation energy losses dominate. The fractional

[3]Normal Temperature and Pressure

energy loss due to bremsstrahlung can be defined as follows, (Spurio, 2014):

$$\frac{1}{E}\frac{dE}{dx} \simeq -\frac{1}{X_0}, \tag{1.27}$$

where X_0 is the radiation length, its value depends on the material, e.g., is ∼300 for air at NTP. For bremsstrahlung process, it corresponds to the mean distance travelled by an electron before reducing its energy to $1/e$ of its initial value. Instead, for pair production, the radiation length $X_{0,pp}$ is the average path after which a photon is converted into a $e^{\pm}$ pair, it is linked to the radiation length of bremsstrahlung radiation, (Spurio, 2014):

$$X_{0,pp} \simeq \frac{9}{7}X_0. \tag{1.28}$$

The *Heitler model*, (Heitler, 1936), is an approximated model to describe the EM cascade. It reproduces well the longitudinal development of the cascade, but it overestimates the final number of charged particles since it does not take into account possible multiple scattering of $e^{\pm}$, energy losses by ionization and annihilation, (Longair, 2011). A simplified illustration of a EM shower is shown in Fig. 1.10.

The hadronic shower is, instead, initialized by hadrons, i.e., relativistic protons or nuclei. The hadronic shower is more complex than the EM shower, the number of secondary particles is larger and the interactions are governed by strong force, (Perkins, 2009). A modified version of the Heitler model can be used to describe the cascade. Primary hadrons produce pions, kaons, and light baryons. Pions are the main product (∼ 90%), the neutral pion (π^0) decays rapidly, decaying time of the order of 10^{-17} s, in two photons that initiate a secondary EM shower, while the charged pions ($\pi^{\pm}$) have a *longer* lifetime, order of 10^{-8} s, undergo further collision generating other pions, (Spurio, 2014). Once the critical energy is reached and the interaction timescale of the pions is longer than the decaying one and as result muons are produced. The value of E_c for these processes is around 1 GeV. A small fraction of high energetic muons decay into neutrinos, however, most muons reach the detector (Spurio, 2014). A simplified illustration of a hadronic shower is shown in Fig. 1.10. EM and hadronic showers develop differently, the hadronic one produce more secondary particles, the width of the shower is larger, and the propagation time is longer. These differences are essential to distinguish them, (Spurio, 2014).

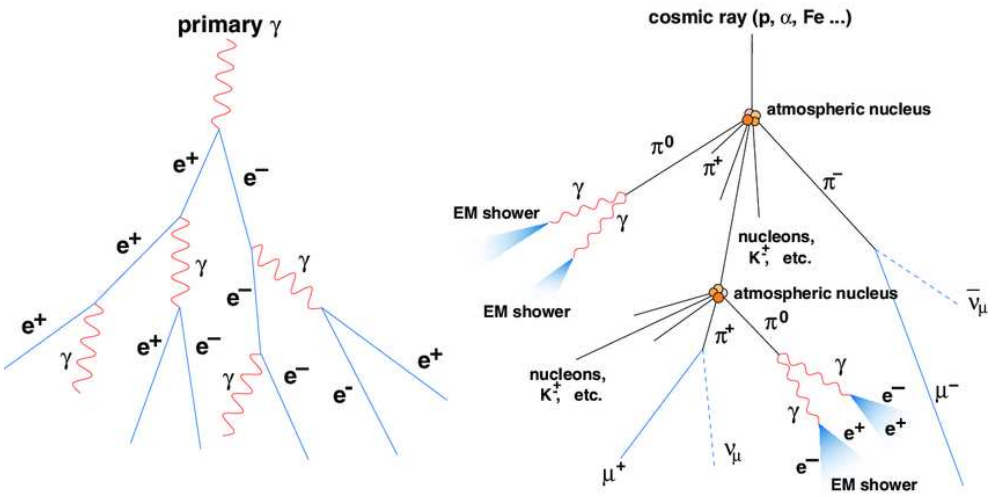

Figure 1.10: Schematic model of shower development: EM shower (left) initialized by a photon (γ) and purely composed of electron-positron pairs ($e^{\pm}$) and photons; the only two processes considered are the pair creation and the bremsstrahlung radiation. Hadronic shower (right) originated by a hadronic particle (proton or nucleus) producing several secondary particles: pions ($\pi^{\pm,0}$), muons ($\mu^{\pm}$), neutrinos (ν), photons, kaons ($K^{\pm}$), etc. From López-Oramas (2015).

1.4.1 Indirect Detection

Imaging Atmospheric Cherenkov Telescopes

Imaging Atmospheric Cherenkov Telescopes (IACTs) are *ground based instrument* that can detect the Cherenkov light emitted by the showers induced in the atmosphere. The light can be collected to generate an image of the shower, from which it is possible to study the nature and the main feature, e.g., energy and incident direction, of the primary particle. The detection technique is called **imaging technique**, and it allows the indirect detection of γ-rays, (Spurio, 2014; Longair, 2011). Currently, there are three major IACT fully operative: **VERITAS (Very Energetic Radiation Imaging Telescope Array System)** located in Arizona, see Fig. 1.12, **H.E.S.S. (High Energy Stereoscopic System)** located in Namibia, see Fig. 1.12, and **MAGIC (Major Atmospheric Gamma-ray Imaging Cherenkov)** located on the Canary Island; see Ch. 2 dedicated to MAGIC telescopes and MAGIC analysis. The new generation of IACTs is at development stage, the **Cherenkov Telescope Array Observatory (CTAO)** is planned to be divided into CTAO-south in Chile and CTAO-north on the Canary island.

To be efficient, an IACT must have a large reflector (diameter of several meters) to collect enough Cherenkov photons. The collected photons are focused on a camera composed by an array of photomultiplier tubes (PMTs). To have high accuracy in the producing of the shower image, numerous PTMs are required. Additional, PTMs must have a fast, timely response in order to catch the fast Cherenkov flashes, (Spu-

rio, 2014; Longair, 2011).
In order to detect Cherenkov light, IACTs have to operate during night when the contribution of the Night Sky Background (NSB) is low. Since all this requirement, IACTs are low duty cycle instruments. An IACT has a relatively small field of view (order of $\sim 5°$) meaning that to be observed a source has to be directly pointed, (Spurio, 2014). Fig. 1.11 shows a simplified representation of the imaging atmospheric Cherenkov technique.

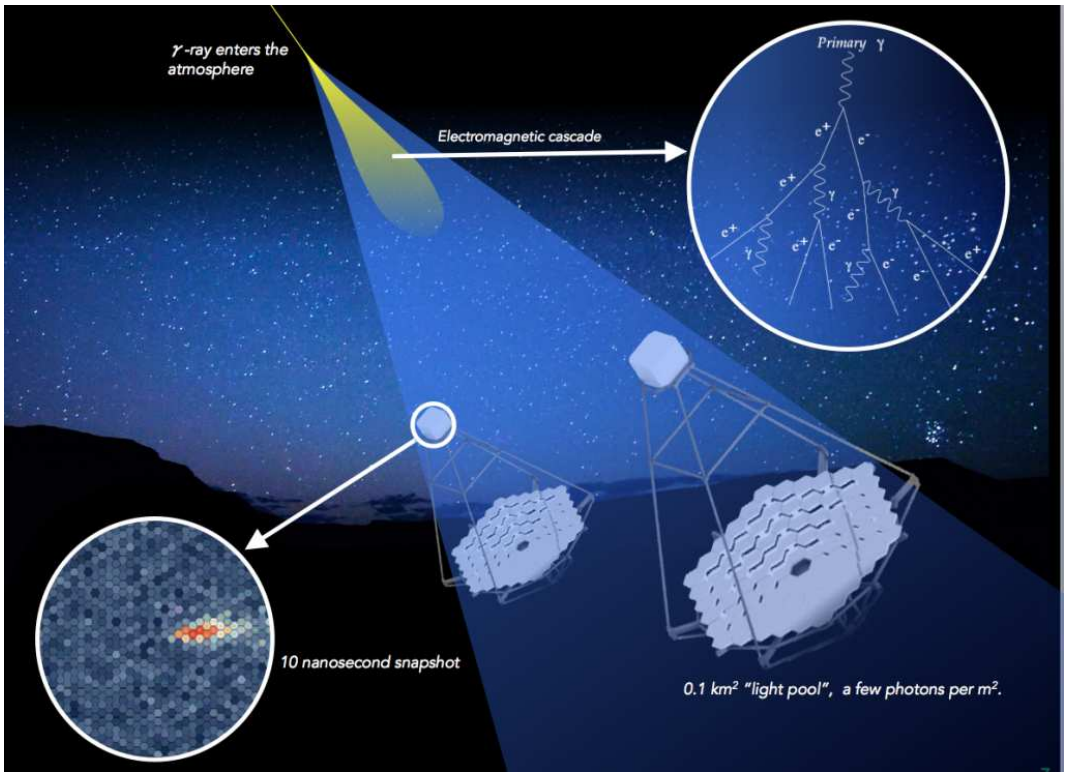

Figure 1.11: Scheme of the imaging atmospheric Cherenkov technique. A γ-ray photon enter the atmosphere, initializing a EM cascade, the charged particles produced in the shower emit Cherenkov light which is detected by the telescope. IACTs can work only during dark time. From CTAO web page[4].

The more relevant part of the detection for imaging technique is the discrimination between the γ-ray signal and the background. The stereoscopic technique is an improvement on the reconstruction and discrimination, since an array of telescope provides different perspectives of the same shower. This addition also improves the geometrical reconstruction of the shower, (Spurio, 2014).
The prevalent background contribution is due to a large distribution of hadrons arriving isotopically into the atmosphere and generate hadronic showers. The hadronic events are three order of magnitude more than the γ-ray events. For this reason, hadrons are a strong source of background. Nevertheless, hadronic shower produce

[4]https://www.ctao.org

irregular e wide images, while γ-ray showers create an elliptical and narrow images. This difference and the previously mentioned difference between γ-ray cascade and hadronic cascade are fundamental for the *γ/hadronic separation*. Moreover, also muons are a source of background, but they are rejected due to the characteristic *muon-ring* that they display on the camera plane. Unfortunately, not all the background can be removed; cosmic $e^{\pm}$ initialize EM shower that are not distinguishable from those produced by γ-rays.
Lastly, the performance of IACTs is related to the observational condition, since they use the atmosphere for the detection, (Longair, 2011).

Figure 1.12: Two of the IACTs mentioned. Top image: the H.E.S.S telescope, located in Khomas Region, Namibia. From H.E.S.S web page[5]. Bottom image: VERITAS, located in Arizona, USA. From VERITAS web page[6].

Extensive Air Shower Arrays

The indirect detection made by ground-based instrument count also **EAS arrays**, (Spurio, 2014). Differently from IACTs, EAS arrays detect via *particle sampling technique*. Currently, the main working EAS are **HAWC (High Altitude Water Cherenkov** experiment located in Mexico, and **LHAASO (Large High Altitude Air Shower Observatory** located in China, see Fig. 1.14.

[6]https://www.mpi-hd.mpg.de/hfm/HESS/pages/about/telescopes/
[6]https://veritas.sao.arizona.edu

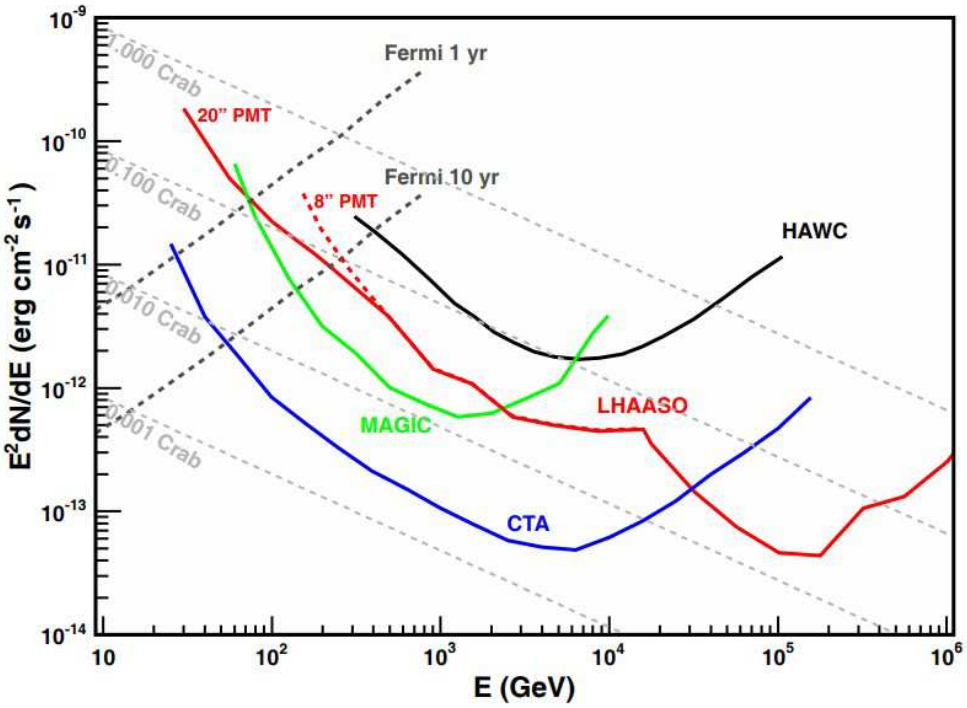

Figure 1.13: Comparison of differential sensitivity (multiplied by E^2) of IACTs and EAS to a Crab-like point γ-ray sources on 50h of observation. The Crab nebula data obtained by different detectors such as MAGIC, HAWC, LHASSO, are taken into account, and the spectral index of -2.6 is extrapolated and extended to 1 PeV. From Zhen et al. (2022).

These type of detectors measure the secondary charged particles that reach the ground level. The detector array covers a huge area $\sim 10^4$-10^5 m^2 and must be installed at high altitude (over 4000 m) in order to collect more charged particles. The type of particle samplers are usually scintillator counters, water Cherenkov tanks and resistive-plate chambers. The threshold for energy is of the order of TeV, higher than IACTs, this is due to the fact that only high energy showers produce a significant number of particles that can reach the ground level, (Longair, 2011).
The discrimination method to separate γ events from the background is based on the reconstructed shower shape or on the muon content. This method is quite limited since particle samplers can access only to the shower's tails. Differently from IACTs, these instrument have a duty cycle that is almost 100%, a large field of view ($\sim$ 2 sr) and a huge effective area given by the spread of detectors' position. Since the long duty cycle and large field of view, EAS arrays can operate as all-sky monitor. While, due to the large effective area, EAS arrays have more sensitivity than IACTs at in the TeV region, (Spurio, 2014).
The Fig. 1.13 shows a comparison of differential sensitivity of IACTs and EAS to a Crab-like point γ-ray sources, (Zhen et al., 2022).

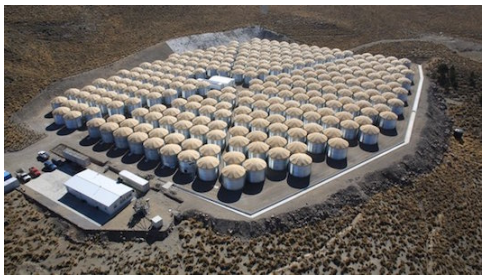

Figure 1.14: Examples of EAS experiment. Left image: the HAWC observatory, located in Sierra Negra volcano, Mexico at an altitude of 4100 m. From HAWC web page[7]. Right image: LHAASO, located in Sichuan Province, China at an altitude of 4410 m. From LHAASO web page[8].

1.4.2 Direct Detection

The Earth's atmosphere is opaque for energy regions that differs from optical, infrared and part of the radio energy bands. This fact implies that the direct observation of CRs and γ-rays is not possible from the ground. This radiation is absorbed by the atmosphere and attenuated. A space instrument is needed to catch direct information on high energy CRs and γ-rays, (Spurio, 2014; Longair, 2011).

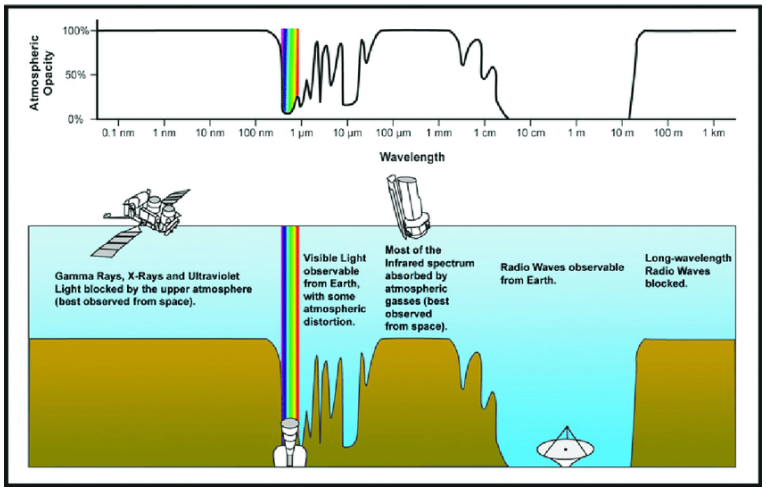

Figure 1.15: Opacity of the Earth's atmosphere, the detection by ground-based telescope is possible only for radio, infrared and optical band. The detection must be done by space telescope for all the other energy band. In this diagram, the brown curve shows how transparent the atmosphere is at the given wavelength to radiation from space. The major windows are at visible wavelengths (marked by the rainbow) and at radio wavelengths from about 1 mm to 10 m. From ESO web page[9].

[8]https://www.hawc-observatory.org
[8]http://english.ihep.cas.cn/lhaaso/

The detection of γ-rays require special instruments, a classical telescope for optical detection cannot be used. The detection techniques are based on the following processes(Spurio, 2014; Longair, 2011):

- **Photoelectric effect:** when photons hit a metal surface, electrons can be emitted. The emitted electrons are called photoelectrons. This process is dominant in the range 0.1-0.3 MeV. Detectors use scintillator counters and solid state detectors.
- **Compton scattering:** photons are scattered by electrons, resulting in a decrease in energy of the photons and a corresponding increase in the energy of the electrons. This process is dominant in the range 0.5-10 MeV. Instrumentation consists in two detector layers, a converter and an absorber.
- **Pair production:** an high energy photon is converted into a electron-positron pair. This process is dominant above 30 MeV. Detectors have a converter region where γ interacts, a tracker that provide the direction of $e^{\pm}$ and a loss estimation for energy, and a calorimeter.

Since the CRs are composed mostly of charged particle, a γ-ray satellite must have an anti-coincident system, in order to suppress CR background. However, the small effective area that characterize satellites makes impossible the detection of VHE γ-rays. Currently, ***Fermi*-LAT** is the most performant instrument, even so, it has a limit at ~ 300 GeV, (Longair, 2011).

1.5 Active Galactic Nuclei

Active Galactic Nuclei (AGN) are an extremely bright central region of a galaxy that is dominated by the light emitted by dust and gas as it falls into a black hole. They are composed of, (Longair, 2011):

- a central **Supermassive Black Hole (SMBH)** with mass between 10^6-10^{10} $M_\odot$;
- an **Accretion Disk** of matter gravitationally attracted to the central SMBH;
- an **X-ray Corona**, whose origin is still under debate. It is likely a hot layer or a collection of highly active clustered regions within the inner part of the accretion disk;
- a **Dusty Torus** that blocks the radiation coming from the center and re-emits is in infrared wavelength;
- a **Broad Line Region (BLR)**, a zone with small clouds and relatively dense ($\sim 10^8$ cm^{-3} at high speed $\sim 10^3$ km s^{-1} located at $\sim 10^{12}$-10^{15} km from the center. It is responsible for the broad and mainly optical emission lines detected;

[9] https://www.eso.org/public/images/atm_opacity/

- a **Narrow Line Region (NLR)**, a zone with less dense clouds (10^3-10^6 cm^{-3}) located at $\sim$ 100 pc from the center, responsible for the narrow emission lines;
- around 10% of AGN have a jet of relativistic particles, pointed in two opposite direction perpendicular to the plane on which the accretion disk lies, they are called **jetted** AGN.

The AGN population is composed of different type of sources, that are very luminous $L_{\rm bol} \sim 10^{48}$ erg s^{-1} and powerful non-explosive sources, making them visible up to very high redshift; have small emitting region in most bands implying high energy density; have strong evolution of the luminosity functions; and have a detectable emission covering the whole spectrum, from radio up to VHE, Padovani et al. (2017).
In the Unified Model of AGN, by Urry and Padovani (1995), these objects are classified by their *radio-loudness* and their optical spectra, if both BLR and NLR are visible they are classified as *Type I*, while if the BLR is not present or weak they are *Type II*. However, this classification become outdated and obsolete. The nowadays used classification is from Padovani et al. (2017), the distinction is between **jetted** and **non-jetted** AGN.
Inside the jetted AGN family, it is possible to distinguish between:

1. **Blazars**: jetted AGN having the jet pointing directly towards the Earth or with small angle ($<30°$); characterized by extreme variability. Subsequently divided into *BL Lacertae (BL Lacs) objects* and *Flat Spectrum Radio Quasars (FSRQs)*; see Sec. 1.5.1 for more details.
2. **Radio Galaxies**: jetted AGN having the jet oriented at large angles with respect to the line of sight ($>30°$); characterized by strong emission in the radio band due to the interaction of high energy particle with the magnetic field. Subsequently divided into *Fanaroff-Riley I* and *Fanaroff-Riley II* depending on the luminosity of the jets.

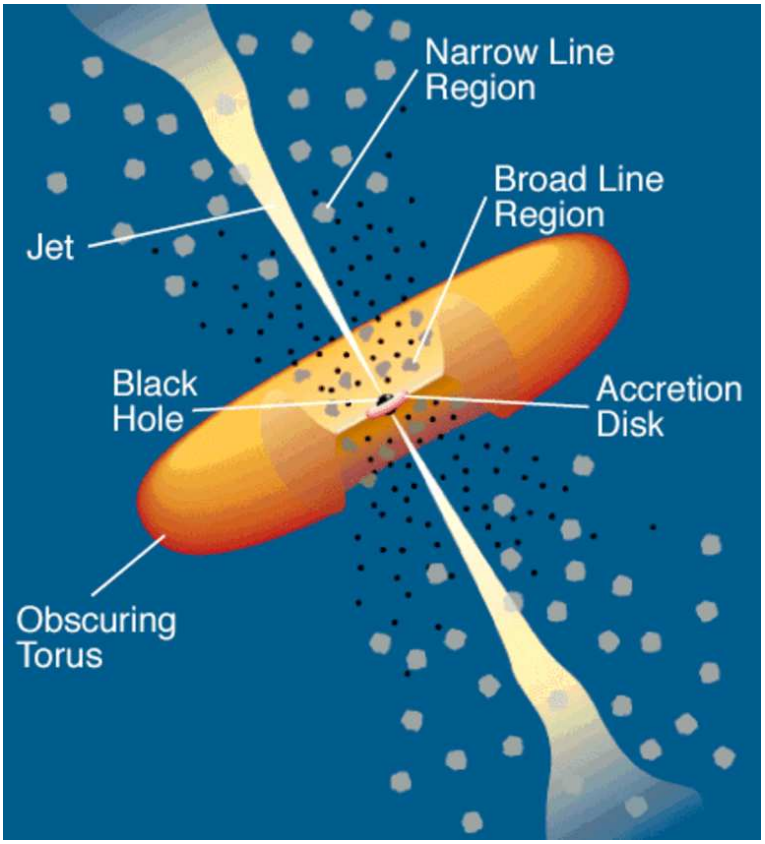

Figure 1.16: Structure of AGN. All the structures defined are illustrated: the SMBH is surrounded by the accretion disk; the BLR, the NLR and the dusty taurus are present, and the jets are perpendicular to the accretion disk plane. As mentioned above, a blazar is seen with the jet pointing towards the observer, while a radio galaxy presents a larger angle of inclination. From Fermi gamma-ray Space Telescope web page[10].

1.5.1 Blazars

Blazars are a subclass of AGN, what makes them peculiar is the viewing angle; the jet is pointed toward the observer, (Padovani et al., 2017). Depending on the characteristic emission, blazar are divided into **FSRQ** and **BL Lacs**. The FSRQ spectrum shows a two-peak structure, evidence of BLR and NLR, and a thermal spectrum is associated with the accretion disk. While, BL Lacs shows as well the two-peak structure, but there is no evidence of emission and/or absorption lines, and the emission is characterized by strong optical polarization and rapid variability. When a **flare state** occurs, the flux varies quickly over a short time, and the luminosity can reach a value 40 times higher than the average, Longair (2011).

[10]https://fermi.gsfc.nasa.gov

The **Spectral Energy Distribution (SED)** has a double-peaked shape, see Fig. 1.17, the first peak is associated to **synchrotron emission**, and it is located at lower frequency 10^{12}-10^{15} Hz, while the second peak origin is more complex to define, it can be related to **leptonic process** such as *synchrotron-self Compton (SSC)* or *External Compton (EC)*; or to **hadronic process** such as *proton synchrotron*, and it is located at higher frequency 10^{21}-10^{25} Hz, Longair (2011).

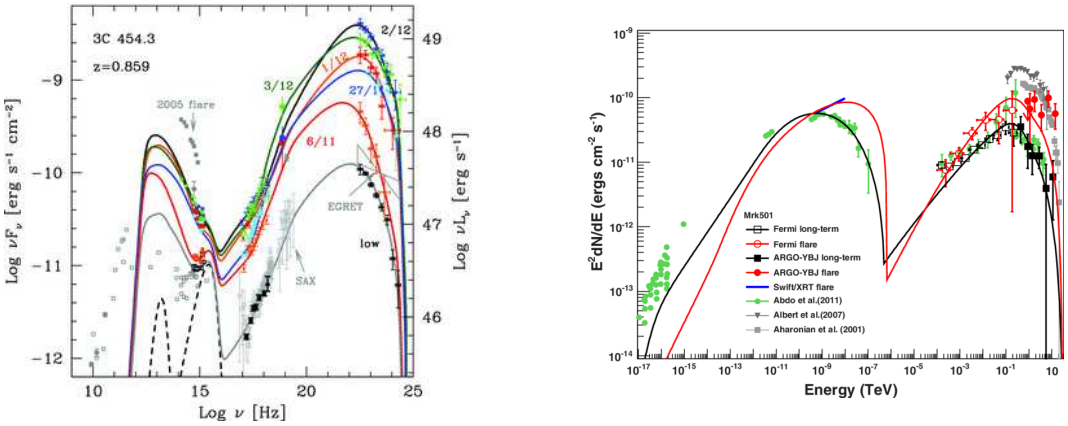

Figure 1.17: Two examples of a blazar SED and comparison between a FSRQ and a BL Lac object. Left: 3C454.3, a very luminous FSRQ with high redshift (z=0.859), from Bonnoli et al. (2010). Right: Mrk 501 a VHE BL Lac object HBL (z=0.034), from Bartoli et al. (2012). For both the example, the doubled-peak shape is clearly distinguishable; the low energy bump is related to the synchrotron emission, while the high energy bump has a still debated origin, the SSC or the EC are the more plausible leptonic mechanisms.

A further classification is based on the position of the synchrotron peak, (Padovani et al., 2017):

- **Low-synchrotron peak Blazar (LBL)** $\nu_{\rm synch}^{\rm peak} < 10^{14}$ Hz;
- **Intermediate-synchrotron peak Blazar (IBL)** $10^{14} < \nu_{\rm synch}^{\rm peak} < 10^{15}$ Hz;
- **High-synchrotron peak Blazar (HBL)** $10^{15} < \nu_{\rm synch}^{\rm peak} < 10^{17}$ Hz
- **Extremely-high-synchrotron peak Blazar** $\nu_{\rm synch}^{\rm peak} > 10^{17}$ Hz.

Because of their similar continuum properties, BL Lacs and FSRQs are collectively called blazars, due to this fact there are hypotheses on their connection. Three main theory were proposed, (Urry and Padovani, 1995): (i) FSRQs evolve into BL Lacs, (ii) FSRQs and BL Lacs are different manifestations of the same physical process, and (iii) BL Lacs are gravitationally microlensed FSRQs. The original **blazar sequence** was proposed by Fossati et al. (1998), as an attempt to identify observational properties in the SED of blazars, see Fig. 1.18; it was the first systematic study of the SED of blazars including γ-ray data above 30 MeV.

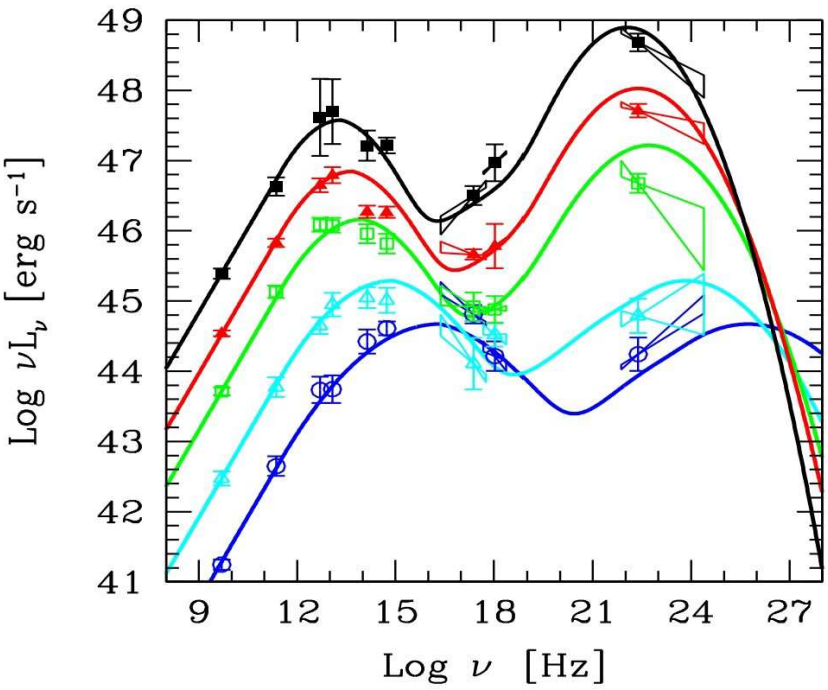

Figure 1.18: The blazar sequence, constructed with the 126 blazars belonging to complete flux limited radio and X-ray samples of blazars. From Fossati et al. (1998); Donato et al. (2001); Ghisellini et al. (2017)

1.6 PKS 1424+240

This thesis project is related to the study and analysis of the blazar PKS 1424+240 via MAGIC telescopes, this section is an overview of the main characteristic of this source.

PKS 1424+240 is a blazar classified as HBL BL Lac Object having the synchrotron peak around 10^{15} Hz, located at:

$$\text{R.A.} = 14^{\text{h}}27^{\text{m}}00^{\text{s}} \qquad \text{Dec} = +23^{\text{d}}47^{\text{m}}40^{\text{s}}.$$

It is a very distant BL Lacs object, with a redshift of $z = 0.603$, (Goldoni, 2021). The Fig. 1.19 shows the SED built with archival data of PKS 1424+240, from Firmamento web page[11].

It was detected, at first, as a radio source in 1977, (Condon et al., 1977), and it was observed by the National Radio Astronomy Observatory (NRAO). Later in 1988, it was classified as blazar, (Impey and Tapia, 1988), from optical polarization studies, and then, the polarization result was verified and reported, and a non-thermal X-ray radiation, (Fleming et al., 1993). These studies brought to light the evidence of variable and intrinsically polarized optical emission produced by the object and the presence of a non-thermal radiation in the X-ray band.

[11] https://firmamento.hosting.nyu.edu/home

The source was finally detected at VHE by VERITAS, (Acciari et al., 2009), and by the MAGIC Collaboration, (Teshima, 2009). The γ-ray emission of PKS 1424+240 was not detected by EGRET (Energetic Gamma Ray Experiment Telescope) but was observed with the *Fermi*-LAT pair-conversion.

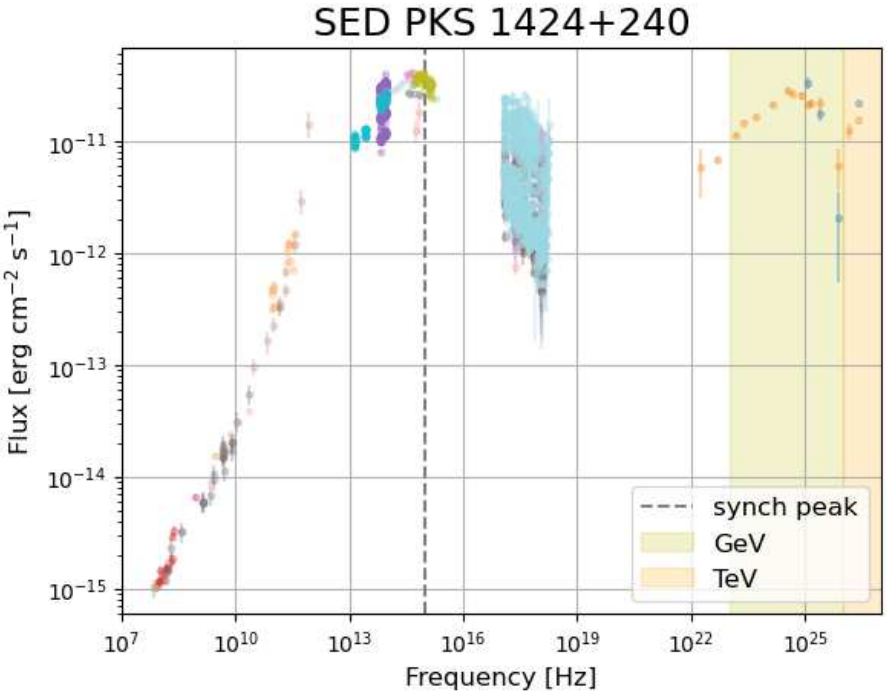

Figure 1.19: SED of PKS 1424+240 built with archival data, each color is associated to a different catalog. The position of the synchrotron peak is highlighted by a dashed line around 10^{15} Hz, while the VHE region is highlighted with yellow (GeV) and orange (TeV) in order to define the MAGIC window of observation. Data retrieved from Firmamento web page[12].

PKS 1424+240 more interesting characteristic is its association with VHE neutrino emission. It is the second most significant neutrino candidate source in the Northern sky seen by IceCube, with local significances of 3.7 σ (while NGC 1068 has 4.2σ, and TXS 0506+056 has 3.5 σ), (Aartsen et al., 2020; Abbasi et al., 2021, 2022). As it was said in the Sec. 1.3, other sources share the same peculiarity; in particular, there are several similarities between PKS 1424+240 and TXS 0506+056, see Fig. 1.20. Beside being both BL Lacs there are other commonalities, (Padovani et al., 2022), the more important are:

- They are both HBLs, having $P_{1.4\mathrm{GHz}} \sim 1.5 \times 10^{26}$ W Hz^{-1} and $L_\gamma \sim 2.9 \times 10^{46}$ erg s^{-1}; however, TXS 0506+056 is ∼3-6 time less powerful.
- The low-energy parts of the SEDs are almost identical, up to the synchrotron peak, while there are differences in the X-ray and γ-ray bands.

[12] https://firmamento.hosting.nyu.edu/home

The main differences are the distance, TXS 0506+056 (z=0.336) is much closer with respect to PKS 1424+240 (z=0.603); and the SED at X-ray and at γ-ray energies. The blazar TXS 0506+056 is associated the first observed astrophysical neutrino, (Aartsen et al., 2018); while the link with PKS 1424+240 is a result of a time integrated data analysis, (Aartsen et al., 2020). This difference lead to a predilection for TXS 0506+056. Nevertheless, all the multiple studies on it can be a important starting point for the study of PKS 1424+240.

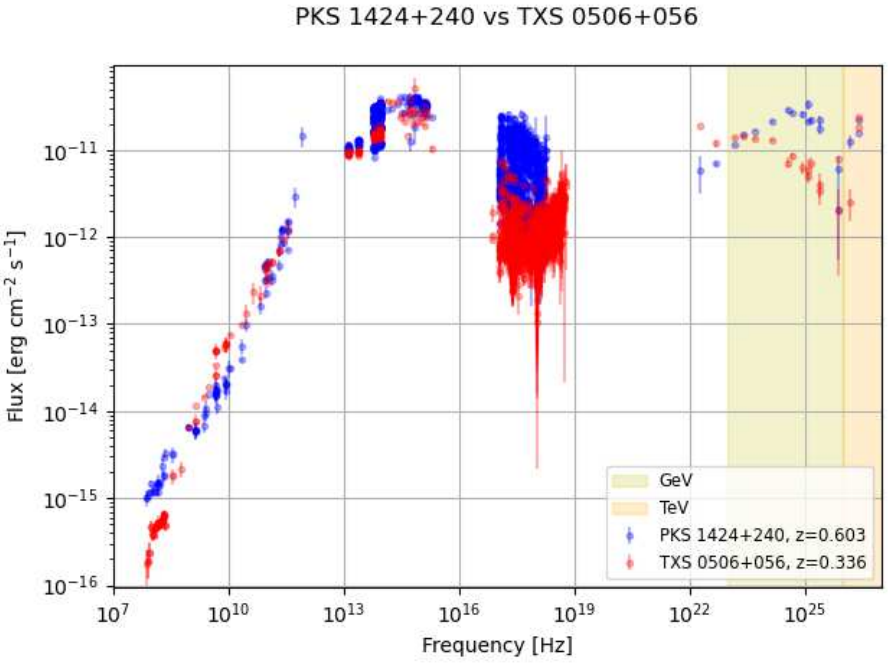

Figure 1.20: SED comparison between PKS 1424+240 (blue dots) and TXS 0506+056 (red dots), the similarity is evident in the low energy part before the synchrotron peak. The distribution is less similar at higher energy, especially at X-ray and at γ-ray energies. A difference between the two sources is the distance, TXS 0506+056 (z=0.336) is much closer with respect to PKS 1424+240 (z=0.603). Data retrieved from Firmamento web page[13].

[13]https://firmamento.hosting.nyu.edu/home

Chapter 2

The MAGIC Telescopes

This chapter is dedicated to the MAGIC telescopes. It provides a detailed explanation of the MAGIC telescopes and their capabilities, covering both hardware and software aspects. It begins with an overview of the technical components of Imaging Atmospheric Cherenkov Telescopes, followed by a description of the standard data analysis procedures, that it will be used to study the blazar PKS 1424+240.

The **Major Atmospheric Gamma-ray Imaging Cherenkov** (MAGIC) telescopes are two Cherenkov telescopes working in stereoscopic mode, located at $\sim$ 2200 m above the sea level in *Observatiorio Roque de los Muchachos* in La Palma, Canary Island, Spain[1], see Fig. 2.1. MAGIC-I, the first telescope, started to operate in 2003, while MAGIC-II was completed in 2009, both telescopes have a primary mirror of 17 m of diameter. Since then, they have been always in operation except for a major upgrade in 2012, (Aleksić et al., 2016a,b). They detect and collect the Cherenkov light produced in the EM shower in the atmosphere, through the technique called *imaging technique*, see the related section, Sec. 1.4.1, in the previous Chapter. The **energy range** spans from 30 GeV up to 100 TeV. At 1 TeV, the **sensitivity** is approximately 0.6% of the Crab Nebula flux for a 50-hour observation, making it one of the most sensitive instruments for detecting very high energy γ-rays, especially at low energies. The telescopes have a **field of view (FoV)** of about 3.5° in diameter.

2.1 MAGIC Hardware

2.1.1 Structure and drive system

The MAGIC telescopes were constructed to observe transient event, in order to do that, the telescopes were built to be both rigid and light-weighted to perform fast repositioning. The telescopes' weights 67 t in total, as the sum of the single component: the camera $\sim$0.89 t, the camera bow and the counterweights $\sim$3.4 t, the towers $\sim$20.2 t, six carriages $\sim$25 t, the Al-mirror and the active mirror control

[1] https://magic.mppmu.mpg.de

∼9 t, and the carbon fiber dish ∼8 t. The MAGIC drive system is the hardware component which moves the telescopes, there are three modes for the driving system, (Aleksić et al., 2016a,b):

- tracking mode: used to track sources during observations;
- repositioning mode: used during standard operation to move from a source and track a new source. In case of fast repositioning mode, the telescopes can repoint every position in less than 30 s;
- parking mode: position where the telescopes are set during the day or bad weather conditions, when no data taking is performed.

The telescopes have a range between -73° and 100° of elevation axis, while the azimuthal axis is 400°, (Aleksić et al., 2012).

Figure 2.1: MAGIC telescopes, Observatiorio Roque de los Muchachos, La Palma, Canary Island, Spain. MAGIC I (left), MAGIC II (right). The project started in 2003 with the construction of MAGIC-I; later in the 2009 a second telescope, MAGIC-II, was added. Since then, the two telescopes worked in stereoscopic mode, making a great improvement in the sensitivity. Credit: Giovanni Ceribella.

2.1.2 Mirrors

The mirrors of MAGIC-I and MAGIC-II are different due to technical reasons, (Doro et al., 2008):

- MAGIC-I is made of aluminum honeycomb sandwich 50×50 cm^2 mirrors produced by INFN Padova and MPI, and mirrors of 1×1 m^2 at the edges with cut

side produced by INFN and cold-slumped mirror produced by INAF. The panels in which mirrors are mounted have a particular design called chess-board structure, due to a wrong defined mirror surface level during the design;

- MAGIC-II is made of 143 1×1 m^2 aluminum honeycomb sandwich mirrors produced by INFN and 140 1×1 m^2 cold-slumped mirrors produced by INAF.

Together, the MAGIC telescopes have a diameter and a focal length of 17 m, and a total reflective surface of 236 m^2. The mirrors are parabolic, this choice was made because even though parabolic mirrors are more expensive than spherical mirrors, they are isochronous so they do not induce time spread in the arrival time of Cherenkov photons. However, since the optics is not perfect, in order to evaluate the optics performance one need the *Point Spread Function* (PSF). The PSF is related to the difference between the ideal geometrical shape of the mirror and the real one; the typical value for MAGIC is less than 10 mm with mirrors focused. The PSF affects the sensitivity at low energies and worsen the pointing resolution. The PSF of both telescopes are measured every night before the observations, (Doro et al., 2008).

2.1.3 Active Mirror Control

The **Active Mirror Control (AMC)** has the function to correct the mirror alignment and focusing, (Biland et al., 2007). When the telescopes move the gravitational load impact is modified. The motion causes deformations that need to be corrected. The AMC consists of several actuators in axial and cardan joints. The scheme of AMC is different in the two telescopes, (Biland et al., 2007):

- MAGIC-I has eight independent chains, horizontally aligned for better maintenance, with eight AMC electronic boxes each;
- MAGIC-II as seven independent chains with eight or nine boxes each.

Every night, before the observations start, the AMC changes the position of the mirrors to correct the focus and estimate the PSF using the SBIG camera, a CCD camera that measures accurately the PSF of individual mirror segments and of the total mirrors, to estimate the reflectivity at different wavelengths.

2.1.4 Camera

The **camera** collects the Cherenkov photons reflected by the mirrors, (Tridon et al., 2009). It is composed of 1039 photomultiplier tubes (PMTs) for each telescope. In total, the field of view is of 3.5° and the PMTs are grouped in 169 cluster of 7 pixels. Each PMT has a light collector (Wiston cone) that is an optical device used to efficiently focus light onto the PMT. The Vertical Cavity Surface Emitting Lasers (VCSELs) convert the signal into an optical signal, it can produce a near IR light (850 nm).
Different components have then different propose for the operation of the camera, (Tridon et al., 2009):

- the *temperature cool* system is composed of two plates of aluminum with horizontal water channels, they are at 20°C;
- the *drying unit* removes damp air from the camera, dehumidifies it and returns it to the camera, however, it is located only in MAGIC-II;
- the *lids* protect the camera, they are closed when the telescopes do not observe;
- the *spectralon plate* is set 3 cm above the plexiglass window, the star images are focused on it, allowing the gamma images to be focus at the PMT plane;
- the *Starguider LEDs* are used by the Starguider camera, a CCD camera to monitor the tracking system online that has been installed in the center of the mirror dish, to find the position of the camera relative imaging;
- the *low voltage power supplies* are located underneath the camera, each camera has two of them;
- the *temperature and humidity sensor*, respectively, eight and four sensors, slow control of the camera's conditions;
- the *Moon filter* is used in presence of bright moon.

2.1.5 Trigger System

MAGIC has a standard trigger that consist of three levels, called L1, L2 and L3. The first trigger level, L0, digitalizes the signals from the inner pixels of the camera, in the so-called trigger region, via a discriminator threshold. The width and delay of the digitized signal should be adjusted to strike a balance between the L1 trigger rate, which depends on the width of the L0 signals, and achieving a good distribution of arrival times at the L1 board. The time spread is mostly due to electronics. The widths and delays adjustment is performed thanks to the program called HYDRA (HYperfast Delay and Rate Adjustment), developed by MAGIC collaboration members: this results in a reasonable gate for the L1 trigger, reducing the rate of accidental triggers, (Berti, 2018).
After the L0 trigger, the digitized signals are transmitted to L1, which distributes them to the right boards. The signals are sent to the Trigger Processing Unit (TPU), which creates the final trigger, performing a global logical OR of the signals. In the case of a trigger, the L1 trigger signals (one per telescope) are sent to the L3 board and prescaler board. The L3 or stereoscopic trigger is hosted in a specific PULSAR board (L3T) with two mezzanines, one for the standard trigger (L1) and the other for the Sum-Trigger signals. The L3 trigger executes a logical OR between the two L1 trigger signals: if a trigger is generated, the L3 trigger signal is sent to the readout of the two telescopes. A L3 trigger number is generated as well by the mezzanines and is used later in the offline analysis, (Berti, 2018).
Additionally to the standard trigger level, other two trigger system can be selected: the Sum-Trigger and the Topological Trigger. The Sum-Trigger is an analog trigger without any topological logic, two electronics of the Sum-Trigger are present, one for

each telescope. They are used to perform the L3 trigger. The Topological Trigger (Topo-Trigger) uses the spatial information at the trigger level. The basic idea is that γ-ray initiated showers will trigger the same macrocells in both cameras, or if a specific macrocell is triggered in the first telescope, the surrounding macrocells will be triggered in the second telescope, (Berti, 2018).

2.1.6 Weather instrumentation

The instruments used by MAGIC to monitor the weather conditions are:

- **LIDAR**; it is used to measure the atmospheric transmission through the aerosol. It is located in a tower close to the MAGIC counting house, and it is protected by a dome. It sends electromagnetic pulses via a laser, that are back-scattered by clouds or aerosol; then it records the arrival time distribution of the photons and measure the transparency of the atmosphere assuming an extinction method, (Fruck et al., 2014). This system measures the transparency of the atmosphere, and it quantifies the information via a parameter called *transmission coefficient*. The structure of LIDAR is shown inf Fig. 2.2.
- **Weather station**; it measures parameters such as the temperature, the humidity, the wind speed and direction.
- **Pyrometer**; it evaluates the presence of clouds in the atmosphere and measures the sky temperature. Its output parameter is called *cloudiness*.
- **Dust Particle Counter**; this instrument is at the Telescopio Nazionale Galileo, however, its result are used also by MAGIC. It measures the dust density through a laser scattering.
- **allSkyCamera**; a camera that takes images of the sky, these images are needed to investigate the sky conditions.

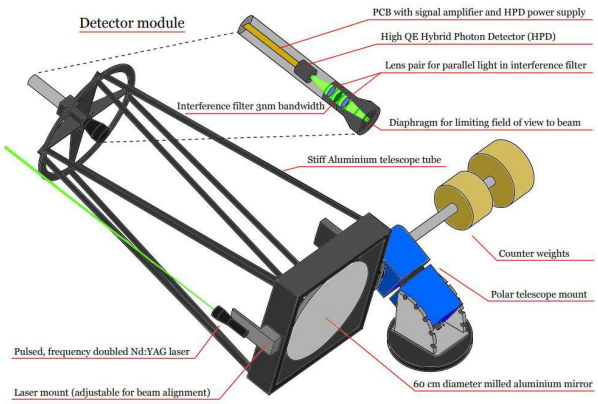

Figure 2.2: Schematic representation of LIDAR structure.The LIDAR system is employed to assess atmospheric transmission through aerosols. It emits electromagnetic pulses via a laser, which are then back scattered by clouds or aerosols. The system records the distribution of photon arrival times and measures the atmosphere's transparency using an extinction method. From Fruck et al. (2014).

2.2 MAGIC software

2.2.1 Central Control

As was already discussed, the MAGIC has several subsystems, some of them are telescope-related that control different hardware component. For example, the drive system, AMC, Camera Control (CaCo) and LIDAR, a weather related instrument. All these subsystems are controlled by the **MAGIC Central Control (CC)** via TCP/IP. The CC program called **SuperArehucas (SA)** has a Graphical User Interface (GUI) to operate telescopes. It interfaces subsystems that do not communicate within each other. SA coordinates action of each subsystem, automatizes some data taking and avoids oversights of instruments. The connection between CC and other subsystem is via TPC/IP sockets, each subsystem opens a *read socket* to obtain information from the CC and a *write socket* to send back information to the CC. The subsystem send a report to the CC every second, while the SA sends the report to the subsystem every ten seconds. The CaCo and the LIDAR subsystem communicate both with the weather station and SA. This is necessary in order to have automatic reaction in case the operation safety limits are not fulfilled during observations, (Bretz et al., 2009).

2.2.2 Automatic Alert System

The **MAGIC automatic alert system** processes the alerts coming from the Gamma-ray Coordinates Network (GCN)[2] and communicates with the MAGIC CC. This is needed to observe transient events (e.g., gamma-ray burst). The automatic alert

[2]The GCN is an open-source platform created by NASA to receive and transmit alerts about astronomical transient phenomena.

system is a multithread C program running in background full-time. The system handles the alert sent from the GCN and if the target is observable it sends an alert string to the CC, which automatically repoints the telescopes.

2.2.3 Data and Analysis at the MAGIC site

MOLA

MOLA (Magic OnLine Analysis) is a program that perform an analysis from low level up to high level, obtaining preliminary result on flux and significance of observed sources. It runs every night during observations. The result is very useful for Target of Opportunities (ToOs), which follow up transient events and flaring sources, (Tescaro et al., 2013)

OSA

The On-Site Analysis (OSA) program performs low level analysis. The raw data from the DAQ and the reports from the CC are copied in a common storage (GFS2) and inserted in a MySQL database. The OSA proceeds with the analysis and sends the results to Port d'Informacio Cientifica (PIC) in Barcelona, where the data are stored. The data are ready to be analyzed at upper level. This system reduces the data size of a factor ∼500, making the transfer faster.

Data and Daily Check

The **Data Check System** is a series of script that run automatically at the end of the observation time. The result is a graphical output that allow to verify the condition that might affect data taking quality. The main plot produced is called **Superplot**, see Fig. 2.3, that contains:

- zenith angle distribution (Zd) as a function of time for each source;
- the current of the M2 (DC) as a function of time;
- L3 trigger rate as function of time;
- the Transmission coefficient at 9 km (T_{9km}), at 3 km (T_{3km}) and the cloudiness as a function of time.

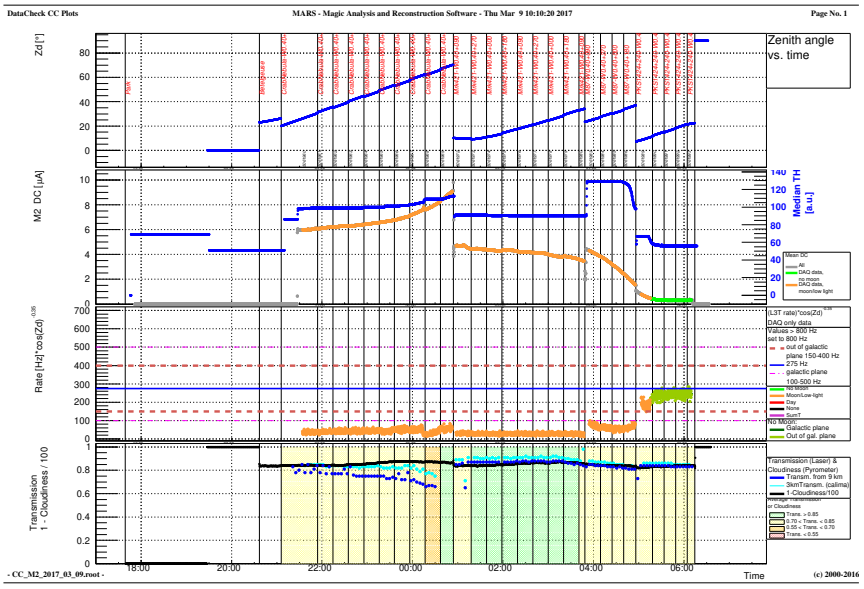

Figure 2.3: An example of a superplot graphical output. From the top to the bottom: Zd vs. time, the blue line representing the track of the observed source; M2 DC vs. time, the green track represents observation without moon, while the orange track with moon; L3 trigger vs. time; T_{9km} and cloudiness vs. time, it shows the quality of the transmission laser with a color scale from green (optimal) to red (bad). Superplot of 9^{th} March 2017, this day was close to the full moon. From Datacheck and Onsite Analysis Plots[3].

2.3 MAGIC data taking

2.3.1 Night conditions

IACTs, therefore also MAGIC, are instruments with a low duty cycle; the best performances are obtained in during the so-called *dark time*, i.e., moonless night, that is the standard operation condition. Each year the dark time accounts for ∼1600 hours that translate into a duty cycle of ∼18%. However, the real value is lower since bad weather and technical problem can happen during the night. Taking into account this issue, the overall efficiency of dark time observed each year is roughly 60%. To overcome this problem and increase the observational time, MAGIC can observe also with the presence of the moon, *moon time*. MAGIC can observe up to 75% of moon time, stopping only a few days during full moon. Since the NSB in moon time is higher, different discriminator threshold should be set and a dedicated analysis of the data should be performed, (Aleksić et al., 2016a).
However, the observation is not possible if some *safety limits* are not satisfied. To

[3]http://www.magic.iac.es/operations/datacheck/ccsuper/ (internal page)

avoid possible risk of damaging the hardware components, the following criteria must be respected:

- humidity <90%;
- average PMT current <30μA;
- individual PMT <47 μA;
- wind speed <50 km/h;
- minimum zenith distance 1.5°.

2.3.2 Pointing configurations

MAGIC can take data in two different pointing configurations, the ON mode and the WOBBLE mode, see Fig. 2.4

ON mode: this setting requires two types of observation in order to be performed, an ON observation in which the pointed source lies at the center of the camera and an OFF observation in which no source is pointed at the center (preferably having similar zenith and azimuth). The OFF observation is needed to have an estimation of the background.

WOBBLE mode: this setting is a false source tracking method, (Fomin et al., 1994), in which offsets from the source are tracked; the standard offset for point-like sources is 0.4°. One or more OFF position are selected to evaluate the background sky in the opposite direction of the camera. To have an unbiased estimation of the background, more than one wobble position are needed, usually four. Currently, the wobble tracking is the default pointing mode in MAGIC.

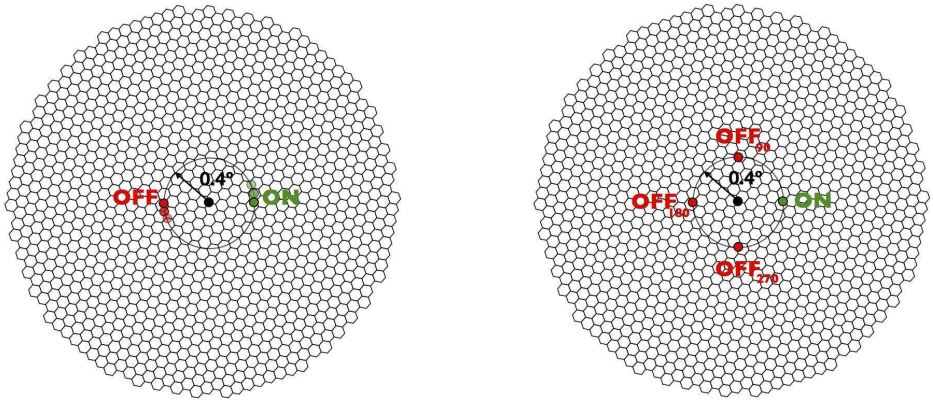

Figure 2.4: The WOBBLE pointing mode. Left: 1 OFF, right: 3 OFF. The black dot represents the center of the camera. This setting is a false source tracking method in which offsets from the source are tracked. One or more OFF positions are chosen to assess the background sky in the direction opposite to the camera. To obtain an unbiased estimate of the background, multiple wobble positions are required. From López-Coto (2017).

2.4 Data analysis

MAGIC data analysis software is called **MAGIC Analysis and Reconstruction Software (MARS)**, (Moralejo et al., 2009). It consists of a collection of programs written in C++ and using *ROOT* libraries[4]. The whole data analysis can be subdivided into three stage of data processing, (Moralejo et al., 2009):

1. at **low level**, data are converted from binary raw into ROOT format and calibrated. Image cleaning and image parametrization are done. It is the longer part since it deals with a huge amount of data and requires many CPU-hours. It is usually done on site by OSA, except for moon data. Used programs: `merpp`, `sorcerer`, `star`;

2. at **intermediate level**, data of individual telescopes are merged in order to have a *stereo image* parameters, Random Forest (RF) and Look-Up Tables (LUTs) algorithms are trained and applied to data. Most of the time this is the starting point for data analysis. Used programs: `superstar`, `coach`, `melibea`;

3. at **high level**, graphical output for final result are obtained. Used programs: `odie`, `capsar`, `flute`, `fold`, `CombUnfold`.

2.4.1 Monte Carlo γ-ray analysis

Monte Carlo (MC) simulations of γ-ray are needed in the analysis process γ-ray data, since no other source ofγ-ray can be used, (Majumdar et al., 2005). The

[4]https://root.cern.ch/

program used to perform MC simulation is `CORSIKA` (COsmic Ray Simulation for KAscade), (Heck et al., 1998). It simulates the atmospheric cascades initiated bye primary particle, the transport of particle in the atmosphere, their interaction with atmospheric nuclei and their decay. MAGIC uses a customized version of `CORSIKA` called *mmcs*, that calculates and stores several parameters, such as particle's type, energy, direction, arrival time and location of the shower. Then `reflector` is the program which simulates the atmospheric absorption of the Cherenkov photons and the mirror response of the telescope to the incoming Cherenkov light. Lastly, the program `camera` simulates the camera response and of the electronic chain.
The output MC data file can be analyzed together with observational data since they have the same format.

2.4.2 Low level analysis

The first step of the low level analysis is the conversion from raw file (output of the DAQ) into ROOT file. The conversion is done by `merpp` (MERging and Processing Program) which also merges the data file and the subsystem reports. Then, the program `sorcerer` (Simple, Outright Raw Calibration, Easy, Reliable Extraction Routines) performs the *calibration* and *signal extraction* on the waveforms of the signal. The main purpose is to obtain two pieces of information for each pixel in each event: *charge* (converted from ADC[5] counts to number of photoelectrons) and *arrival time* of the signal.

The first step for *signal extraction* is to estimate a baseline. Initially, the signal of each pixel is initially stored in time slices and the signal waveform is composed by the sum of the actual signal and the baseline of the capacitors. In order to estimate the baseline, the recorded time slices stored are binned into a histogram and then fitted with a Gaussian. The mean value of the fit is taken as baseline and then removed from the signal. After the subtraction, the *sliding window* algorithm extracts the signal. After the extraction of the signal, the *calibration* can be performed. The signal is given in integrated readout counts, and it needs to be converted in photoelectrons. The method used is called *F-factor method*, it assumes that one readout count corresponds to C photoelectron, (Mirzoyan, 1997). The number of photoelectrons follows a Poisson distribution. The conversion factor reads as:

$$C = \frac{N_{\text{phe}}}{\mu} = \frac{\mu}{\sigma^2_{\text{signal}} - \sigma^2_{\text{noise}}} F^2, \tag{2.1}$$

where F^2 is the excess noise factor, σ^2_{signal} and σ^2_{noise} are the standard deviation of signal and noise, N_{phe} is the number of photoelectron, and μ is the readout counts. Since PMTs have different gain, a *flatfielding* procedure is done, and the conversion factor can be written as:

$$C = \frac{N_{\text{phe, average}}}{\mu}, \tag{2.2}$$

[5] Analogue to Digital Converter

where $N_{\text{phe, average}}$ is the number of photoelectron averaged over all pixels.
Finally, the *arrival time* of the signal is extracted by performing an average time slices of the integrated window weighted with the signal:

$$t_{arrival} = \frac{\sum_i i \times s_i}{\sum_i s_i}, \tag{2.3}$$

where i is the time slice number and s_i is the signal in slice.
The next step, once the calibration is done, is an **image cleaning** procedure and an **image parametrization**. The cleaning is needed to remove pixels which do not belong to a given shower image, see Fig. 2.5 for an example of showers detected by MAGIC. The program used for both cleaning and parametrization is `star` (STandard Analysis and image Reconstruction). This algorithm has the purpose to reject pixels that contain fluctuations of NSB or electronic noise and to ensure that most of the image is conserved to avoid signal losses. The image cleaning algorithm can be summarized in two steps, (Aliu et al., 2009):

- **sum image cleaning**; the signals are clipped in amplitude to reduce the NSB. Different combinations of neighboring pixels are summed and if the signal is higher than a threshold value and if it is arrived in a specific time interval, then the signal is part of the shower image, (Aliu et al., 2009)
- **time-constrained absolute image cleaning**; surviving pixels are classified into two categories, *core* and *boundary* pixels. Core pixels are the one having as direct neighbor at least one pixel survived from the sum filter and its charge is above a threshold, Q_{core}. Then, if the arrival time of the core pixel is within a 4.5 ns window from the mean arrival time, the pixel is kept. The boundary pixels are the pixel having as neighbor core pixels with a charge larger than another threshold, $Q_{boundary}$. Then, their arrival time should be less than 1.5 ns with respect to the core pixels, (Aliu et al., 2009).

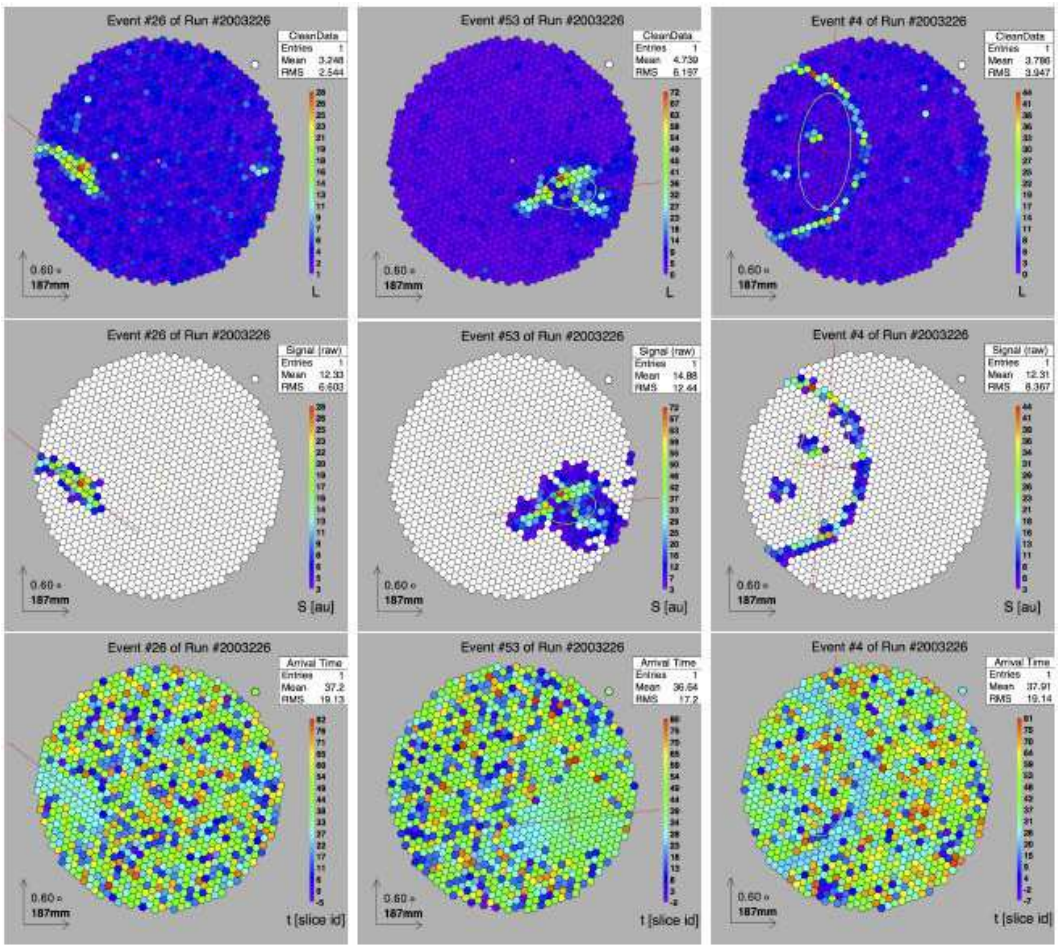

Figure 2.5: Example of showers detected by MAGIC. Top panel: charge distribution before image cleaning. Middle panel: charge distribution after image cleaning. Bottom panel: arrival time distribution. The showers are induced by photons (left) which display an elliptical shape, by hadrons (center) which display a non-homogeneous shape, and by muons (right) which display the typical muon-ring. From Garrido-Terrats (2015).

In standard condition, the core and boundary threshold (Q_{core} and $Q_{boundary}$) are set to 6 phes and 3.5 phes, respectively. This is valid for dark time, in presence of the moon, the NSB effect is higher and this implies higher values for the threshold. Then the image parametrization is the last step of low level analysis. The stored and cleaned images are used to extract a set of parameters. The image parameters are fundamental for the data analysis chain since they allow a discrimination of γ/hadron event and an estimation of the incoming direction and energy in the following steps. The main parameters, see Fig. 2.6, are:

- **Hillas parameters** (e.g., size, width, Center of Gravity); it is a set of basic parameter introduced by Hillas (1985). They are defined by how the photons are distributed in pixels that constitute the Cherenkov image. The parame-

ter *size* is, in first approximation, proportional to the energy of the primary particle.

- **Source-dependent parameters** (e.g., alpha, dist); they are related to physical properties of the shower depending on the expected position of the source.
- **Time parameters** (e.g., Time gradient, time RMS); they take into account the arrival time of the Cherenkov signal.
- **Image quality parameters** (e.g., leakageN, number of islands); they are needed to evaluate the noise level of the image.
- **Directional parameters** (e.g., asymmetry, M3Long); they are used to discriminating between the head and the tail of the shower.

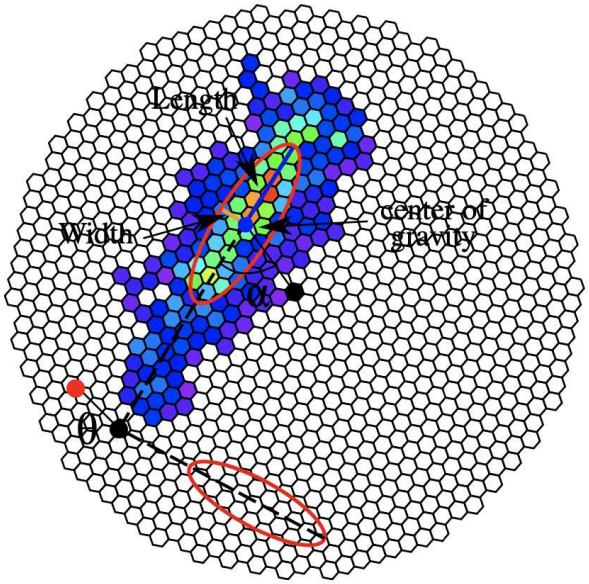

Figure 2.6: Image of a shower induced by photons in the camera showing the typical elliptical shape, and some Hillas parameters of a cleaned image. The black dot is the reconstructed position of the source, while the red dot is the true position of the source. From wiki MAGIC[6].

2.4.3 Intermediate level analysis

In the low level stage, the analysis is performed separately for each telescope. The intermediate level starts with the **stereoscopic reconstruction** in order to merge the information into a single file, see Fig. 2.7. The program performing this task is `superstar`. It is responsible for a purely geometric reconstruction of the three-dimensional shower. Another set of parameter, *stereo parameters*, are calculated to

[6]https://wiki.magic.pic.es/index.php/Main_Page (internal page)

obtain a better energy and direction reconstruction. However, the main point of `superstar` is to merge as input the two `star` files of the same events with individual image parameters to a stereo file.
For standard analysis, the low level stage is done by OSA. Therefore, the work done by an analyzer start from the `superstar` files. The first step is usually to run the program `quate` to check the quality of the dataset. It divides the data runs that may present *non-standard* conditions from the *good* conditions. It can be applied to `star`, `superstar` or `melibea` files and the cuts can be modified depending on the needed result. Usual cuts include:

- to select upper and lower cuts value for Zd, Az, atmospheric transmission, Direct Current (DC) and check if there are runs out of range to exclude them;
- to find dataset affected by technical problems, e.g., faulty subsystem, wrongly observational configuration, data taken during hardware change or data test;
- to find data with bad atmospheric condition, checked by the transmission value at 9 km, or data taken during moon-light, controlled by the DC value.

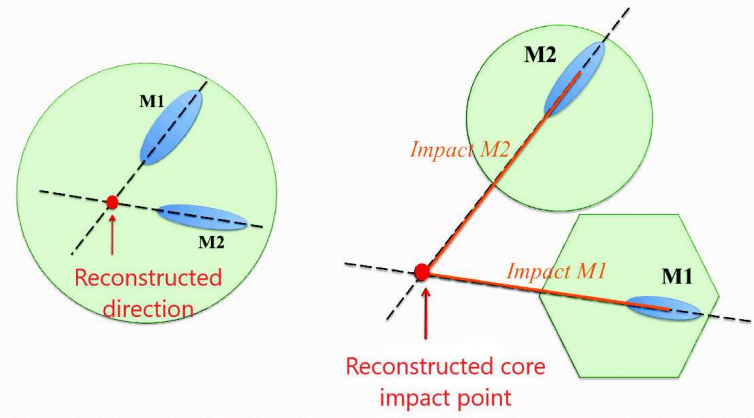

Figure 2.7: Geometrical reconstruction of the direction and impact point. The low level result from each telescope is merged to reconstruct a stereoscopic analysis. The addition of the second MAGIC telescope made the reconstruction of the incident direction less complicated. M1 and M2 stand for MAGIC I and MAGIC II, respectively. From wiki MAGIC[7].

A key point of the analysis is to identify the nature of the events and to separate γ-ray showers from the background. MAGIC is an IACT, and therefore it is a background-dominated instrument, the majority of the events that trigger the telescopes are hadronic-induced showers. Indeed, other source of background are *accidental triggers* due to NBS light, moon light or electronic shot noise, muons and electron-positron induced showers. In addition to the separation of events, for the

[7]https://wiki.magic.pic.es/index.php/Main_Page (internal page)

high stage analysis it is needed a reconstruction of the arrival direction and the energy of the events.
For all this tasks, γ-hadron separation, direction reconstruction and energy estimation, is used a *Random Forest (RF)* classification algorithm, (Albert et al., 2008). However, the energy estimation can also be performed with the *Look-Up Tables (LUTs)* algorithm. The program used to create RF or LUTs is called `coach` (Compressed Osteria Alias Computation of the Hadronness parameter).
The γ-hadron separation is the most important point. Even in the brightest γ-ray sources, the number of hadrons is $\sim$3 orders of magnitude larger than the γ-ray. Therefore, a powerful discrimination method is necessary. In MARS, it is used a RF, a multidimensional algorithm based on decision trees. RF trees are generated using sample parameters calculated in `star` and `superstar`. The default number of trees is 100, but it can be modified. The construction of trees starts with the selection of a random parameter, and a *cut value* is searched by the RF algorithm in order to get the best division between γ-ray and hadron events. Now the events are separated, based on their value, in two subsamples called *branches*. The cut value is obtained by minimizing the Gini index, (Catalano et al., 2009):

$$Q_{gini} = \frac{4N_h N_\gamma}{(N_h + N_\gamma)^2}, \tag{2.4}$$

where N_γ and N_h are respectively the number of γ-ray events and the number of hadron events. The Gini index gives an estimate of the variance of the distribution of γ-ray and hadronic events. The procedure is then repeated, the best parameter is chosen for each subsample, and new branches are created. The process stops either if in a subsample there are only γ or hadron, or if the subsample has a too low number of events. The last resulting subsamples are called *leaf* and a value 0 (γ-like events) or 1 (hadronic-like events) is assigned to them, this parameter is called **hadroness**, and it contains information of the particles' nature.

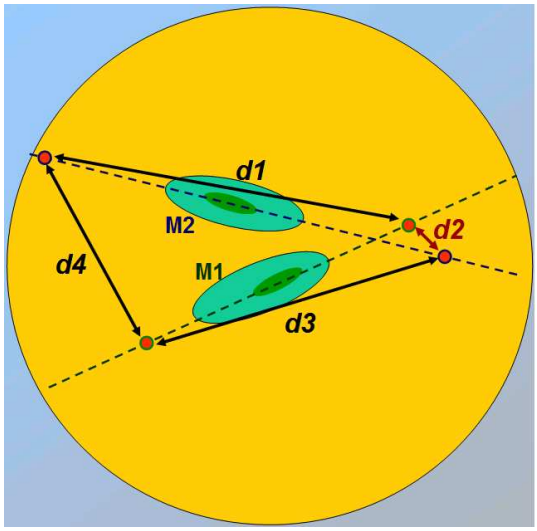

Figure 2.8: DISP parameters. The DISP RF method reconstructs the DISP parameter using a RF algorithm. M1 and M2 stand for MAGIC I and MAGIC II, respectively. From wiki MAGIC[8].

The program `coach` need two input cards of so-called *training samples* to *train* the RF, a *MC train sample* containing a sample of MC simulated γ-rays, and an *OFF data sample* containing data with no evidence of γ-ray signal ($<$1% C.U.). At this point, the MC simulation are divided into two categories: *train* and *test*. The MC train is needed and used by `coach`, while the MC test by `melibea`. It is essential that both sample, OFF and MC, are chosen from the same analysis period and in the same zenital range of the *ON data*, the data related to the source that need to be analyzed. Moreover, the OFF data need to match as much is possible the observational conditions of the ON data, e.g., dark/moon night, extragalactic/galactic source.
Then, the RF is applied in the program *melibea* that has as input both ON data and MC test sample. At the end of RF creation, a value of 0 or 1 it is assigned to each leaf, the final hadroness value h of the events is the average of the all h_i value over N trained trees:

$$h = \frac{1}{N}\sum_{i=1}^{N} h_i. \tag{2.5}$$

Beside hadroness, a second quantity obtained in this step is the reconstruction of **incident direction** of the primary γ-ray. The method is called **DISP RF method**, (Aleksić et al., 2016b; Fomin et al., 1994). It reconstructs the DISP parameter using a RF algorithm applied to a continued variable. The γ-ray showers display elliptical images at the camera. The DISP parameter represent the distance between the image Center of Gravity (CoG) and the source position, see Fig. 2.8;

$$\mathrm{DISP} = A(\mathrm{size}) + B(\mathrm{size})\frac{\mathrm{widht}}{\mathrm{length} + \eta(\mathrm{size})\mathrm{leakage2}}, \tag{2.6}$$

[8] https://wiki.magic.pic.es/index.php/Main_Page (internal page)

where a(size), B(size) and η(size) are second order polynomials of log(size); they are optimized using MCs and performing a regression on a continuous quantity using a RF. The DISP is computed for each telescope and for each event, therefore there are two DISP value for each event. As a result, four potential source position are estimated. Furthermore, a *crossing method* is used to remove the degeneracy.

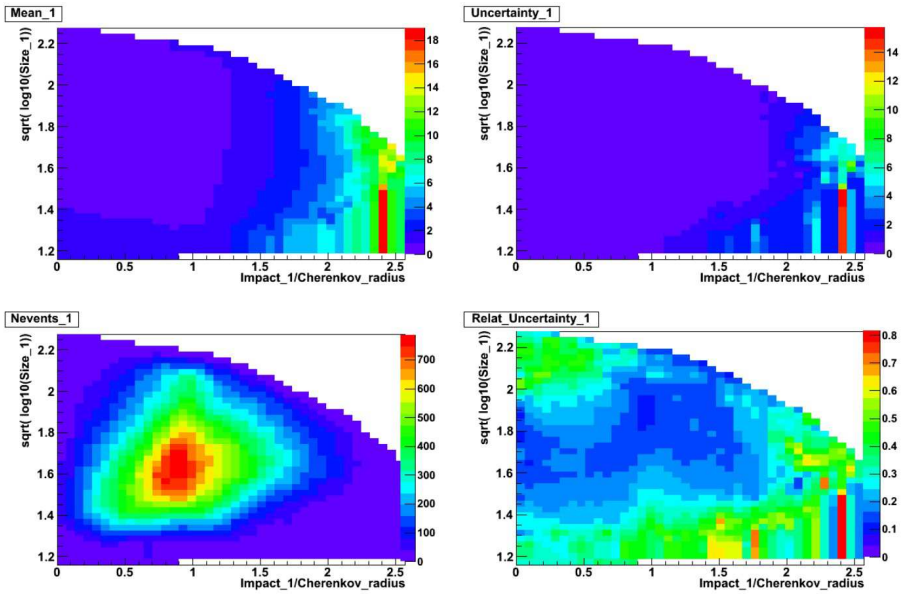

Figure 2.9: Energy reconstruction. The energy of the incident photon is almost proportional to the amount of Cherenkov photons produced, and consequently to the image size measured by the telescopes. The γ MC training sample is divided in bins for every parameter considered for the energy reconstruction. A multidimensional table containing the mean energy of MC events belonging to each bin is built. Then the estimated energy of a real event is the value stored in the table for the multiparameter bin corresponding to this event. From wiki MAGIC[9].

The third and last quantity is the **energy estimation** of the events. It can be done by using RFs or LUTs, the current standard procedure uses LUTs. They are build by `coach` through the MC training samples. LUTs are based on the assumption that the energy of the primary γ-ray is proportional to the amount of Cherenkov photons produced by the shower, and as a consequence, on the size parameter, (Aleksić et al., 2012). The MCs are divided into bins of size and impact parameter/ r_C, where r_C is the Cherenkov radius. Then, a two-dimensional table is created, it contains the mean energy and the root-mean-square (rms) of MC events for each bin. At the end, a value of the estimated energy (E_{est}) of a real event is stored in the LUTs for both telescopes. The value of the mean estimated energy is then computed and properly weighted with the rms of the individual energies. However, a RF can be used to obtain the same result, but it is not the standard choice, RF are used especially for higher energies.

[9]https://wiki.magic.pic.es/index.php/Main_Page (internal page)

2.4.4 High level analysis

Once hadroness, reconstructed direction and energy are done, it is possible to start the high level analysis. At this stage, signal's *significance*, *skymaps*, *spectrum* and *light curves* are obtained.
The program `odie` is responsible for the extraction of the signal's significance, it creates the θ^2 **distribution plots**, see Fig. 2.10; where θ^2 is the angular distance between the reconstructed position of the source and the real position. The θ^2 parameter evaluates the presence of significant γ-ray signal from a given region in the sky; γ-ray events would accumulate at smaller values of hadroness and θ^2, while hadronic events would be isotropically distributed for θ^2 with higher value of hadroness.
To optimize the significance, the cuts on hadroness and θ^2 need to be changed depending on the energy range, see Table 2.1. The three energy cuts are:

- **Low Energy (LE)** cuts provide the best sensitivity at energy below 100 GeV, a low value of size is required to count low energy events. They are used for sources with a VHE *soft*-spectrum.
- **Full Range Energy (FR)** cuts provide the best sensitivity for intermediate energy range. It gives the best performance on sources with Crab-like spectrum (-2.6 spectral index).
- **High Energy (HE)** cuts provide the best sensitivity at energies above 1 TeV, it is also added another cut on the estimated energy E_{est}.

These three cuts are used to maximize the significance in different energy ranges, they are activated or not dependently on the source.

Energy Range deg^2	θ^2	Hadroness	Size M1 phe	Size M2 phe	E_{est} GeV
Low Energies	$<$0.02	$<$0.28	$>$60	$>$60	-
Full Range Energies	$<$0.009	$<$0.16	$>$300	$>$300	-
High Energies	$<$0.007	$<$0.1	$>$400	$>$400	$>$1000

Table 2.1: Standard cuts optimized for different energy ranges. From wiki MAGIC[10].

The cut value of θ^2, θ^2_{cut}, is the upper bound of the *signal region*. Two histograms, *signal histogram* and *background histogram*, are build, where the events are binned on the basis of their θ^2 value. The signal histogram is related to the ON region and the number of events, N_{ON} are calculated. While the background histogram is related to the OFF region, where there are the events from the OFF. The binned OFF events are calculated as the angular distance between the arrival direction of the event and the OFF region position. The histogram gives an estimate on the number of background events, N_{OFF}. The overplot of the signal and background histogram is the θ^2 plot. The number of excess events, N_{ex} is calculated as follows:

$$N_{ex} = N_{ON} - \alpha N_{OFF}, \tag{2.7}$$

[10]https://wiki.magic.pic.es/index.php/Main_Page (internal page)

where α is the ration between the number of OFF and ON regions.
The **significance** of the signal is estimated by using the Li&Ma equation, (Li and Ma, 1983):

$$\sigma_{\text{Li\&Ma}} = \sqrt{2\Big[N_{ON} \ln\Big(\frac{1+\alpha}{\alpha} \cdot \frac{N_{ON}}{N_{ON}+N_{OFF}}\Big) + N_{OFF} \ln\Big((1+\alpha)\frac{N_{OFF}}{N_{ON}+N_{OFF}}\Big)\Big]} \tag{2.8}$$

For a Gaussian distribution a $\sigma_{\text{Li\&Ma}} > 5\sigma$ is not consistent with the background; therefore a γ-ray detection can be claimed.

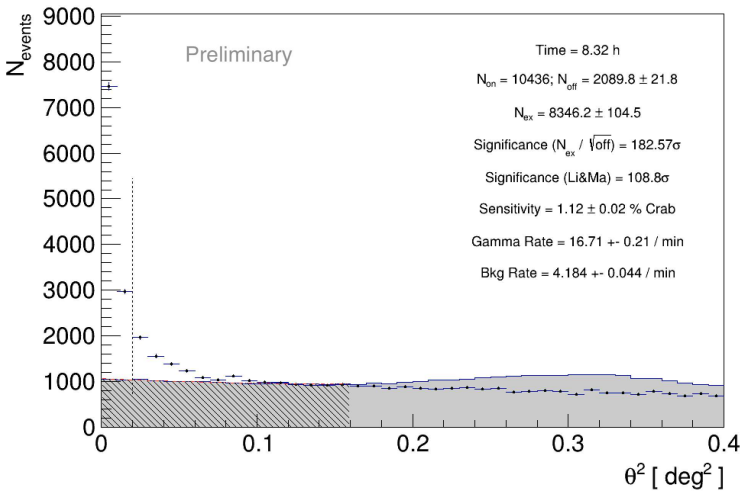

Figure 2.10: Example of low energy θ^2 plot of Crab Nebula. The gray histogram is the background histogram. The points correspond to values of the signal histogram. The vertical dashed line is the θ^2_{cut}. The presence of a *bump* at 0.3 deg^2 is due to the fact that Crab Nebula is a extended source. Analysis done for the Crab check, see Sec 3.2 for more details.

The signal significance and the sensitivity are parameters used to quantify the performance of an instrument. The IACTs sensitivity is usually defined as the minimum flux needed tot detect the Crab Nebula with a significance of 5σ after 50 hours of observation. The *integral sensitivity* of MAGIC is calculated for sources that have a Crab-like spectrum, in it is 0.55% Crab Units (C.U.) at few hundreds of GeV. The *differential sensitivity* is, instead, valid for sources with any other spectral shape; the cuts' optimization is performed in narrow bins of energy, it is 6.7% in the lowest energy band, 60-100 GeV.
To produce **skymaps**, a two-dimensional histogram that contain the γ-ray candidate events, see Fig. 2.11, it is used the program `caspar`. At first, skymaps are produced through a camera exposure model to take into account non homogeneity; from this model, an OFF background map is generated. To create the ON map, data coming from the events are used. The PSF of the instrument is used to smoothing these histograms, it is added in quadrature with a Gaussian kernel to smear the number of excesses. Normally, the Gaussian kernel is taken to be equal to the PSF, and

therefore:

$$\sigma_{\text{smooth}} = \sqrt{2}\sigma_{PSF} \tag{2.9}$$

Then, through the Test Statistic (TS) method the significance of a signal in skymaps is calculated; it corresponds the Li&Ma significance applied on a background that is modelled and smoothed.

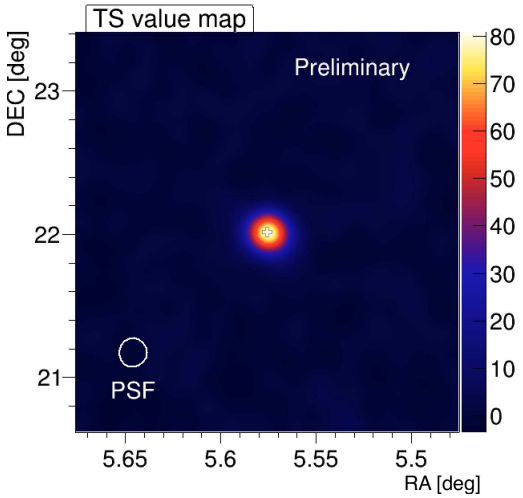

Figure 2.11: Example of low energy skymap of Crab Nebula. It is a two-dimensional histogram that contain the γ-ray candidate events. The PSF of the instrument is used to smoothing these histograms. Analysis done for the Crab check, see Sec 3.2 for more details.

Then, to obtain **spectrum** and **light curve**, it is used the program `flute`. The *differential spectrum* of a source is defined by the number of photons emitted per unit of energy, area, and time:

$$\frac{d\phi}{dE} = \frac{dN_\gamma(E)}{dE dA_{\text{eff}}(E) dt}, \tag{2.10}$$

To evaluate all these features are needed: the total number of γ-rays N_γ, the effective collection area of the instrument A_{eff}, and the effective observation time t_{eff}. These quantities are computed by `flute`, the `MARS` program which calculates the above-mentioned SED and LC.
Instead, the *integral flux* is defined in a specific energy range $[E_{thr}; E_{max}]$:

$$\phi_{E_{thr}<E<E_{max}} = \int_{E_{thr}}^{E_{max}} \frac{d\phi}{dE} dE \qquad \text{cm}^{-2}\ \text{s}^{-1}. \tag{2.11}$$

The LC is the time evolution of the integral flux in a specific energy and time range. While the *Spectral Energy Distribution (SED)* is defined as:

$$E^2 \frac{d\phi}{dE} = E \frac{d\phi}{d(\log E)} \qquad \text{TeV cm}^{-2}\ \text{s}^{-1}, \tag{2.12}$$

the units are the one used by MAGIC.
The total number of γ-rays N_γ is the number of excess event N_{ex}, it is calculated similarly as it was done by `odie`. The main difference is that in `flute` the cuts (size, hadroness and θ^2) are optimized for each energy range.
The effective collection area of the instrument A_{eff} is the area of an ideal detector which detects the same as MAGIC. It can be approximated to the size of the Cherenkov light pool. It has dependency on the energy of the γ-rays and on the zenith angle.

$$A_{\text{eff}}(E; E + dE) = A_{sim} \frac{N_{sel}(E; E + dE)}{N_{sim}(E; E + dE)}, \tag{2.13}$$

where A_{sim} is the simulated geometrical area of MC data, N_{sel} is the number of survived events, N_{sim} is the number of simulated events. Then, the effective collection area, considering an observed source having $d\phi/dE$ spectrum, is weighted on the spectrum as:

$$\langle A_{\text{eff}} \rangle_{[E_1,E_2]} = \frac{\int_{E_1}^{E_2} \frac{d\phi}{dE} A_{\text{eff}}(E) dE}{\int_{E_1}^{E_2} \frac{d\phi}{dE} dE}. \tag{2.14}$$

The average A_{eff} is done with energy-dependent weights on $A_{\text{eff}}(E)$ in narrow bins. The collection area is calculated in bins of zenith angle, similar to the energy bins, its average reads:

$$\langle A_{\text{eff}} \rangle_{[Zd_1,Zd_2]} = \int_{Zd_1}^{Zd_2} A_{\text{eff}}[Zd] f(Zd) d(Zd), \tag{2.15}$$

where $f(Zd)$ is the fraction of the observation time spent at the zenith angle Zd. The collection area has a secondary dependency on the *azimuth angle*.
The effective observation time t_{eff}, is evaluated by subtracting the *dead time* d of the DAQ from the total observation time. If it is assumed that the events' arrival time follows a Poissonian statistic, then:

$$t_{\text{eff}} = \frac{t_{elapsed}}{1 + \lambda d}, \tag{2.16}$$

where $t_{elapsed}$ is the elapsed time, the interval of time between the beginning and the end of the observation.
When N_γ, A_{eff}, and t_{eff} are evaluated, the differential energy spectrum is computed in bins of *estimated energy*, there is no information on the true energy of the events. Nevertheless, the effective area is calculated in bins of true energy of the MC γ-rays; this can lead to the *spillover/migration* of the events, and the flux is wrongly reconstructed. To solve this problem, it is needed an **unfolding method**. A *simple unfolding* is present in `flute`, it is a basic approach based on the number of events that survive the cuts for the collection area. This works in first approximation, however the spectrum is non corrected for additional problem:

- the energy resolution is limited;
- the detector's acceptance is limited;

- other effects, e.g., detection efficiency of the non-ideal detector, binning of variables, systematic distortion.

An unfolding method can solve these issues. The problem is described mathematically by the Fredholm integral equation:

$$g(y) = \int M(x,y)f(x)dx + b(y), \tag{2.17}$$

where $g(y)$ is the distribution of the measured parameter,E_{est}; $f(x)$ is the distribution of the sought parameter, E_{true}; $M(x,y)$ is the *Migration matrix*; $b(y)$ is the background distribution. Equivalently, the equation can be written in a discrete form:

$$g_i = \sum_j M_{ij} f_j + b_i, \tag{2.18}$$

in this form, M_{ij} represents the probability that an event in the bin j of E_{true} is reconstructed in the bin i of E_{est}. To solve the problem is need to invert the migration matrix, however it is not always possible. In this situation it is used the least square method. The minimum value of χ^2_0 gives the solution for $\mathbf{f}$ which shows the best agreement with the data, the matrix form for χ^2_0 reads:

$$\chi^2_0 = (\mathbf{g} - M\mathbf{f})^T V|\mathbf{g}|(\mathbf{g} - M\mathbf{f}) \tag{2.19}$$

This method is valid only for Gaussian distributed data, and it is not efficient for a low number of events with a Poisson statistic. In addition, regularization methods are needed in order to produce acceptable results. A possible regularization is done by adding a regularization term Reg($\mathbf{f}$):

$$\chi^2 = \frac{1}{2}\chi^2_0\omega + \mathrm{Reg}(\mathbf{f}), \tag{2.20}$$

where ω is the strength of Reg($\mathbf{f}$).
In MARS, a possible unfolding command is `CombUnfold`; it performs the entire unfolding procedure, and it is possible to choose the regularization method between Tikhonov, Schmelling and Bertero methods, (Tikhonov and Arsenin, 1977; Schmelling, 1994; Bertero and de C. Mol, 1996).
Nevertheless, an alternative approach is using the command `fold`. It solves the Fredholm equation by a *forward unfolding*. At the beginning, a spectral shape is assumed and then χ^2_0 is minimized. The executable `fold`, differently from `CombUnfold`, gives spectra with a forward-folding Poissonian likelihood maximization. It takes the output of `flute` and calculated the best fitting parameters of the intrinsic source spectrum. Input information required regards the redshift, the energy range, the EBL model and the spectra function to be fitted. Different spectral shapes are allowed: power-law (PWL), log-parabola (LP), power-law with exponential cut-off (EPWL), log-parabola with exponential cut-off (ELP) and power-law with super-exponential cut-off (SEPWL).

Chapter 3

MAGIC analysis PKS 1424+240

This chapter focuses on the analysis of MAGIC data from a flaring state of the blazar PKS 1424+240, which is the central subject of this thesis. In addition, the results were validated through a cross-check analysis and compared with MAGIC archival data to ensure consistency. The observation of MAGIC were triggered by the *Fermi* Gamma-ray Telescope that observed high hardness in the spectrum.

3.1 Analysis Period

The MAGIC experiment started with a single telescope, and later it was upgraded with a second twin telescope; since then it is operating in stereoscopic mode. Nevertheless, significant hardware modifications and upgrade took place since then, which required upgraded in the analysis reconstruction chain that better describes the real performances of the instrument. Moreover, the telescopes performances charges over time and this affects the data quality and characteristics. Therefore, it is fundamental to select the correct MC observational period.
In this work, the observational period **ST.03.07** was selected. This time slot extends from the 29^{th} of April 2016 to the 2^{nd} of August 2017. Tab. 3.1 shows the available observation of PKS 1424+240 by the MAGIC telescopes.

Date	Zenith range (deg)	Observation time (hrs)
09/03/2017	5-35	~ 1.1
10/03/2017	5-35	~ 0.5

Table 3.1: Available observation of MAGIC of PKS 1424+240 during the observational period ST.03.07. The source was observed at low zenith both days.

The first step for standard analysis, i.e., it is used the standard image cleaning levels used by the OSA, consist into download the `superstar` files available from the PIC[1]; and apply `quate`, an executable in `Mars` that calculates the averages of a set of parameters over runs and performs data selection and classification, cuts in order to obtain good quality data. The following criteria were applied:

[1]Port d'Informació Científica

- Transmission at 9 km: >0.8;
- Cloudiness: <0.3;
- M2 DC: <2200 μA;
- L3 rates: from 150×A up to 400×A, A=cos(Zd)$^{-0.35}$.

After that, MC simulation were retrieved and separated into `train` and `test` MC, `wobblering mmcs699` were chosen. The mmcs (MAGIC Monte Carlo Simulation) is a special CORSIKA version modified for MAGIC, (Majumdar et al., 2005), based on CORSIKA 6.5 and 6.9, (Heck et al., 1998). It is possible to check these files on the MAGIC wiki page[2] and obtain them from the PIC server. The zenith range of the simulations spans from 5° to 62°. These files are in `superstar` format, divided in low (5°-35°), intermediate (35°-50°), and high (50°-62°) zenith; additionally it is present also a very high (62°-70°) zenith, nevertheless, it was not relevant for this case. Each folder contains 2 files (denoted with the numbers 1 and 2), a total of 12 file were downloaded and divided into train and test MC. The division of train and test is shown in Tab. 3.2.

mmcs	Zenith range (deg)	train	test
699	5-35	1	2
699	35-50	1	2
699	50-62	2	1

Table 3.2: Division in train and test MC, a total of 12 file were downloaded. The notation 1-2 is the same present in the folder containing the mmcs.

The next step was the selection of **OFF data**. These data must have the same quality condition, being observed during the same period, should not have significant γ emission, and cover the same zenith angles. Additionally, they should be of the same type, meaning Galactic or extragalactic sources, as the source to be analyzed, and the total time should be at least equal to the observational time of the source.
The sources selected for the OFF data are: PSR J2032, HESS 1912, GRB170306B, M87, 3C279, GRB170728, TXS 0637, GRB170604, NGC 1275, NGC 1068, PG 1553+113, Boomerang, OJ287, PSRJ2032+4127; for a total of $\sim$ 23 hours.
Once MCs and OFF data are correctly downloaded, the RF production can start by using the command `coach`, a `Mars` executable which does not process data, but produces several RF files, see Sec. 2.4.3.
Before performing the data analysis on PKS 1424+240, it was performed on the **Crab Nebula**. This source is used ad a standard candle in γ-ray astrophysics. The **Crab check** is usually done in order to check if the RF is correctly produced, (Aleksić et al., 2016b; Aleksić et al., 2012).

[2]https://wiki.magic.pic.es/index.php/Main_Page (internal page)

3.2 Crab Check

To analyze the Crab Nebula, the same quality conditions as PKS 1424+240 were chosen. The Tab. 3.3 shows the selected data for the Crab Nebula, the relative zenith range and observation time. Starting by running `melibea`, an executable in `MARS` that converts Hillas Parameter files or the stereo parameter files to fully analyzed Event files, to obtain files that can be analyzed at higher level; it used the RF previously generated. The results of `melibea` are then used in the following steps (`odie`, `caspar` and `flute`) to obtain graphical output and final results.

Date	Zenith range (deg)	Observation time (hrs)
27/12/2016	5-62	~ 4.4
28/12/2016	5-20	~ 1.7
30/12/2016	5-20	~ 0.6
01/01/2017	5-10	~ 0.1
02/01/2017	5-15	~ 0.2
03/01/2017	10-20	~ 0.3

Table 3.3: Crab Nebula data chosen for the Crab check for the ST.03.07 period, for a total of ∼6 hours before the quality cut.

The $\boldsymbol{\theta^2}$ **plots** are the first results from the executable `odie`, showing the significance of the signal in two different energy range, see Tab. 2.1 in the previous chapter (The MAGIC Telescopes). These plots represent the signal detection of the source, the parameter θ^2 used is the angular distance between the reconstructed position of the source and the real position.
The Crab Nebula is detected at low energy with a significance of 79.0σ, left Fig. 3.1, and full range with a significance of 57.1σ, right Fig.3.1. In both plots is present the characteristic small bump at 0.3 deg^2, it is connected with the method adopted for signal extraction. The significance at higher energy, meaning full range energy, is lower than the significance at low energy because the number of event is decreasing with increasing energy. For this same reason, also the background has a larger number of events at low energy, visually, higher bins in the histogram of the θ^2 plot.

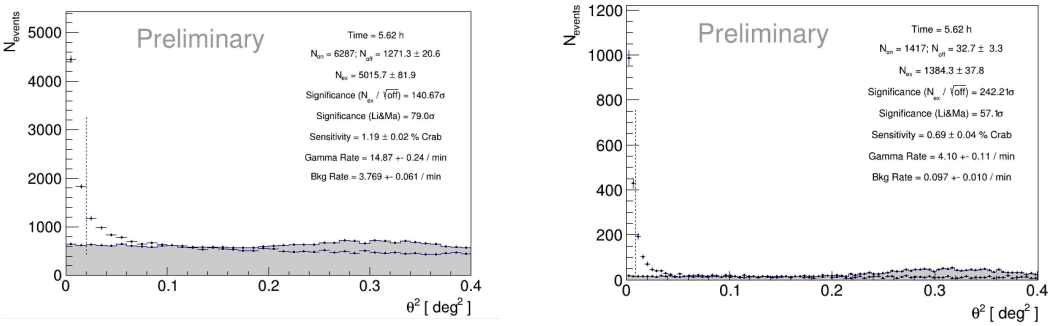

Figure 3.1: Crab Nebula `odie` θ^2 plots. Left: low energy θ^2 plot. Li&Ma significance of 79σ. Right: full range θ^2 plot. Li&Ma significance of 57.1σ. In both θ^2 plots, the gray area represents the estimated background, while the blue dots are related to the source emission. The characteristic small bump at 0.3 deg^2, present in both plots, is connected with the method adopted for signal extraction.

Another important result is the **skymap** built with the executable `caspar`. It can be shown in two forms: as a distribution of the **Test Statistic (TS) value** in the **Field of View (FoV)**, left Fig. 3.2; and as the **number of events (# bins)** against the **TS values**, right Fig. 3.2. In particular, the second representation is meaningful, the red line that follows a Gaussian profile is the *null hypothesis*, i.e, the background. While after TS value $\sim$4, the events that do not follow the Gaussian profile are the actual source emission. The fact that the null hypothesis follows a Gaussian shape indicates that the analysis has been successfully conducted.
The first representation shows that the TS distributions of the Crab Nebula emission on the camera, the source is clearly visible as a confirmation of the successful detection. Skymaps are relevant to check the PSF of the instrument; they do not have information on the detection significance as the θ^2 plots.

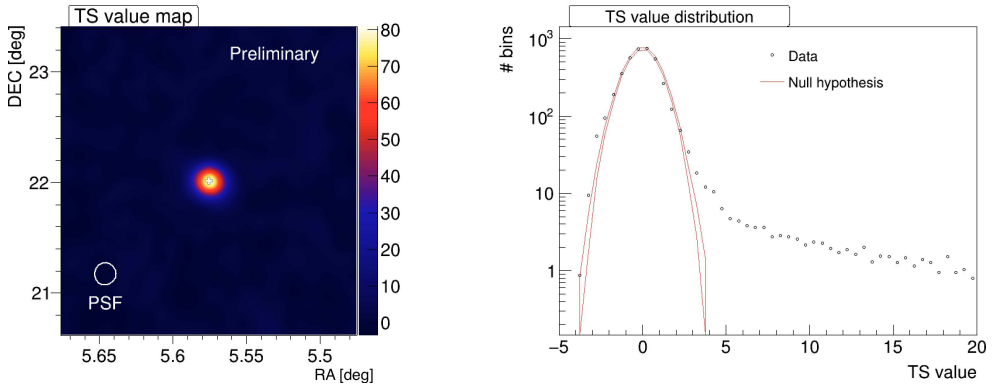

Figure 3.2: Crab Nebula `caspar` output: LE TS value map and TS value distribution. Left: LE skymap; the source is in the center of the camera, and the PSF of the telescopes is displayed in the lower left corner. By default, the color scaling is such that it turns red at 3σ and yellow at 5σ. Right: LE TS histogram; the red line that follows a Gaussian profile is the background (Null hypothesis), while after TS$\simeq$4, the events that do not follow the Gaussian profile are the actual source emission (Data).

The final results and graphical outputs are the **SED**, left Fig. 3.3 and the **light curve**, right Fig. 3.3, obtained by the executable `flute`. The SED can be further corrected with a unfolding technique (e.g., `fold`, `CombUnfold.C`), but this step is not required for the Crab check analysis.
The SED follows a **LogParabola** trend, in `flute` the default spectral shape for the Crab Nebula is:

$$\frac{d\phi}{dE} = \left(\frac{E}{E_0}\right)^{-2.31-0.61\log_{10}(\frac{E}{E_0})} \qquad E_0 = 150 \quad \text{GeV}, \tag{3.1}$$

and it is represented by the green lines; while the other line are related to previous studies of the Crab Nebula behavior.
The light curve above 150 GeV night-binned is the integral flux emitted by the source displayed against time in modified Julian Dates (MJD). Two different time binning options are present in `flute`: the most common is the *night-wise* light curve, and the other is the *run-wise* light curve, which is useful to check, e.g., for systematic effects coming from different positions of the source on the camera.
In both cases, the newly analyzed data match the archival result within the errors, implying the correctness of the RF production.

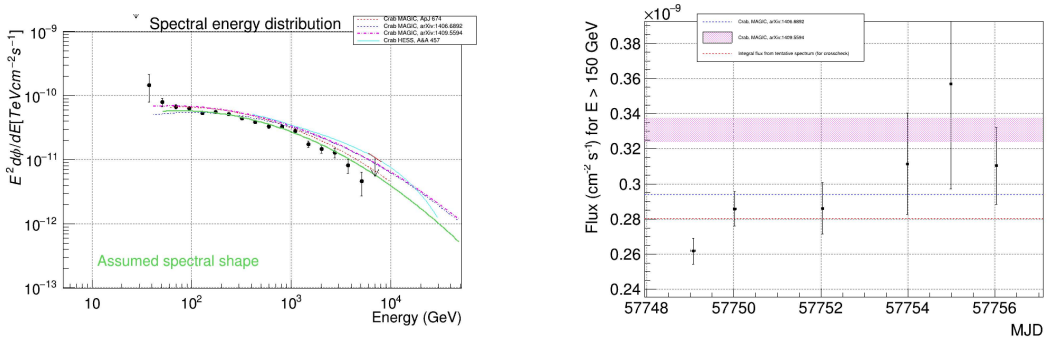

Figure 3.3: Crab Nebula `flute` output. Left: SED that follows a LogParabola trend; the assumed spectral shape is represented by the green line, the other lines are related to archival studies of the source. The black points are the actual data, while the arrow represent an upper limit. Right: night-binned light curve above 150 GeV; is the integral flux vs. time. The dashed lines represent archival MAGIC analysis result. In both plots, the newly analyzed points match the archive result, implying the correctness of the RF production.

3.3 PKS 1424+240 analysis results

Once the Crab check is done, and it is established the correctness of the RF production, the analysis of PKS 1424+240 data can start. The steps are the same described in Sec. 2.4 in the previous chapter (The MAGIC Telescopes), starting from the *intermediate stage* and following the steps for a standard analysis. Cleaned and calibrated data are retrieved from the PIC in `superstar` format, then they are filtered by applying quality cuts with the executable `quate`, the energy is reconstructed by the executable `melibea`. High level analysis results are obtained with the executable `odie`, `caspar`, `flute`, and `fold`. Differently from the Crab check, in this case the unfolding procedure is required.

The source was observed by MAGIC during the nights of 9^{th} and 10^{th} March 2017 for a cumulative time of ∼1.7 h (before quality cuts). The observation was triggered by *Fermi*-LAT that measured a high hardness in the spectrum. Indeed, the results of the analysis are compatible with a *flaring state*, having a flux of order of 4×10^{-11} cm^{-2} s^{-1}.
After the quality cuts were applied, the observational time is reduced to ∼1.5 h (both nights); most of the observational time during the second nights is not analyzable due to the presence of the moon, the full moon was few days after (12^{th} March 2017).

3.3.1 Signal Search

The first fundamental step is to check the **signal detection**. This procedure is done by the creation of **signal search** plots, which use the parameter θ^2, the angular distance between the reconstructed position of the source and the real position.
The following plot shows the signal search plots or θ^2 plots, obtained by the exe-

cutable `odie`; Fig. 3.4 display the low energy and the full range θ^2 plots, while Fig. 3.5 is a comparison of the two nights observed.
The important result is that the source is correctly detected with a cumulative significance of 5.5σ, meaning that the source emission is distinguishable from the background, over an observational time of $\sim$1.5h.
In particular, it is noticeable the fact that during the second night of observation, see right Fig. 3.5, the condition of observability were worse than the previous day, leading to a shorter observed time and lower significance. This deterioration of the quality is related to the presence of the moon, since the full moon was few days after (12^{th} March 2017). The MAGIC telescopes are IACTs, therefore this lowering in the quality of data, in the presence of moonlight, is a limit of the instrument itself.
In this case, the θ^2 plots have much less significance with respect the result of the Crab check, due to the fact that there are fewer hours of observation and the source is fainter and more distant. The Crab Nebula is a Galactic source with a distance of $\sim$1.7 kpc; while PKS 1424+240 is an extragalactic source having a redshift of $z \simeq 0.603$, (Goldoni, 2021). Especially in the full range energy range the source emission is not present, only the background is visible, see right Fig. 3.4. Therefore, further steps will be done only in the low energy range.

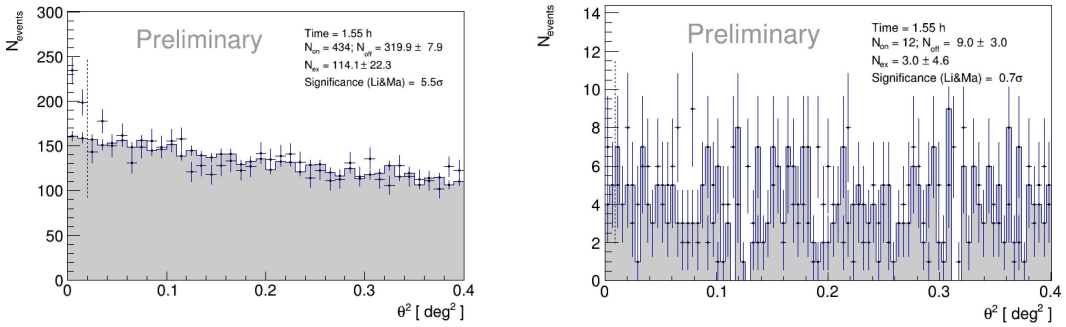

Figure 3.4: PKS 1424+240 `odie` θ^2 plots for a cumulative observational time of 1.55 h. Left: low energy θ^2 plot; Li&Ma significance 5.5σ, the source emission is still distinguishable from the background. The detection has been successful. Righ: full range θ^2 plot; Li&Ma significance 0.7σ; the source emission is not visible, the detection is background dominated. This result was expected since PKS 1424+240 is a distant VHE blazar.

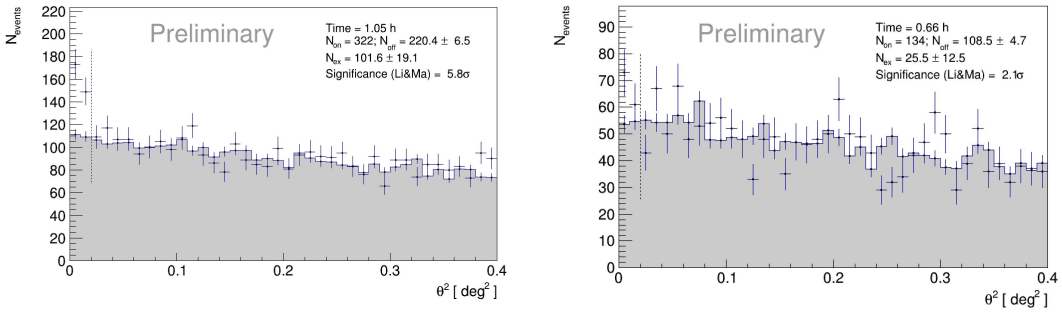

Figure 3.5: PKS 1424+240 `odie` low energy θ^2 plots, comparison of 9/03/2017 (left) having a Li&Ma significance 5.8σ and 10/03/2017 (right) having a Li&Ma significance 2.1σ. The significance is lower for the second night of observation, due to the observability condition. During the second night were significantly worst and due to that the observation time is reduced having effect of the significance. This deterioration of the quality is related to the short observational time and the presence of the moon.

Moving then to the **skymaps** produced by the executable `caspar`, the two dimensional skymap in left Fig. 3.6, and the TS histogram, right Fig. 3.6.
The important result is that the source is in the center of the source position (small white cross) meaning that the source was detected, and the image is symmetric, meaning that there were no issue during the observation. In the TS histogram, the background follow correctly a Gaussian profile and the source emission is a variation from the profile. These results have to be interpreted as the compatibility between the expected data and the observed data.

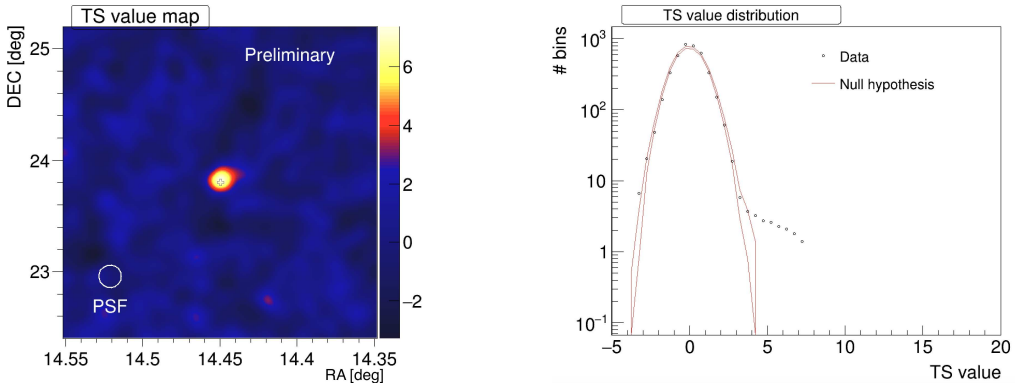

Figure 3.6: PKS 1424+240 LE `caspar` output: TS value map and TS value distribution. Left: LE skymap; the source is in the center of the source position (white cross), and the PSF of the telescopes is displayed in the lower left corner. By default, the color scaling is such that it turns red at 3σ and yellow at 5σ. The source was correctly detected, and no issue happened during the pointing of the source. Right: LE TS histogram; the red line that follows a Gaussian profile is the background (Null hypothesis), while after TS$\simeq$4, the events that do not follow the Gaussian profile are the actual source emission (Data). These results are compatible with the expected values.

3.3.2 Spectral Energy Distribution and Light Curve

Then it is time to build the SED and the light curve, both these results are produced by the executable `flute`. For this step, both the `melibea` files from the actual observations and those from an adequate MC sample are needed. The MC will be used to characterize the instrument performance (e.g., collection area, energy resolution) which allows converting the observed excess event rates into estimates of the source flux. One of the most critical aspects in the flux calculations is the estimation of the background to be subtracted from the number of events observed in the ON region defined around the candidate source; from this subtraction, an estimation of the number of observed γ-rays is obtained, see Sec. 2.4.4 in the previous Chapter for more details.

The left plot in Fig. 3.7 is the SED, while the right plot in Fig. 3.7 is the light curve; it is visible the distinction between the spectral shape of the Crab Nebula and PKS 1424+240.
In this case, the assumed spectrum follows a **power law**:

$$\frac{d\phi}{dE} = \left(\frac{E}{E_0}\right)^{-3.5} \qquad E_0 = 100 \quad \text{GeV}. \tag{3.2}$$

In both plots **upper limits** are present, they are computed when the signal is not revealed due to poor significance. The causes may be the short observation time and/or the faintness of the source. The maximum relative error used to construct upper limits was set to be standard (i.e., 0.5). The energy threshold for the integral flux computation is lower than the one used for the Crab Nebula because PKS

1424+240 has a steeper spectrum.
In the light curve, the only point present is of the order 4×10^{-11} cm^{-2} s^{-1}, compatible with a flaring state.

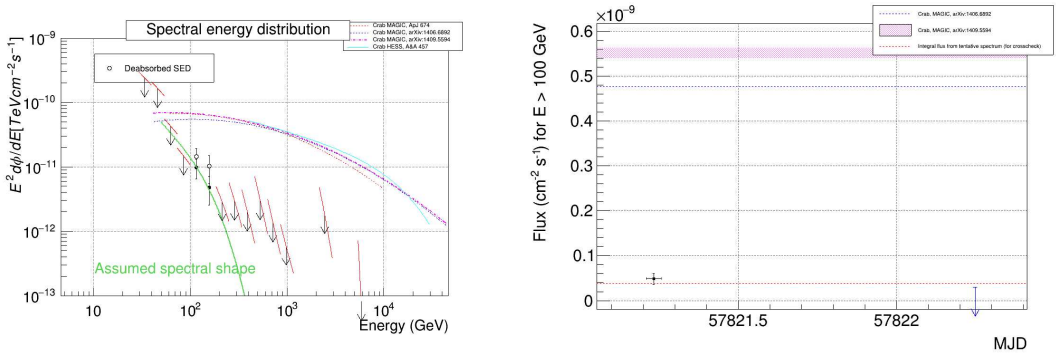

Figure 3.7: PKS 1424+240 `flute` output. Left: SED that follows a power law trend; the assumed spectral shape is represented by the green line, the others lines represent the Crab Nebula archival studies. The black points are the actual data, while the arrows represent upper limits. Right: night-binned light curve above 100 GeV; is the integral flux vs. time. The dashed lines represent archival MAGIC analysis result of Crab Nebula. The only point present is compatible with a flaring state. The low significance found in the θ^2 plots has consequence in both SED and light curve.

3.3.3 Deabsorbed Spectral Energy Distribution

Differently from the Crab check, an **unfolding** technique is needed in order to produce final results. The executable `fold` is used to obtain spectra via forward-folding Poissonian Likelihood maximization; it takes as input the output form `flute` and calculates the best-fitting parameters of the intrinsic source spectrum. Basically, the intrinsic spectrum is build starting from the estimated spectrum.
The assumed spectral shape is a power law:

$$\frac{d\phi}{dE} = f_0 \Big(\frac{E}{E_0} \Big)^{-p}, \tag{3.3}$$

where E_0 is a normalization for the energy [GeV], it is suggested by the program in order to minimize the correlation between the spectral parameter; f_0 is a normalization constant and p is the spectral index, they are obtained by a fit procedure with the data, see Tab. 3.4.

$f_0 \times 10^{-10}$	p	E_0 [GeV]	χ^2
4.71±2.06	-2.57±0.76	153.86	4.92

Table 3.4: PKS 1424+240, fit results; E_0 is a normalization for the energy suggested by the program in order to minimize the correlation between the spectral parameter; f_0 is a normalization constant and p is the spectral index; χ^2 is a test that measures how a model compares to actual observed data.

The results of `fold` are the spectral parameters with their uncertainties. Additionally, the **fold outputs** display a spectrum and SED with individual points, obtained from the excess rates measured in bins of estimated energy, and converted into flux points using a collection area which contains a *spillover correction*, calculated using best-fit spectrum, see Fig. 3.8.
In addition to the data points, to build properly the intrinsic spectrum the redshift and the EBL model are needed. For this analysis, the redshift of PKS 1424+240 used is $z = 0.603$, evaluated by Goldoni (2021); and the EBL model used is the model of Domìnguez et al. (2011).
The diffuse EBL[3] is all the accumulated radiation in the universe, this radiation covers almost the whole electromagnetic spectrum, except the microwave, which is dominated by the primordial CMB[4]. After the CMB, the EBL produces the most energetic diffuse background. The understanding of the EBL is also fundamental for extragalactic VHE astrophysics, since VHE γ-ray photons interact with the EBL and product an $e^{\pm}$ pair, causing an attenuation in the observed flux. This interaction significantly impacts the detectability and measurement of distant VHE sources, as the pair production process absorbs part of the photons, leading to a reduction in the observed intensity.
In this step, significant spectral points are re-calculates, taking into account the fitted function it obtains (to recalculate the effective area). Points will be calculated only for E_{est} bins which were shown in the spectrum by `flute`, those with a significant enough excess. The spectral points are placed at the median E_{true} (calculated from MC) of the excess events of each E_{est} bin.

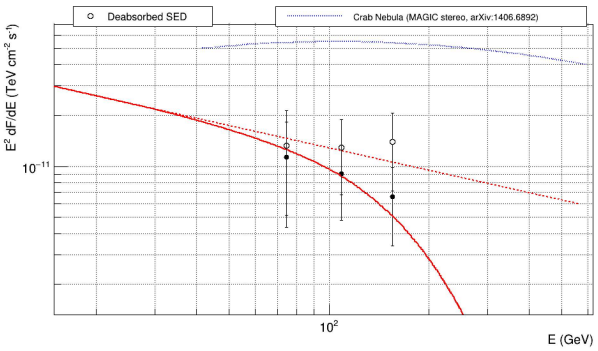

Figure 3.8: PKS 1424+240 `fold` output, SED produced with the forward-folding technique. The full dots are the observed points, while the empty points are the deabsorbed bins, $z = 0.603$ and EBL model from Domìnguez et al. (2011). The blue dashed line is from archival data related to the Crab Nebula; while the red is associated to the best fit of PKS 1424+240.

The alternative executable `CombUnfold` performs the unfolding of the energy distribution to estimate the true energy of an event from its reconstructed energy by making use of experimental technical performance. The result of `CombUnfold` and

[3]Extragalactic Background Light
[4]Cosmic Microwave Background

a comparison with several unfolding methods such as forward folding, the Tikhonov method (Tikhonov and Arsenin, 1977), the Bertero method (Bertero and de C. Mol, 1996) and the Schmelling (Schmelling, 1994), are shown in Fig. 3.9. This confirms the stability of the result obtained.

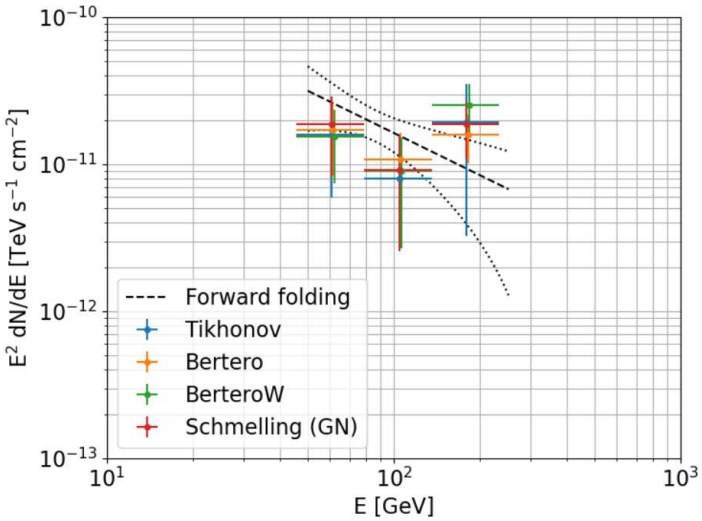

Figure 3.9: PKS1424+240 `CombUnfold`, SED comparison between various unfolding methods, such as the forward folding, the Tikhonov method (Tikhonov and Arsenin, 1977), the Bertero method (Bertero and de C. Mol, 1996) and the Schmelling (Schmelling, 1994). The SEDs are also corrected for EBL absorption with z = 0.603, using the model from Domìnguez et al. (2011). Done by D. Cerasole.

3.3.4 Crosscheck Analysis

A fundamental step of the MAGIC data analysis is the **crosscheck** evaluation, meaning that two analyzers study the same data set. Then the comparison of the results must be added to a specific page on the wiki MAGIC. This step is essential to have a comparison of the analysis and to check the correctness of the results. The two analyses must show compatible result in order to be accepted, and the different steps of the analysis should be done following the same criteria. For this project, the second analyzer was Dr. Davide Cerasole (INFN, University of Bari).
In Fig. 3.10 two tables of signal search results are displayed. The tables show the observed time and significance, divided into night of observation (single night and stacked nights) and by energy range (low energy and full range). For both data sets, a background estimation with 3 and 5 OFF region was performed, resulting that the analysis with 5 OFF has a better sensitivity. The worst data quality during the second night is clearly visible from the low significance around 2σ in both 3 and 5 OFF analyses. The results are in agreement, meaning that the analysis was correctly done.

Date	Teff [h]	Sign. LE	Sign. FR	Comment
2017-03-09	1.05	5.31	0.41	3 OFF regions
2017-03-09	1.05	5.81	0.84	5 OFF regions
2017-03-10	0.66	2.12	0.33	3 OFF regions
2017-03-10	0.66	1.68	0.48	5 OFF regions
Stacked	1.55	5.12	1.24	3 OFF regions
Stacked	1.54	5.51	1.34	5 OFF regions

Date	Teff [h]	Sign. LE	Sign. FR	Comment
2017-03-09	1.05	2.94	1.82	3 OFF regions
2017-03-09	1.05	5.12	1.81	5 OFF regions
2017-03-10	0.48	1.99	0.09	3 OFF regions
2017-03-10	0.48	2.10	1.06	5 OFF regions
Stacked	1.54	3.63	1.35	3 OFF regions
Stacked	1.54	5.61	1.64	5 OFF regions

Figure 3.10: PKS 1424+240 `odie` results comparison. The left table are my analysis results, while the right table is done by the second analyzer (D. Cerasole). The first column is the date, related to the single night of observation and staked together. The second is T_{eff}, which shows the observed time in hours. Then the third column is related to the LE range, while the forth to the FR. Lastly, the fifth column regard the number of OFF region, 3 or 5. The results of the two analysis are compatible, minor difference are present.

In Tab. 3.5 two tables of results of the light curve estimation are compared. It shows the integral flux and the relative error for both nights, the time is expressed in MJD[5]. For the second night, an upper limit was found, and it is displayed also the integral flux relatively to the upper limit with 95% of confidence level. For both analyses during the first night, a flux of $\sim 4 \times 10^{-11}$ cm^{-2}s^{-1} was registered, while the upper limit is compatible with zero. This result is compatible with a flaring state of the source during the first night.

MJD	Flux (cm^{-2}s^{-1})	Flux error (cm^{-2}s^{-1})	Flux 95% UL (cm^{-2}s^{-1})
57821	4.83 $\times 10^{-11}$	1.24 $\times 10^{-11}$	
57822	-2.08 $\times 10^{-11}$	1.99$\times 10^{-11}$	2.95 $\times 10^{-11}$

MJD	Flux (cm^{-2}s^{-1})	Flux error (cm^{-2}s^{-1})	Flux 95% UL (cm^{-2}s^{-1})
57821	3.84 $\times 10^{-11}$	1.49 $\times 10^{-11}$	
57822	7.71 $\times 10^{-12}$	1.94$\times 10^{-11}$	6.08 $\times 10^{-11}$

Table 3.5: PKS 1424+240 `flute` results comparison. The upper table are my analysis results, while the bottom table is done by the second analyzer (D. Cerasole). The first column is the date expressed in MJD; the second column is the integral flux value, in both case the measurable value is of the order of $\sim 4 \times 10^{-11}$ cm^{-2}s^{-1}; while the second value is an upper limit compatible with zero; the third column is the error relatively to the integral flux; and the last column is the integral flux relatively to the upper limit (UL) with 95% of confidence.

The results of reconstruction of the intrinsic spectrum are compared and showed in Fig. 3.11. The integral flux values are in agreement, the difference in energy is due to a different binning in energy arising from the executable used for the analyses. These values are the same showed in Fig. 3.8.

[5]Modified Julian Dates

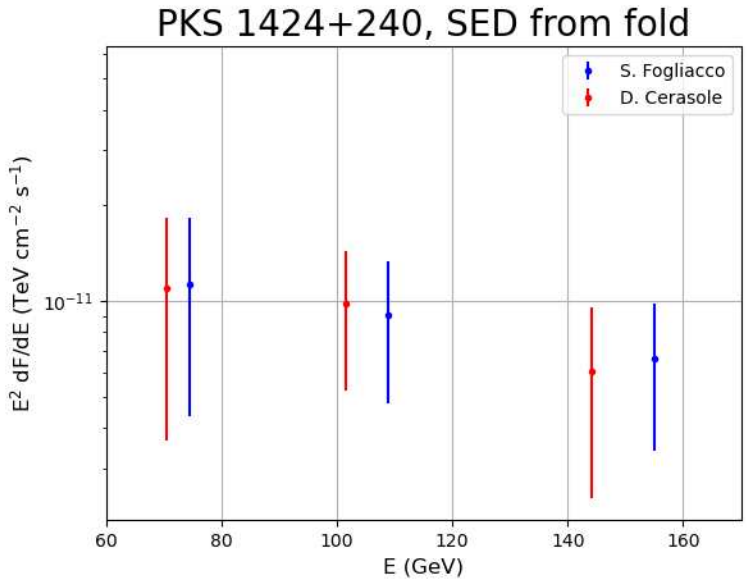

Figure 3.11: PKS 1424+240 `fold` result crosscheck. The points with the relative errors are from the unfolding step. The integral flux values are in agreement, the difference in energy is due to a different binning in energy.

3.4 MAGIC past observations

The blazar PKS 1424+240 has already been observed and studied by the MAGIC telescope, by Aleksić et al. (2014), and by Acciari et al. (2019, 2020). Respectively, the first paper is a long term study over a span of ∼3 years (2009-2011), while the second and third papers cover the two-years period of 2014-2015. Before staring a brief review of the main results obtained in these two past study, it must be said that the redshift of PKS 1424+240 (z=0.603) was evaluated recently, (Goldoni, 2021), therefore, in both papers different values were used.

The following information and results, arise from Aleksić et al. (2014).
The source was observed from April to June 2009 in single-telescope mode (only MAGIC-I was active) and then in stereo mode during the spring of 2010 and 2011, when MAGIC-II was in commissioning phase. The source was observed in good condition, covering a zenith angle range between 4° and 36°. The observed time is 12.5 h in 2009 (mono), 11.6 h in 2010, and 9.5 h in 2011. During the last two year, when the stereoscopic mode was available, the data sample was taken in wobble mode (false-source tracking). This mode can take both source and background data at the same time.
The signal search, i.e., the production of θ^2 plots, has a stacked significance of the whole data sample of $\sim 7\sigma$, while the single sample result are shown in the Tab. 3.6, where the year of observation, the observed time, the energy threshold E_{th}, the number of excess events N_{exc} and the significance of the signal are reported. The energy threshold E_{th} is defined as the energies where the number of MC γ-ray events

with assumed spectral indices is maximized in the histogram of the image size, 150 GeV was chosen for the first year, and 100 GeV for the other two years. The number of excess events N_{exc} is calculated as the difference between the number of ON event and OFF event ($N_{exc} = N_{ON} - N_{OFF}$).

Year	Observed Time [h]	E_{th} [GeV]	N_{exc}	Significance
2009	12.5	150	489	4.6σ
2010	11.6	100	330	4.8σ
2011	9.5	100	333	5.5σ

Table 3.6: Characteristics and signal result of PKS 1424+240, from Aleksić et al. (2014). The year of observation, the observed time, the energy threshold E_{th}, the number of excess events N_{exc} and the significance of the signal are listed.

Then the differential energy spectrum was fitted with a power law:

$$\frac{dN}{dE} = f_0 \Big(\frac{E}{200\text{GeV}}\Big)^{\Gamma} \qquad \text{ph cm}^{-2}\ \text{s}^{-1}\ \text{TeV}^{-1}, \tag{3.4}$$

the fit parameters are shown in Tab. 3.7. The resulting spectrum is shown in Fig. 3.12.

Year	Fit range [GeV]	f_0 [cm^{-2} s^{-1} TeV^{-1}]	Γ	$F(>150\text{GeV})$ [cm^{-2} s^{-1}]
2009	150-400	$(1.3 \pm 0.6_{stat} \pm 0.4_{sys}) \times 10^{-10}$	$5.0 \pm 1.7_{stat} \pm 0.7_{sys}$	$(1.66 \pm 0.50) \times 10^{-11}$
2010	100-300	$(0.5 \pm 0.2_{stat} \pm 0.1_{sys}) \times 10^{-10}$	$3.5 \pm 1.2_{stat} \pm 0.5_{sys}$	$(0.53 \pm 0.25) \times 10^{-11}$
2011	100-400	$(1.0 \pm 0.3_{stat} \pm 0.2_{sys}) \times 10^{-10}$	$3.9 \pm 0.9_{stat} \pm 0.2_{sys}$	$(1.00 \pm 0.30) \times 10^{-11}$

Table 3.7: Power-law spectrum of PKS 1424+240, fit parameters and integral flux value, from Aleksić et al. (2014).

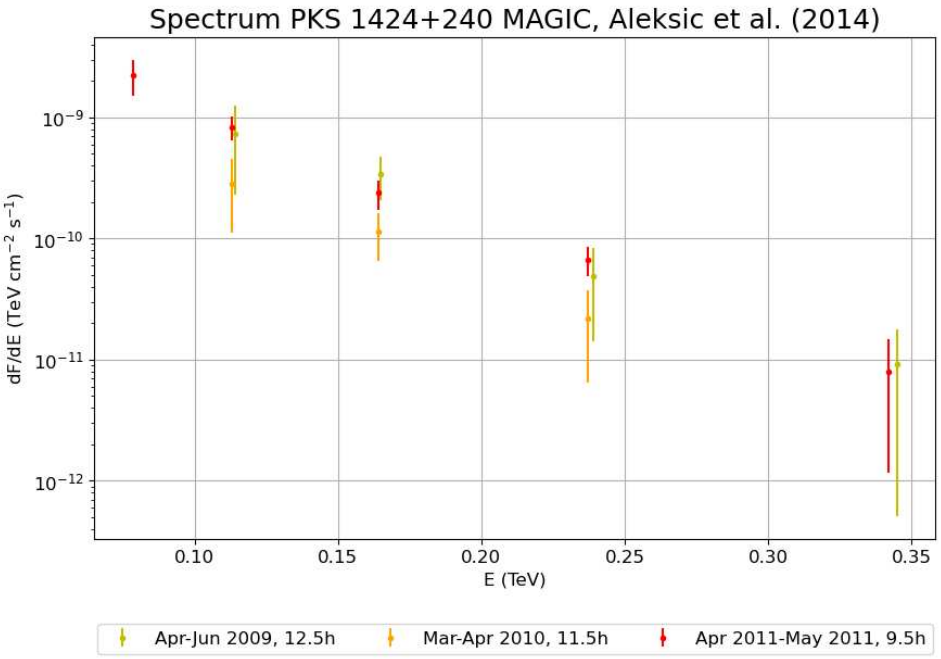

Figure 3.12: Differential energy spectrum of PKS 1424+240, from Aleksić et al. (2014). The energy spectrum flux, expressed in TeV^{-1} cm^{-2} s^{-1}, vs energy, expressed in TeV, relatively to the year 2009 (yellow), 2010 (orange) and 2011 (red) observed by MAGIC.

The second paper Acciari et al. (2019) had the aim to estimate the EBL based on a joint likelihood analysis of 32 gamma-ray spectra for 12 blazars (PKS 1424+240 included), while the third paper by Acciari et al. (2020) has the focus on the modelling of the SED, therefore it will be also mentioned in one on the next chapters (Spectral Energy Distribution modelling).
Nevertheless, some information on the spectrum can be extracted. PKS 1424+240 was observed between March and June in the 2014, and between January and June in the 2015, for a cumulative time of 49.1 h. The two observation year is divided into two campaign, since the VHE γ-ray flux observed in 2015 was the 60% of the flux observed during 2014. Also, two different models were applied, a power law for the 2014 data and a log-parabola for the 2015 data.

$$\frac{dF}{dE}(E) = F_0\left(\frac{E}{E_0}\right)^{-\Gamma} \qquad \text{simple power law} \tag{3.5}$$

$$\frac{dF}{dE}(E) = F_0\left(\frac{E}{E_0}\right)^{-\Gamma-\beta\log_{10}\frac{E}{E_0}} \qquad \text{log-parabola} \tag{3.6}$$

where F_0, Γ and β are respectively the flux at the normalization energy E_0, the spectral index, and the curvature parameter of the spectrum at E_0; their value are included in the Tab. 3.8. For both years, the threshold energy was set at 150 GeV, and the flux above the threshold for the 2014 and 2015 was $1.1 \pm 0.2 \times 10^{-11}$ cm^{-2} s^{-1} and $0.6 \pm 0.2 \times 10^{-11}$ cm^{-2} s^{-1}, respectively. The spectrum observed by MAGIC

is shown in Fig. 3.13

Year	Model	E_0 [GeV]	F_0 [10^{-11} cm^{-2} s^{-1}]	Γ	β
2014	power-law	111	98.0± 6.5	2.77±0.16	
2015	log-parabola	104	82±15	2.19±0.52	1.93±0.87

Table 3.8: Best-fitted model of PKS 1424+240 divided by campaign, the table shows the normalization energy E_0, the spectral index, and the curvature parameter of the spectrum at E_0. All the spectral parameters were calculated considering the EBL absorption, model by (Domìnguez et al., 2011), by Acciari et al. (2019, 2020).

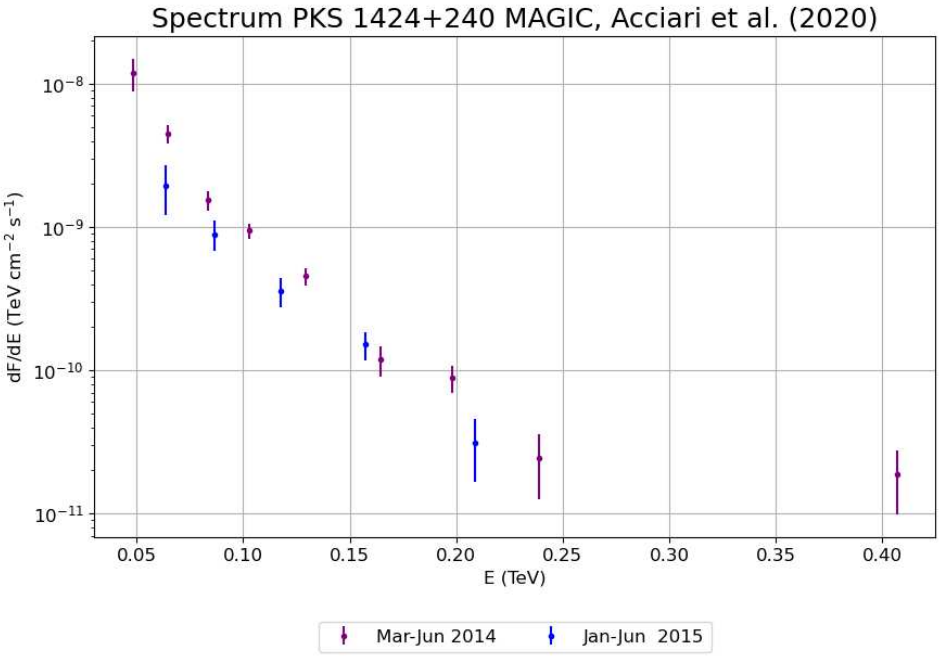

Figure 3.13: Differential energy spectrum of PKS 1424+240, from Acciari et al. (2019, 2020). The energy spectrum flux, expressed in TeV^{-1} cm^{-2} s^{-1}, vs energy, expressed in TeV, relatively to the year 2014 (purple), 2015 (blue) observed by MAGIC.

In conclusion, the source was observed in a flaring state during the 2009 and 2017, it will be confirmed by the observation in the X-ray band in the next chapter (Multiwavelength Analysis PKS 1424+240). The comparison between MAGIC archival data and MAGIC data analyzed in this thesis is shown in Fig. 3.14. The results obtained in this work are compatible with the past result, a last and final check to confirm the correctness of the analysis.

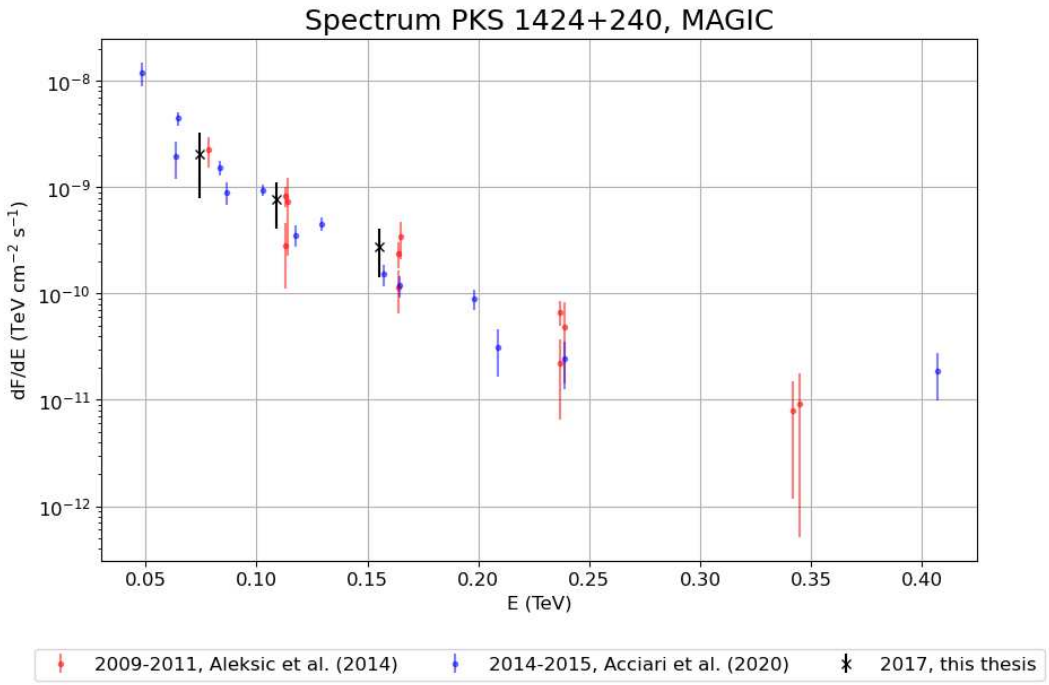

Figure 3.14: Differential energy spectrum of PKS 1424+240 observed by MAGIC from 2009 to 2017. The energy spectrum flux, expressed in TeV^{-1} cm^{-2} s^{-1}, vs energy, expressed in TeV. The red points (2009–2011 data) are relatively to the study by Aleksić et al. (2014), the blue points (2014–14 data) are relatively to the study by (Acciari et al., 2020), and the black crosses (2017 data) are the result of the analysis done in this thesis.

Chapter 4

Multiwavelength Analysis PKS 1424+240

This chapter focuses on the multiwavelength analysis. To obtain a comprehensive understanding of the source's behavior, data from various instruments were gathered. A multiwavelength light curve was constructed, spanning the electromagnetic spectrum from the radio band to very high energy gamma rays.
The analysis of the multiwavelength data is a crucial step for the modelling and a better comprehension of the source and its time variability.
In order to build a meaningful spectrum, some criteria must be followed; the most important one is the simultaneity of the observations, meaning that observations in different bands should be performed in close time windows. The simultaneity is required since these sources are very variable during time.

4.1 Radio Band

The radio astronomy was born with the discovery of the existence of radio waves by Hertz in 1888, (Schwab and Fischer, 1998). In the beginning bright sources such as the Sun were studied without positive results, however, in 1933 Jansky at Bell Labs discovered cosmic radio waves originating from the Milky Way, (Jansky, 1933).

OVRO

The **Owens Valley Radio Observatory (OVRO)**[1] is one of the largest radio observatories active nowadays, see Fig. 4.1. The observatory was built in the 1960s, and it is operated by the Astronomy department of the California Institute of Technology. Also called the *Big Ears*, the observatory is located near Bishop, California, on the east side of the Sierra Nevada. In the beginning of 2000, a new program was proposed and the OVRO 40m Telescope Monitoring Program started. This monitoring program, begun in 2008 and discontinued in 2020 due to lack of funding, has led to numerous publications (about one publication per month). AGNs have

[1] https://sites.astro.caltech.edu/ovroblazars/

been considered as candidate for neutrino emission since long time, and OVRO is a unique facility able to test the hypothesis whether neutrinos detected with the IceCube experiment originate from radio-loud AGN. The new proposed OVRO AGN multi-messenger monitoring program has monitored over 5500 AGN, mostly blazars, at present time. For this thesis, it were used data from the 40 m diameter telescope that performs radio measurements at a frequency of $\nu = 1.5{\times}10^{10}$ Hz.

Figure 4.1: OVRO 40 m telescope, performing at $\nu = 1.5{\times}10^{10}$ Hz, located near Bishop, California, on the east side of the Sierra Nevada. From OVRO web page[2].

The OVRO light curve data of PKS 1424+240 were requested (retrieved in April 2024) to build the multiwavelength light curve. Fig. 4.1 shows the light curve of PKS 1424+240 observed by OVRO. The source was observed with regularity from 2009 up to 2023. OVRO light curve has a better quality with respect to the other wavebands, this is due to the monitoring program started around 15 years ago. There is no exactly simultaneity with the MAGIC data set analyzed, the closest observation was the night before the interested period (8^{th} March 2017). The flux is expressed in Jansky (Jy), however, the conversion is related to a factor 10^{-23} as follows:

$$1 \quad \text{Jy} = 10^{-23} \quad \text{erg cm}^{-2}\ \text{s}^{-1}\ \text{Hz}^{-1} \tag{4.1}$$

therefore, the difference is just a scale factor.
A first noticeable result from the radio light curve is the timescale of the variability of the source. The blazar is variable over a span of several years.

[2]https://www.ovro.caltech.edu

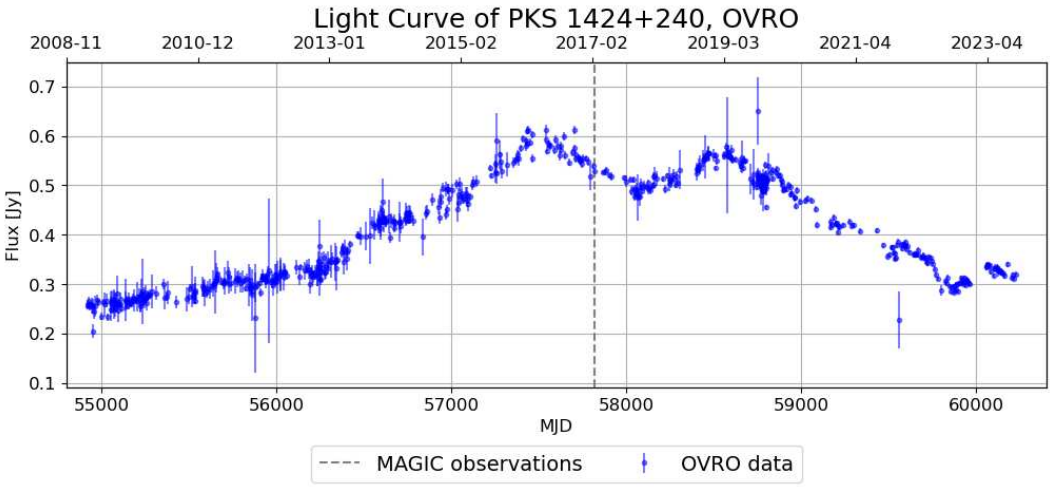

Figure 4.2: OVRO 40 m light curve of PKS 1424+240. The radio data are represented by the blue dots, while the gray dashed line represents the observed nights by MAGIC. On the x-axis, both MJD and UTC are displayed, lower and upper axis, respectively. The flux intensity is given in Jy. Courtesy of OVRO 40m Telescope[3].

4.2 Optical Band

Optical band refers to the range of radiation that is visible to the human eye. This is also known as the visible spectrum and typically covers wavelengths included in the range 380-750 nm. The optical band is further divided into specific sub-bands or filters, such as the B-band at 445 nm, the V-band at 551 nm and the R-band at 658 nm, (Smith, 2014).

Tuorla Observatory

At the **Tuorla Observatory**[4] is located in Piikkiö, near Turku, Finland. The observatory was founded in 1952 and has since been involved in various research areas, including the blazar optical monitoring.
The **Tuorla blazar monitoring** consists in several optical experiments:

- the 35 cm telescope at the KVA observatory on La Palma, Canary island, Spain;
- the 1.03 m telescope at Tuorla Observatory, Finland;
- the 50 cm Searchlight Observatory Network telescope, San Pedro de Atacama, Chile;
- the 40 cm Searchlight Observatory Network telescope, New Mexico, USA;

[3]https://sites.astro.caltech.edu/ovroblazars/
[4]https://users.utu.fi/kani/1m/

- the 60 cm telescope at Belogradchik, Bulgaria;
- the 80 cm Joan Oró Telescope at Montsec Astronomical Observatory, Spain.

All data are taken through the Cousins R-filter, it is part of the Johnson-Cousins UBVRI system, which extends the original Johnson UBV system to include the red (R) and infrared (I) bands, see Fig. 4.3. The FOV[5] is 12 arcmin.
This monitoring program, as the OVRO one, started in the beginning of 2000 was a innovative method to study variable object such as blazars.

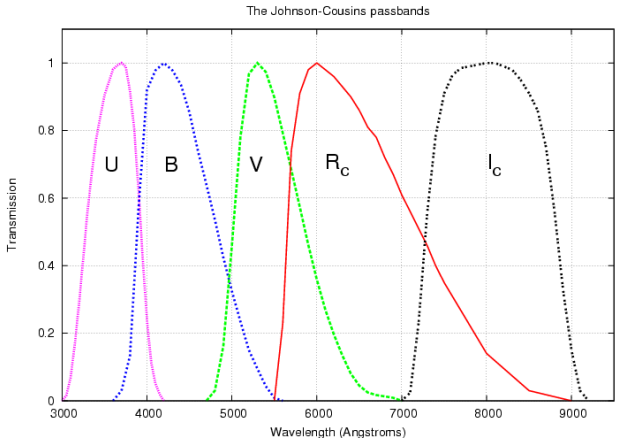

Figure 4.3: Johnson-Cousins UBVRI filter curves. Extension to the original Johnson UBV (Ultraviolet-Blue-Visible) system to include the red (R) and infrared (I) bands. From Tawalbeh and Al-Wardat (2018).

The optical light curve data of PKS 1424+240 were requested to the Tuorla Observatory (retrieved in August 2024) to build the multiwavelength light curve. Fig. 4.4 shows the light curve of PKS 1424+240 observed by the Tuorla blazar monitoring program. The source was observed quite regularly since 2004 up to 2023. It is no present exact simultaneity with the MAGIC observation, but the source was observed in by Tuorla during the same week during March 2017.
Similar to OVRO, the flux is expressed in Jy, the conversion present in Eq. 4.1 can be used to convert it; and again the good quality of the light curve is associated to the long monitoring program.
Also in this case, the first feature that can be extracted from the plot is the variability of the source. Similar to the radio light curve, the optical light curve has a long time variability, on a shorter scale than the radio case.

[5]Field Of View

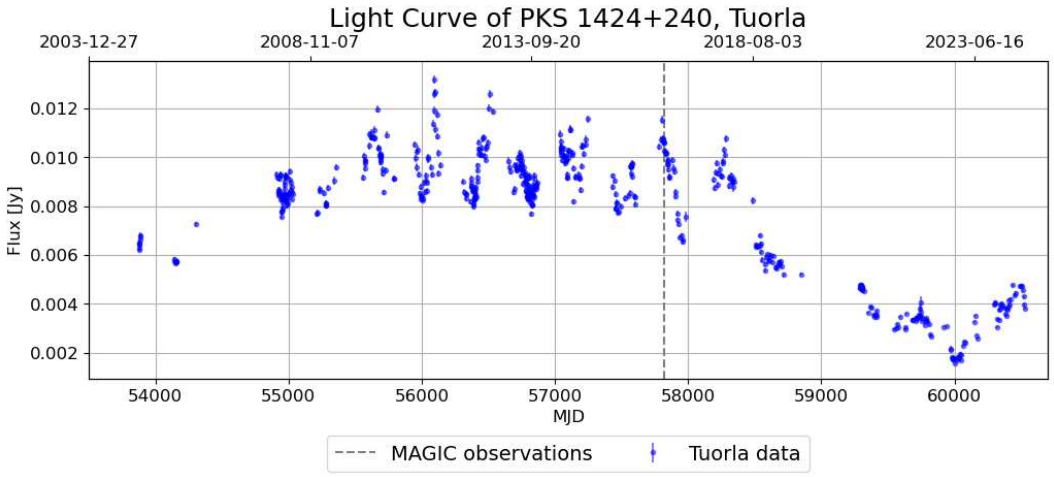

Figure 4.4: Tuorla light curve of PKS 1424+240. The optical data are represented by the blue dots, while the gray dashed line represents the observed nights by MAGIC. On the x-axis are displayed both MJD and UTC, lower and upper axis, respectively. The flux intensity is given in Jy. Courtesy of Tuorla Observatory blazar monitoring[6].

4.3 X-Ray Band

The X-ray band has wavelengths ranging 0.01-10 nm, or equivalently between 0.1 and 100 keV. The X-ray band is typically divided into two main categories: *soft* X-rays (0.1-10 keV) and *hard* X-rays (10-100 keV), (Arnaud et al., 2011). It was discovered by Röntgen (1896) that named it X-radiation to signify an unknown type of radiation.
X-rays interact with matter through *photoabsorption* (soft X-rays), *Compton scattering* (hard X-rays), and *Rayleigh scattering*.
To remark, two important active telescopes that will not be used in this thesis since no data were available for the interested blazar PKS 1424+240:

- *eROSITa* detecting energy range of 0.2 to 10 keV, soft X-rays;
- *INTEGRAL* detecting energy range of 15 keV to 10 MeV, hard X-rays (and low energy γ-ray); furthermore, the energy range observed fall in between of the two bump of emission where the detection is not possible with actual sensitivity.

Swift-XRT

The X-ray instrument of the Neil Gehrels *Swift* Observatory is the ***Swift* X-ray Telescope (XRT)**, a schematic representation of the instrument is shown in Fig. 4.5. The *Swift*-XRT aims it to measure fluxes, spectra, and light curve of Gamma-ray Bursts (GRBs) and afterglows covering more than seven orders of magnitude

[6]https://users.utu.fi/kani/1m/

in flux. The instrument has an effective area of 110 cm^2 (at 1.5 keV), a FOV of 23.6×23.6 arcmin, a resolution at half-power diameter of 18 arcsec, and, a energy range between 0.2-10 keV. The XRT uses a grazing incidence Wolter 1 telescope to focus X-rays onto a state-of-the-art CCD, (Burrows et al., 2000).

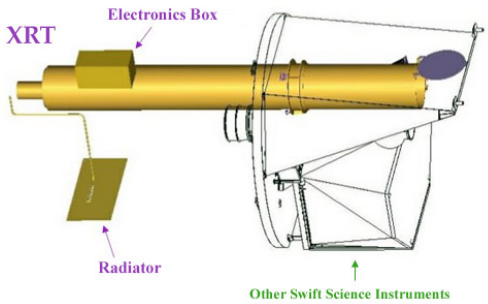

Figure 4.5: Schematic representation of *Swift*-XRT. The configuration of the mirror is a Wolter 1. From Swift web page[7].

Swift-XRT light curve data are free to access, and it is possible to build light curve and spectra from the repository[8] (retrieved in April 2024). XRT has different operating modes, depending on the brightness of the source being observed, for PKS 1424+240 two were available: Windowed Timing (WT) mode and Photon Counting (PC) mode. The WT creates 1-dimensional imaging with 1.8 ms time resolution and full energy resolution; while the PC generates 2-dimensional imaging with 2.5 s time resolution and full energy resolution; for this thesis, only PC data were considered. The available light curve data cover the time interval from 2009 up to 2023. The source PKS 1424+240 was observed with variable time interval. Two flaring state are visible in the light curve, one happened in April 2009 and the second during March 2017, see Fig. 4.6. The second flare is the interesting one for this project, the observations are quasi simultaneous with the analyzed MAGIC data set. Differently from radio and optical band, the variability of the X-ray light curve is faster, daily timescale; this characteristic is correlated with a different emission zone.
The energy flux is measured in *count rate*, meaning counts per second of single photons.

[7]https://swift.gsfc.nasa.gov/about_swift/xrt_desc.html
[8]https://www.swift.ac.uk/user_objects/

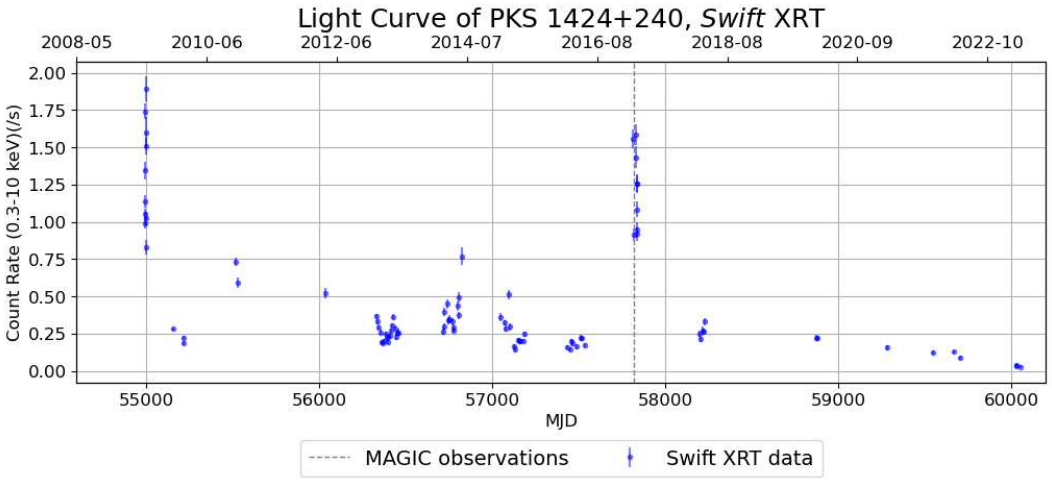

Figure 4.6: *Swift*-XRT light curve of PKS 1424+240. The x-ray data are represented by the blue dots, while the gray dashed line represents the observed night by MAGIC. On the x-axis are displayed both MJD and UTC, lower and upper axis, respectively. The intensity of the flux is given in count rates. Two flaring state are visible, the second one happened in March 2017 and the observations are quasi simultaneous with MAGIC. Data retrieved from The Neil Gehrels Swift Observatory[9].

4.4 High Energy Gamma-Ray Band

Gamma rays can be classified on the photons' energy, as it was mentioned in Sec. 1.2 in the first chapter (Introduction), and high energy γ-rays have energy in between tens of MeV and 100 GeV. In this energy range, the main interaction between photons and matter are: the *photoelectric effect* dominant below MeV; the *Compton scattering* dominant between few MeV and few tens of MeV; and the *pair creation* dominant above tens MeV, (Spurio, 2014).
Most of the γ-ray telescopes detect signal via pair creation. In this process, a high energetic photon is converted into an electron/positron couple. Nevertheless, the above-mentioned INTEGRAL, detects low energy γ-ray via coded mask technique, which allows imaging and provides background subtraction.

Fermi Gamma-ray Telescope

The ***Fermi* Gamma-ray Telescope** is a space mission working in the high energy range between 10 keV and 300 GeV, (Atwood et al., 2009). It is a space observatory being used to perform γ-ray astronomy observations from low Earth orbit. In Fig. 4.7 a reconstructed image of *Fermi* is shown. The main instrument is the **Large Area Telescope (LAT)** with the aim to study transient phenomena. The other instrument is Gamma-ray Burst Monitor (GBM); it has a field of view several times

[9]https://www.swift.ac.uk/user_objects/

larger than the LAT and provides spectral coverage of gamma-ray bursts that extends from the lower limit of the LAT down to 10 keV. For this project it were used data from *Fermi*-LAT, an imaging γ-ray detector based on pair-conversion of photons, which detects photons with energy from 20 MeV to 300 GeV.
The key scientific objectives of the mission include: understand the mechanisms of particle acceleration in ANG and determine the high-energy behavior of GRBs and transients. In particular, it studies energy spectra and variability of wavelengths of light coming from blazars to determine the composition of the jets.

Figure 4.7: The *Fermi* Gamma-ray Telescope, space observatory in low Earth orbit. From Fermi-LAT web page[10].

Fermi-LAT light curve data are free to access from the dedicated repository[11] (retrieved in April 2024). The resulting light curve is plotted in Fig. 4.8.
Fermi is a full sky survey mission, sweeping its field of view over the entire sky every three hours (every two orbits, ∼90 min each), (Carson, 2007). Nevertheless, for this characteristic in order to build a significant signal data have to be integrated over a time window (at least 3-days), resulting then in an averaging of variability properties of the source on a shorter timescale. In this case, the variability is an intermediate state between the long time saw in radio and optical band and the short time present in X-rays. The source PKS 1424+240 was observed by *Fermi*-LAT during the same week of March 2017.

[10] https://fermi.gsfc.nasa.gov/science/instruments/lat.html
[11] https://fermi.gsfc.nasa.gov/ssc/data/access/lat/LightCurveRepository/

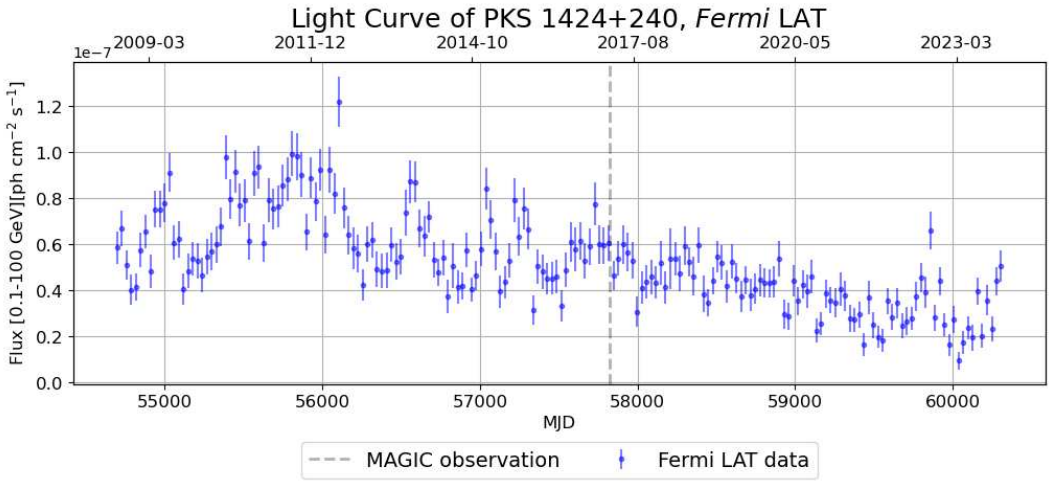

Figure 4.8: *Fermi*-LAT light curve of PKS 1424+240. The high energy γ-ray data are represented by the blue dots, while the gray dashed line represents the observed nights by MAGIC. On the x-axis are displayed both MJD and UTC, lower and upper axis, respectively. The intensity of the flux is given in photons cm^{-2} s^{-1}. The flaring state is not visible due to the binning time of Fermi. Data retrieved from *Fermi*-LAT repository[12].

4.5 Very High Energy Gamma-Ray Band

Photons having energies higher than 100 GeV are defined as very high energy γ-rays, Sec. 1.2 in the first chapter. For this range of energy, the detection is only possible via indirect methods described in Sec. 1.4.1 in the first chapter.

MAGIC

The **MAGIC** telescopes are described in the second chapter The MAGIC Telescopes, where notion on hardware and software are illustrated; while the whole data analysis is present in the third chapter MAGIC analysis PKS 1424+240.
The light curve data resulting from the data analysis are displayed together with archival data in Fig. 4.9. PKS 1424+240 was studied and analyzed by Aleksić et al. (2014), in a long term study of roughly three years that include mono MAGIC data of 2009 and stereo MAGIC data of 2010-2011; and Acciari et al. (2020) including data from 2014 to 2015. The data analyzed for this thesis were triggered by *Fermi*-LAT that measures high hardness in the spectrum, and the source was observed by *Swift*-XRT in a flaring state. The result from the 9$^{\text{th}}$ March 2017 is compatible with a flaring state: $\sim 4 \times 10^{-11}$ cm^{-2} s^{-1}; while for the 10$^{\text{th}}$ March 2017 just an upper limit is available.
Similar to the X-ray band, the variability of the source seems to be fast with a daily timescale.

[12]https://fermi.gsfc.nasa.gov/ssc/data/access/lat/LightCurveRepository/

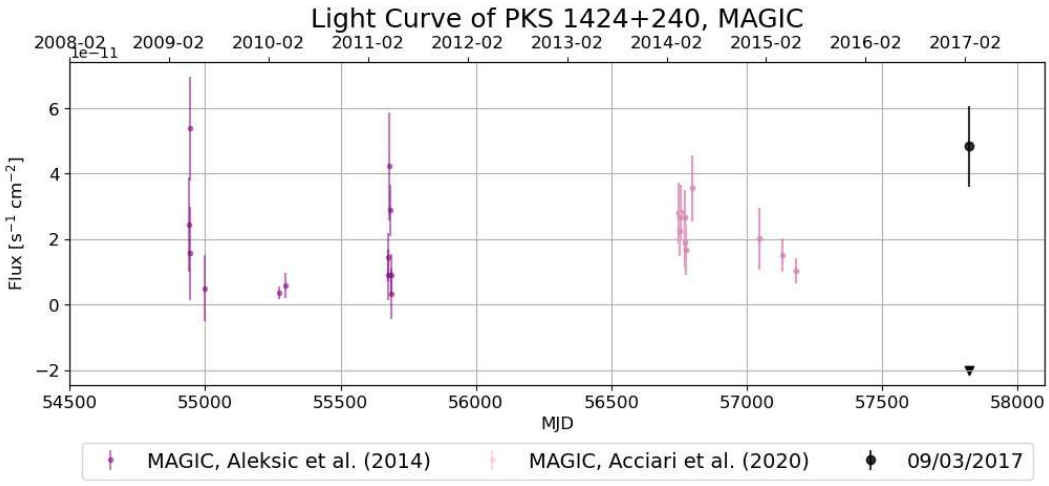

Figure 4.9: MAGIC light curve of PKS 1424+240. On the x-axis are displayed both MJD and UTC, lower and upper axis, respectively. Three set of data are displayed: purple dots are related to the study of Aleksić et al. (2014), pink dots are related to the study of Acciari et al. (2020), and finally, the black points are the result of this analysis (the upper limit is marked with a inverted triangle). The intensity of the flux is given in cm^{-2} s^{-1}.

4.6 Neutrinos

The association with neutrinos is a relevant characteristic of PKS 1424+240. This connection is important because neutrinos are messengers that can be directly linked to the hadronic interaction in the source, (Perkins, 2009). More information on neutrinos are present in Sec. 1.3 in the first chapter.

IceCube Observatory

The **IceCube** Observatory is a neutrino observatory located at the South Pole, it counts thousands of sensors that are positioned under the Antarctic ice, distributed over a cubic kilometer.
Recently the first astrophysical neutrino in association with a flaring blazar, TXS 0506+056, was detected, (Aartsen et al., 2018). After that discovery other two neutrino emitting candidates were found by performing a time integrated analysis (over ∼10 years of archival data) the Seyfert galaxy NGC 1068 and the blazar PKS 1424+240, (Aartsen et al., 2020; Abbasi et al., 2021, 2022).
In order to study the neutrino connection with PKS 1424+240, data from IceCube All-Sky Point-Source Neutrino Events Catalog[13] were retrieved (access on June 2024). The neutrino events plot, displayed in Fig. 4.10, shows the detected neutrino which arrival direction is coincident with the source position against energy. IceCube has performed several searches for point-like sources of neutrinos. The events con-

[13]https://heasarc.gsfc.nasa.gov/W3Browse/icecube/icecubepsc.html

tained in the catalog come from the 10-year time-integrated neutrino point source search, (Aartsen et al., 2020; Abbasi et al., 2021). Events in the catalog are track-like neutrino candidates detected between April 2008 and July 2018. The data contained in the release of IceCube's point source sample shows 3.3σ evidence of a cumulative excess of events from a catalog of 110 potential sources[14].
The neutrino events are almost homogeneously distributed over time, this result is expected since these data have not been filtered to sort between astrophysical and atmospheric neutrinos.

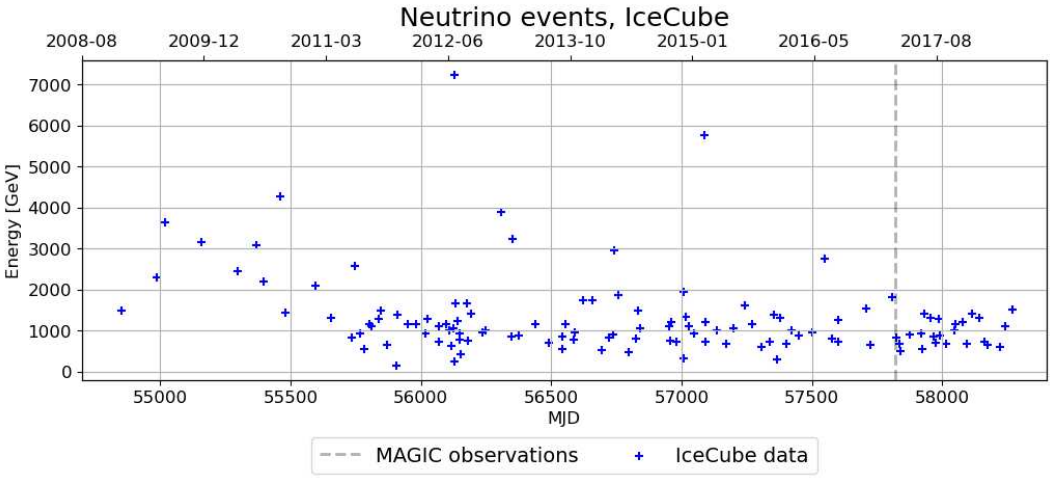

Figure 4.10: IceCube accumulation neutrino event coincident with the direction of PKS 1424+240. On the x-axis are displayed both MJD and UTC, lower and upper axis, respectively. On the y-axis is reported the energy of the detected neutrino in GeV. The neutrino events are displayed by blue cross, while he gray dashed line represents the observed nights by MAGIC. Data retrieved from IceCube repository.

4.7 Multiwavelength Light Curve

Once the analysis of the individual bands is concluded, it is time to superimpose the light curve of all energy bands in order to highlight the source's properties. Fig. 4.11 represents exactly this superimposition of light curves. Each panel is related to a specific energy band and instrument, the energies shown in the plot are increasing from the top to the bottom panel. The first is the OVRO light curve representing the radio band at 15 GHz, then there is the Tuorla light curve for the optical band in R-filter; the *Swift*-XRT light curve for the X-ray band; for the γ-rays *Fermi*-LAT light curve represents high energy γ-ray, while the MAGIC light curve the VHE γ-ray above 150 GeV; lastly the IceCube panel shows the accumulated neutrino events during the past years coinciding with the position of PKS 1424+240. All the data shown in the plot are daily binned, except *Fermi*-LAT, that is weekly binned.

[14]https://icecube.wisc.edu/data-releases/2021/01/all-sky-point-source-icecube-data-years-2008-2018/

In order to do a correct interpretation of the multiwavelength light curve, the concept of **fractional variability** can be used. This tool is described in the next section, Sec. 4.7.1.

4.7.1 Fractional Variability

Extreme time variability is a typical feature of blazars, it can be of order of minutes up to years. The **fractional variability** is a parameter used to investigate the degree of variability of light curve. In general, the variance is used to quantify the intensity of the variability of a given data set. For the specific case of blazar the sample is the light curve with its relative error, (Schleicher et al., 2019).
To define the fractional variability, few tools are needed, such as the variance, (Schleicher et al., 2019):

$$S^2 = \frac{\sum_{i=1}^{N}(\langle x\rangle - x_i)^2}{N-1}, \tag{4.2}$$

where N is the number of data points x_i and $\langle x\rangle$ is the mean of the data set.
Then the mean square error is defined as, (Schleicher et al., 2019):

$$\langle\sigma_{err}^2\rangle = \frac{1}{N}\sum_{i=1}^{N}\sigma_{err,i}^2, \tag{4.3}$$

where $\sigma_{err,i}^2$ are the measurement uncertainties.
And the normalized excess variance reads, (Schleicher et al., 2019):

$$\sigma_{\mathrm{NXS}}^2 = \frac{S^2 - \langle\sigma_{err}^2\rangle}{\langle x\rangle^2}. \tag{4.4}$$

Finally, the fractional variability is given by the square root of the normalized excess variance, (Schleicher et al., 2019):

$$\mathrm{F_{var}} = \sqrt{\sigma_{\mathrm{NXS}}^2} = \sqrt{\frac{S^2 - \langle\sigma_{err}^2\rangle}{\langle x\rangle^2}}. \tag{4.5}$$

Then the uncertainty of the fractional variability is given by, (Schleicher et al., 2019):

$$\Delta\mathrm{F_{var}} = \sqrt{\mathrm{F_{var}^2} + \mathrm{err}(\sigma_{\mathrm{NXS}}^2)} - \mathrm{F_{var}}, \tag{4.6}$$

where the uncertainty of the normalized excess variance:

$$\mathrm{err}(\sigma_{\mathrm{NXS}}^2) = \sqrt{\left(\sqrt{\frac{2}{N}}\frac{\langle\sigma_{err}^2\rangle}{\langle x\rangle^2}\right) + \left(\sqrt{\frac{\langle\sigma_{err}^2\rangle}{N}}\frac{2\mathrm{F_{var}}}{\langle x\rangle}\right)^2}. \tag{4.7}$$

Since the fractional variability itself does not use any timing information of the light curve, to compare the fractional variability for different bands, it is important to use the same time window and a time binning of at least the expected and studied time range of the variables, Schleicher et al. (2019). Usually, the fractional variability is

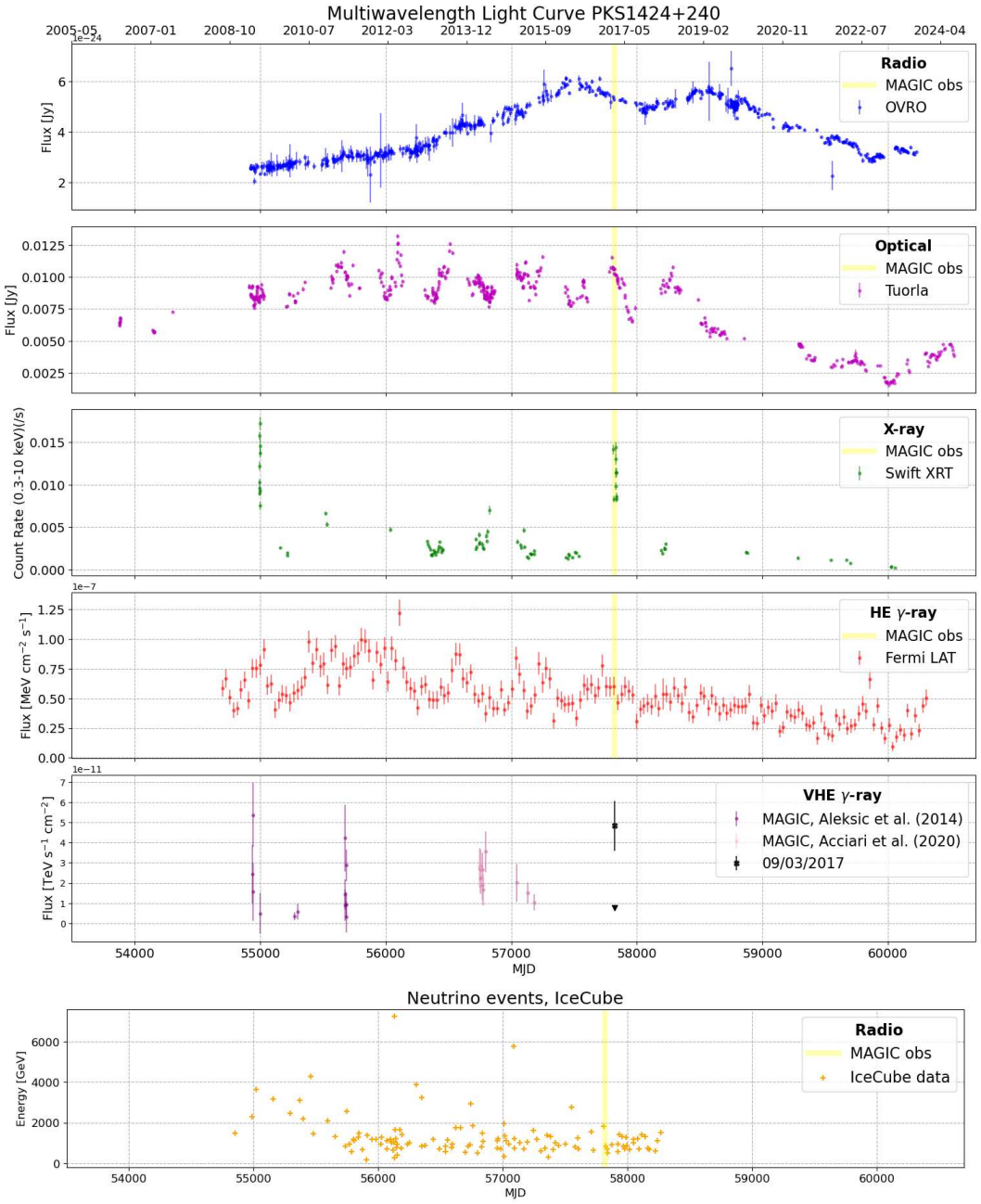

Figure 4.11: Multiwavelength light curve of PKS 1424+240 from 2009 to 2023. The single result from the multiwavelength analysis are plotted together, sharing the x-axis related to the time (MJD and UTC, both). From the top to the bottom, the energy is increasing. The top plot is the OVRO light curve (radio 15 GHz), followed by the Tuorla light curve (optical, R-filter), the *Swift*-XRT light curve (X-ray), the *Fermi*-LAT light curve (high energy γ-ray), the MAGIC light curve (very high energy γ-ray), and lastly at the bottom the IceCube neutrino events. In all panels, the observation data set analyzed in this thesis is plotted with a yellow line; in the MAGIC panel, the interested data are displayed with a black dot for distinguishing them from the archive data (purple and pink).

plotted against the frequency (or equivalently, the energy), as it is shown in Fig. 4.12.

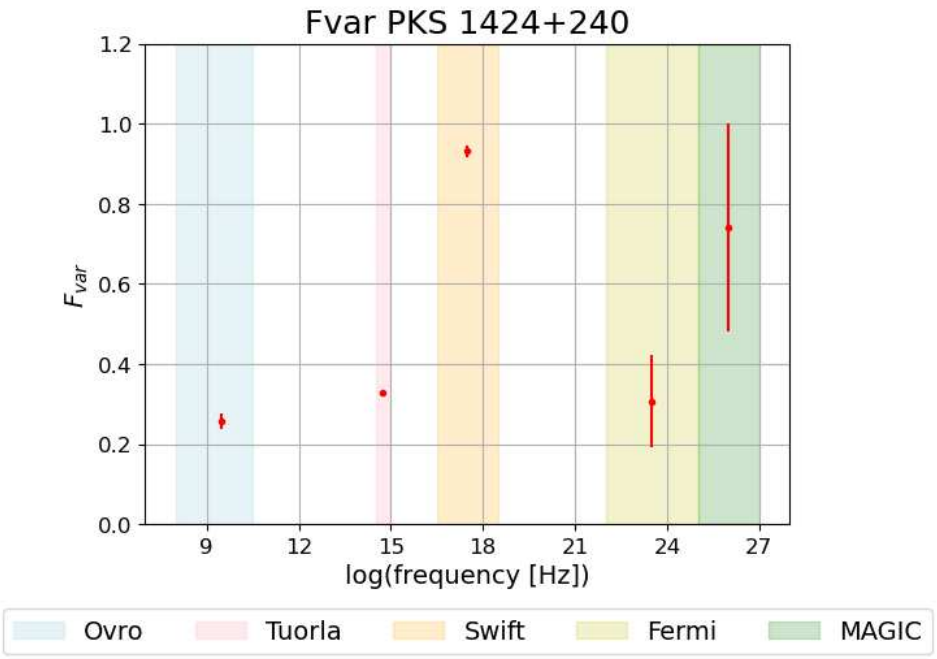

Figure 4.12: Comparison of F_{var} vs. frequency of PKS 1424+240. Data from different instrument are considered, OVRO (radio) in light blue, Tuorla (optical) in pink, *Swift*-XRT (X-ray) in orange, *Fermi*-LAT (high energy γ-ray) in yellow, and MAGIC (very high energy γ-ray) in green. The values of the F_{var} are represented by red points.

4.7.2 Multiwavelength Light Curve Interpretation

It was already mentioned the fact that blazars are very variable objects, and PKS 1424+240 is no an exception. From the multiwavelength light curve, see Fig. 4.7, the variability of the source is clearly visible. By a first interpretation of the light curve in the different bands, it is possible to say that the timescales are different.
In the radio band (OVRO 15 GHz, first panel) the source is slowly varying its flux with time, from the beginning of the observation (around 2009) the flux is increasing reaching a maximum in two peaks in ∼2016 and ∼2019, and then is slowly decreasing. Also in the optical band (Tuorla Observatory, second panel) the flux is quite steady; the flux is increasing, but the maximum is reached before the radio one (∼2013) and then decrease. The delay present is related to the geometry of the emission zone and the acceleration mechanism, (Aleksić et al., 2014). This topic is still under debate. Nevertheless, it is possible to say that the radio and the optical emission are related to the same emission zone. Another feature that confirms this hypothesis is given by the fractional variability, see Fig. 4.12, OVRO and Tuorla F_{var} value is quite similar and lower in respect the other instruments.

Instead, for the X-ray band (*Swift*-XRT, third panel) the timescale of variability is shorter, two flaring state are clearly visible during 2009 and 2017. Different from the previous two bands, the light curve presents several time gaps; the almost continuous light curve in radio and optical energies are the result of two monitoring programs (the OVRO 40m Telescope Monitoring Program and the Tuorla blazar monitoring) started in the beginning of 2000. In this case, the F_{var} value is quite higher with respect to the lower energies band above-mentioned. This difference on the timescale of the variability is possibly due to a different emitting zone.
Moving to the γ-ray band, in the high energy regime (*Fermi*-LAT, fourth panel) the timescale of the variability seems to be less evident, but it can be due to the fact that the time binning of *Fermi*-LAT is not daily binned as it is for the other experiments. Nevertheless, some variability in the light curve is still present. Another explanation can be related to the emitting zone, it was already said that radio and optical emission come from a different region from the X-ray emission, the part of the spectrum seen by *Fermi*-LAT it may be related to a mix of the two zones.
Then in the VHE γ-ray band (MAGIC $E > 150$ GeV, fifth panel), the timescale of the variability seems to be the same present in the X-ray. The source was observed flaring during the same periods. Therefore, the emission related to the VHE γ-rays very likely comes from the same zone as the X-rays.
The two-zone model for the source emission will be better explained in the next chapter, Spectral Energy Distribution modelling.

Chapter 5

Spectral Energy Distribution modelling

This chapter is dedicated to modeling the spectral energy distribution of the blazar PKS 1424+240. The results from the multiwavelength comparison are used to develop a meaningful model that accurately replicates the source's emission. A simple leptonic model was chosen for this purpose, allowing for a comparison with previous models and an assessment of whether an additional hadronic component is necessary to enhance the model's accuracy.

The **Spectral Energy Distribution (SED)** of blazars, and thus of PKS 1424+240, is characterized by a double peak shape. In general, the low energy peak, located at frequency 10^{12}-10^{15} Hz, is associated to synchrotron emission, while the high energy peak origin, located at frequency 10^{21}-10^{25} Hz, is more complex to define. The nature o the second bump can be related to **leptonic processes** or to **hadronic processes**, Longair (2011). Nonetheless, the majority of models consider only the leptonic component; this is because the hadronic interactions are more complex to model than the leptonic one, and usually hadronic processes are subdominant at parity of particle density and magnetic field.
As it was mentioned in Sec. 1.6 in the first chapter (Introduction), a peculiarity of the blazar PKS 1424+240 is the connection with neutrinos. In order to explain physically the presence of neutrino, a lepto-hadronic model should be used.
At first approximation, a leptonic model can describe the SED with good confidence level. Therefore, in this thesis the model is limited to leptonic interactions; and the main goal is to test a simple leptonic model to explain the source emission. Nevertheless, considering the SED modelling of TXS 0506+056, (Cerruti et al., 2011; Ansoldi et al., 2018; Gao et al., 2018; Petropoulou et al., 2020) the hadronic component in the emission might be subdominant; since PKS 1424+240 has a similar behavior this result can be used as a starting point.

5.1 Single-zone Models

The emission from a blazar is often attributed to a relativistic electron population that accelerates and emits radiation within a spherical region. This model is called **single-zone** (leptonic) model, and it is the more common for the SED modelling of blazars. In the single-zone model, the low-frequency component is related to *synchrotron radiation*, while the higher energy component is tied to *inverse Compton scattering*, (Boula and Mastichiadis, 2022). The Synchrotron Self Compton (SSC) is a largely used model where synchrotron radiation, emitted by high energy electrons spiraling in magnetic fields, is scattered to higher energies by the same electrons via inverse Compton scattering.
In this model, the emitting plasma is contained inside a spherical region often called **blob**, in relativistic motion that can be described with a **bulk Lorentz factor** (Γ) along the jets with an inclination angle (θ) with respect the line of sight. The relativistic effects are then described by the relativistic **Doppler factor** (δ):

$$\delta_D = \frac{1}{\Gamma(1 - \beta \cos\theta)}, \tag{5.1}$$

where β is the speed of the particle normalized over the speed of light.
Then the emitting region is immersed in a tangled magnetic field and a population of relativistic electron. The spectrum of electrons can be defined by several functions, the more used are: simple power law, power law with an exponential cut-off, broken power law, broken power law with an exponential cut-off, log-parabola.
In the simplest SSC model, in which all parameters can be free parameters and observational quantities, (Nigro, C. et al., 2022). The seven free parameters are: the blob's radius R (cm), the magnetic field strength B (G), the Lorentz factor of electrons at the spectral break, γ_b, the spectral indices before and after the break n_1 and n_2, the Doppler factor δ_D and the normalization for electron distribution N_0 (cm^{-3}). While the seven observational quantities are: the synchrotron and the inverse Compton peak frequencies $\nu_{\rm sync}$ and $\nu_{\rm IC}$, the synchrotron and inverse Compton peak fluxes $F_{\rm sync}$ and $F_{\rm IC}$, the low energy and high energy spectral indices α_1 and α_2, and the variability timescale $t_{\rm var}$, (Maraschi et al., 1992; Ghisellini and Tavecchio, 2008).
There are few fundamental equations for the single-zone model; the power emitted from the synchrotron radiation is given by, (Spurio, 2014):

$$P_{\rm sync}(\nu) \propto \nu^{\frac{1}{3}} \qquad \text{for } \nu < \nu_c \tag{5.2}$$

$$P_{\rm sync}(\nu) \propto \nu^{-\frac{p-1}{2}} \qquad \text{for } \nu > \nu_c; \tag{5.3}$$

where ν_c is the critical frequency and p is the spectral index of electron distribution. Instead, the power emitted by inverse Compton scattering is given by:

$$P_{\rm IC}(\nu) \propto \nu^{-\frac{p-1}{2}} \qquad \text{for SSC} \tag{5.4}$$

The Doppler boosting relates the observed frequency and flux and the emitted frequency and flux as:

$$\nu_{\rm obs} = \delta_D \nu_{\rm emitted} \tag{5.5}$$

$$F_{\nu_{\rm obs}} = \delta_D^3 F_{\nu_{\rm emitted}}. \tag{5.6}$$

5.2 Two-zone Models

The blazar PKS 1424+240 was modelled by Aleksić et al. (2014) and by Aartsen et al. (2020). Both studies reached the conclusion that a **two-zone** model was needed; since the SED of PKS 1424+240 has a large separation between the first and second peak, the synchrotron peak is a wide bump located around the optical regime ($\log(\nu_{\text{sync-peak}}) = 15.1 \pm 0.4$ Hz[1]), while the second peak is more uncertain but seems to be located at very high energies ($\log(\nu_{\text{sync-peak}}) \sim 24 \div 25$ Hz). This feature is difficult to model with a traditional single-zone SSC. Beside the separation of the peaks, PKS 1424+240 is a BL Lac object, meaning that the accretion disk and the BLR are weak, in this situation the external Compton model cannot be applied. Two-component models have two emitting regions that are responsible for the observed radiation. There exist evidence for the connected origin of X-ray and VHE γ-ray for HBL BL Lacs objects, the two band usually show correlations, (Acciari et al., 2011; Aleksić et al., 2015). While the other component is the one that dominates in radio and optical bands.
The electron density is defined as a smoothed broken power law, (Aleksić et al., 2014; Acciari et al., 2020):

$$N(\gamma) = K\gamma^{-n_1}\left(1 + \frac{\gamma}{\gamma_b}\right)^{n_1 - n_2}; \tag{5.7}$$

where K is a normalization factor, γ_b is the Lorentz factor of electrons at the spectral break, and n_1 and n_2 are the spectral indices before and after the break, respectively.

In the two-zone modelling by Aleksić et al. (2014) it was used the model presented by Tavecchio. et al. (2011) with small modifications. The two emission regions are considered separated, and the inner region is assumed to be smaller, meaning that the inner region is closer to the SMBH, or it is a spine, while the larger region is a sheath. Both regions are described by the same parameters of a single-zone model, therefore, assuming electron population distributed as a broken power law in each region, see Fig. 5.1. Fit parameters from Aleksić et al. (2014) are reported in Tab. 5.1. The high value of γ_{min} obtained is compatible with the hypothesis of shock heating, as suggested by Sironi and Spitkovsky (2011).

[1] https://firmamento.hosting.nyu.edu/data_access

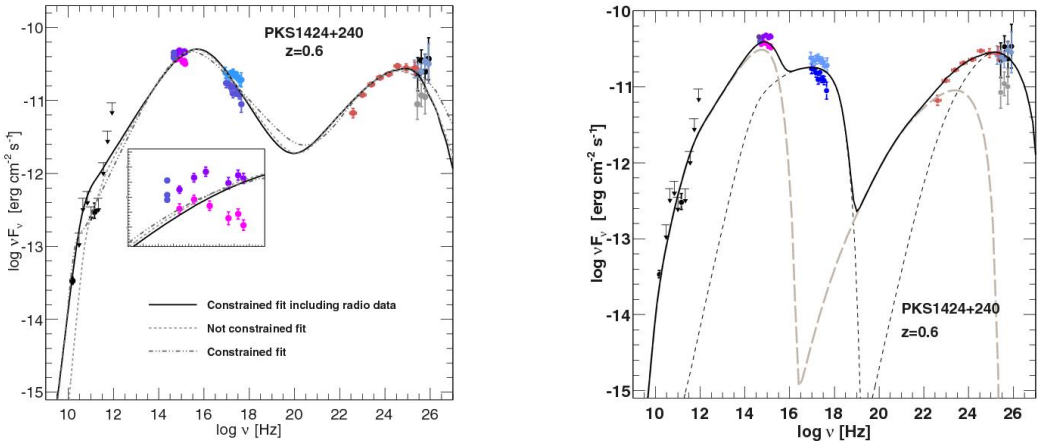

Figure 5.1: Comparison of single-zone SSC (left) and two-zone SSC (right) of PKS 1424+240 assuming a redshift of z = 0.6, by Aleksić et al. (2014). Radio data from OVRO 15 GHz (black filled circles), and Planck 857 GHz (black arrows and filled circle), optical R-band from KVA (blue filled circles), ultraviolet from *Swift*-UVOT (pink for the lowest state and purple for the highest state filled circles), X-ray from *Swift*-XRT (light blue for the high state and violet for the low state filled circles), high energy γ-ray from *Fermi*-LAT (red filled circles), and VHE γ-ray from MAGIC (2009: black, 2010: gray, 2011: light blue). The two-zone model results in more correct fit to the data, the peak of the second bump is located around 60 GeV.

The modelling by Acciari et al. (2020), based as well on the two component model by Tavecchio. et al. (2011), has similarity with the work done by Aleksić et al. (2014), however the two emission region are considered to be co-spatial and interacting to mimic a simple spine-sheath model. In this two-zone model, the two regions are called *core* and *blob*, having the core larger than the blob. The presence of a strong correlation between X-rays and VHE γ-rays bands indicates that the emissions share the same emitting region. Fit data by Acciari et al. (2020) are reported in Tab. 5.2; while the model is shown in Fig. 5.2.

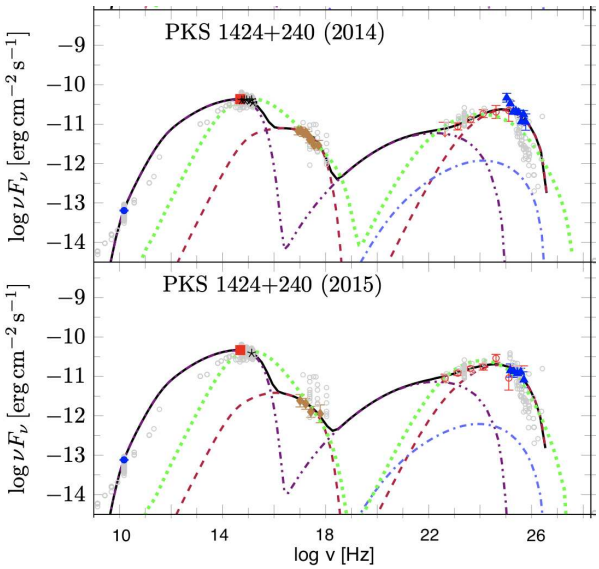

Figure 5.2: Two-zone model by Acciari et al. (2020). Archival non-simultaneous data from the ASI Space Science Data Centre, (gray open circles), radio data from OVRO 15 GHz (blue circle), optical R-band data from Tuorla (red square), optical and UV data from *Swift*-UVOT (black stars), X-ray data from *Swift*-XRT (brown diamonds), high energy γ-ray from *Fermi*-LAT (red open circles) and VHE γ-ray from MAGIC (blue triangles). The green dashed line is the single-zone fit, the black full line the two-zone fit; then the blob region is represented by a magenta dashed line, the core region by a purple dashed line and the interaction one by a blue dash-dotted line.

Model	$\gamma_{\rm min}$ [10^3]	$\gamma_{\rm b}$ [10^4]	$\gamma_{\rm max}$ [10^5]	n_1	n_2	B [G]	K [10^2 cm^{-3}]	R [10^{16}cm]	δ
Single-Zone	0.004	5.3	3.2×10^4	2.0	4.0	0.017	1.7	19	40
Two-Zone in	8.0	3.9	7.0	2.0	3.1	0.033	31	4.8	30
Two-Zone out	0.6	3.0	0.5	2.0	3.0	0.033	0.23	190	9

Table 5.1: Results by Aleksić et al. (2014), fit parameters for: single-zone model and two-zone model (divided by in region and out region). The following quantities are reported: the minimum, break, and maximum Lorentz factors ($\gamma_{\rm min}$, $\gamma_{\rm b}$, $\gamma_{\rm max}$); the low and high-energy slope of the electron energy distribution (n_1 and n_2); the magnetic field intensity B, the electron density K, the radius of the emitting region R; and the Doppler factor δ.

Year	Model	$\gamma_{\rm min}$ [10^3]	$\gamma_{\rm b}$ [10^4]	$\gamma_{\rm max}$ [10^5]	n_1	n_2	B [G]	K [10^{-3} cm^{-3}]	R [10^{15}cm]	δ
2014	one-zone	3.6	2.3	8.9	1.9	4.3	0.017	0.4	55	80
	blob	9.0	3.2	3.2	1.89	3.35	0.1	17	19	20
	core	0.35	0.3	0.28	1.69	3.0	0.1	0.007	1020	10
2015	one-zone	6.0	2.8	6.0	2.0	4.8	0.015	14	56	75
	blob	6.0	4.5	3.3	1.98	3.85	0.1	32	13.1	18
	core	0.33	0.3	0.3	1.68	3.0	0.1	0.007	1020	10

Table 5.2: Results by Acciari et al. (2020), fit parameters for: single-zone model and two-zone model (divided in blob and core regions). The following quantities are reported: the minimum, break, and maximum Lorentz factors ($\gamma_{\rm min}$, $\gamma_{\rm b}$, $\gamma_{\rm max}$); the low and high-energy slope of the electron energy distribution (n_1 and n_2); the magnetic field intensity B, the electron density K, the radius of the emitting region R; the Doppler factor δ.

5.3 SED Modelling

5.3.1 Software: `agnpy`

`agnpy`[2] is a `Python` library designed for modelling the emission from AGN, particularly focusing on leptonic models of AGN jets, (Nigro, C. et al., 2022). It focuses on the numerical computation of the photon spectra produced by particles radiative processes in jetted AGN. It is an open-source tool that allows researchers to simulate and fit the SED of AGNs by taking into account different emission processes. The package includes classes describing the galaxy components responsible for line and thermal emission, and it calculates the absorption due to $\gamma\gamma$ pair production on several photon fields.
On `agnpy` is possible to define thermal and non-thermal emitters, (Nigro, C. et al., 2022):

- `agnpy.emission_regions` describes the emission regions responsible for the non-thermal radiative processes. The emission region contains the Electron Energy Distribution (EED), the only non-thermal emission region implemented is a spherical plasmoid streaming along the jet (blob). The electron distribution is considered homogeneous and isotropic in the blob's rest frame.

- `agnpy.targets` defines line and thermal emitters, providing the photon fields target for inverse Compton scattering or $\gamma\gamma$ absorption. The implemented thermal emitters are: the CMB, a monochromatic point-like source behind the jet, a Shakura-Sunyaev accretion disc; a BLR simplified to an infinitesimally thin sphere; a dusty torus simplified to a ring that absorbs and re-emits black body radiation at fixed temperature. The thermal emission of the targets can also be computed.

[2] https://github.com/cosimoNigro/agnpy

For this thesis the model is limited to a SSC, and thus external photons defined with `agnpy.targets` are not the main focus.
Then different modules are present in order to describe the radiative processes of the emission, a limiting factor is given by the absence of fully developed hadronic process, at present time leptonic processes and the proton synchrotron are available. `agnpy.synchrotron` computes self-absorbed synchrotron spectra, assuming the electron distribution to be in a large scale random magnetic field; `agnpy.compton` characterizes the Inverse Compton with both Synchrotron Self Compton model (SSC) and External Compton (EC); lastly, `agnpy.absorption` models the $\gamma\gamma$ absorption with emission lines and other thermal emitters. Additionally, the EBL absorption can be computed with different models, namely: Domìnguez et al. (2011), Finke et al. (2010), Franceschini et al. (2008).

5.3.2 Modelling of PKS 1424+240

The starting point for the SED modelling is to try to implement the simplest possible model and then, if necessary, increase the complexity of the model. For this reason, even if the blazar has already been modelled by Aleksić et al. (2014) and Acciari et al. (2020) with a two-zone model, a simple one-zone SSC model is tested on 2017 data. The basic hypothesis is that there is only one population of electron responsible for both emission, synchrotron and SSC. For this model, the EED is described by a *broken power law* due to the peak profile of the SED. In `agnpy` the broken power law is described as follows:

$$n(\gamma) = k\Big[\Big(\frac{\gamma}{\gamma_\mathrm{b}}\Big)^{-p_1} H(\gamma; \gamma_\mathrm{min}, \gamma_b) + \Big(\frac{\gamma}{\gamma_\mathrm{b}}\Big)^{-p_2} H(\gamma; \gamma_\mathrm{max}, \gamma_b)\Big] \tag{5.8}$$

where k is a spectral normalization; p_1 and p_2 are the spectral index before and after the break, respectively; γ_min, γ_max and γ_b are respectively the minimum, maximum and breaking Lorentz factors, H is the Heaviside function, which define the first term in the interval $[\gamma_\mathrm{min}, \gamma_\mathrm{b}]$ and the second term in the interval $[\gamma_\mathrm{b}, \gamma_\mathrm{max}]$.

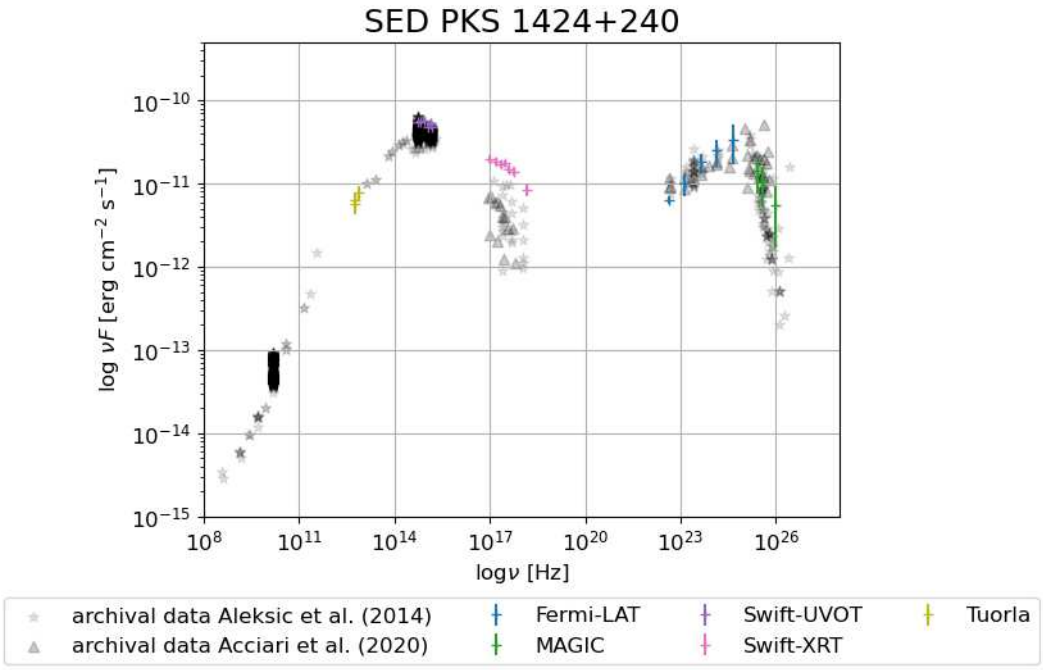

Figure 5.3: PKS 1424+240 SED relatively to the period analyzed for this thesis, March 2017. Archival data are represented by gray stars and triangles, taken from Aleksić et al. (2014) and Acciari et al. (2019, 2020). The different colors represent the different instruments involved: Tuorla (optical R-band, purple), *Swift*-UVOT (UV band, pink), *Swift*-XRT (X-ray band, yellow), *Fermi*-LAT (high energy γ-ray band, blue) and MAGIC (VHE γ-ray band, green). OVRO data are not present due to lack of simultaneity.

The SED relatively to the simultaneous and quasi-simultaneous data of March 2017 is reported in Fig. 5.3. To build the SED, data from different instruments were used, more or less the same described in the previous chapter, Multiwavelength Analysis PKS 1424+240, the main difference is the absence of OVRO due to lack of simultaneity, and the addition of *Swift*-UVOT covering the UV band. In particular, the UV data are the result of an analysis done by Dr. Cerasole; these data are simultaneous to X-ray data since XRT and UVOT are two instruments on the same *Swift* Observatory. The first difference with archival data is the higher value of the differential flux in the X-ray band observed by *Swift*-XRT; this result is in agreement with the flaring state highlighted in the light curve.
The parameters used for the model of the one-zone SSC are shown in Tab. 5.3, while the Fig. 5.4 displays the model itself. The best fit procedure is done choosing the χ^2 statistics and the Levenberg-Marquardt optimizer algorithm, (Nigro, C. et al., 2022). As it was observed by Aleksić et al. (2014), the single-zone model fails to describe correctly the SED, especially in the lower energy region (optical and UV band).

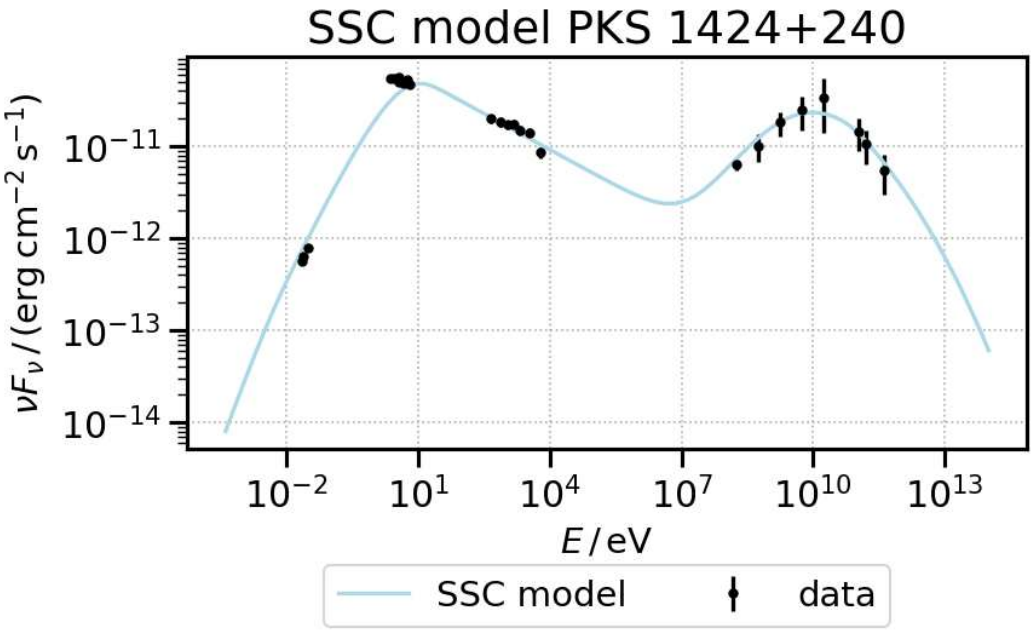

Figure 5.4: Single-zone SSC model of PKS 1424+240. The light blue line represents the fit of the SED; the black points are the quasi-simultaneous data relatively to March 2017.

Therefore, a second model used is the two-zone model; in which two different emission regions are present. The first region is responsible for the emission relatively to the low energy spectrum, meaning radio, optical and UV bands; while the second region is related to high energy, X-ray and γ-ray bands. This result arises also from the multiwavelength light curve, in which two different timescale variability were observed. More complex is the γ-ray band related to *Fermi*-LAT, the total emission may be caused by a superposition of both emission regions. Also in this case, the parameters used for the model of the two-zone are shown in Tab. 5.3, and the model is displayed in Fig. 5.5. Again, the best fit procedure is done choosing the χ^2 statistics and the Levenberg-Marquardt optimizer algorithm.

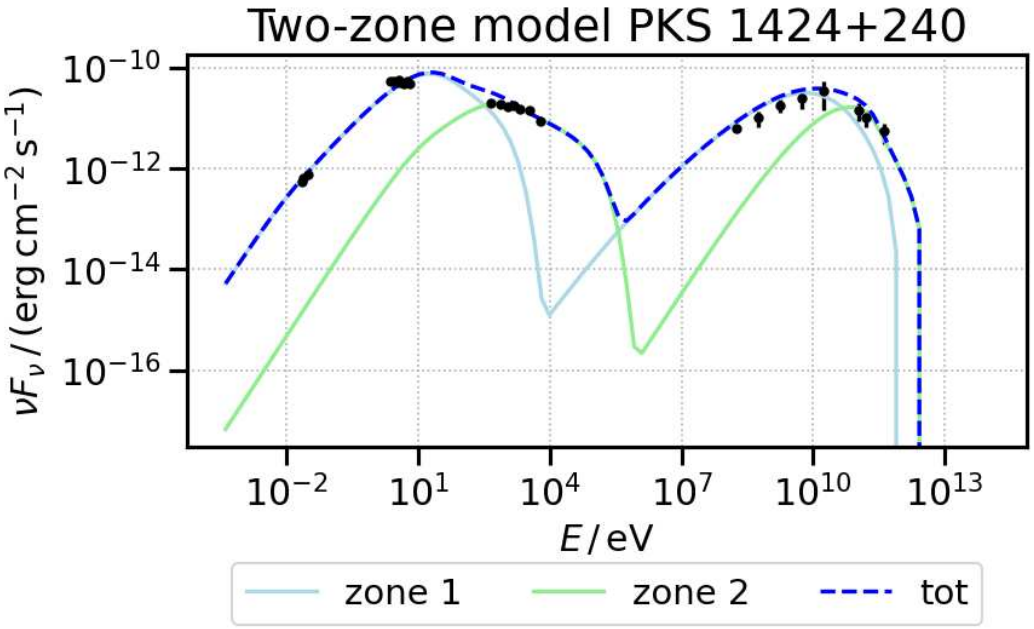

Figure 5.5: Two-zone model of PKS 1424+240. The light blue line represents the first emission zone related to the optical and UV bands, while the green line represents the second emission zone related to the X-ray and γ-ray bands, the total emission is described by the dashed blue line; the black points are the quasi-simultaneous data relatively to March 2017.

Model	$\gamma_{\rm min}$ [10^3]	$\gamma_{\rm b}$ [10^4]	$\gamma_{\rm max}$ [10^5]	n_1	n_2	B [G]	K [10^{-6} cm^{-3}]	δ
Single-Zone	0.4	1.38	10^3	1.2	3.5	0.032	3.1	42
Two-Zone (low energy)	0.5	1.46	2.0	1.1	4.2	0.2	4.7	32
Two-Zone (high energy)	10	8.12	30	1.5	3.8	0.7	1.78	12

Table 5.3: Results of fit parameters for: single-zone model and two-zone model (divided for the lower energy and high energy part of the SED). The following quantities are reported: the minimum, break, and maximum Lorentz factors ($\gamma_{\rm min}$, $\gamma_{\rm b}$, $\gamma_{\rm max}$); the low and high-energy slope of the electron energy distribution (n_1 and n_2); the magnetic field intensity B, the electron density K; and the Doppler factor δ.

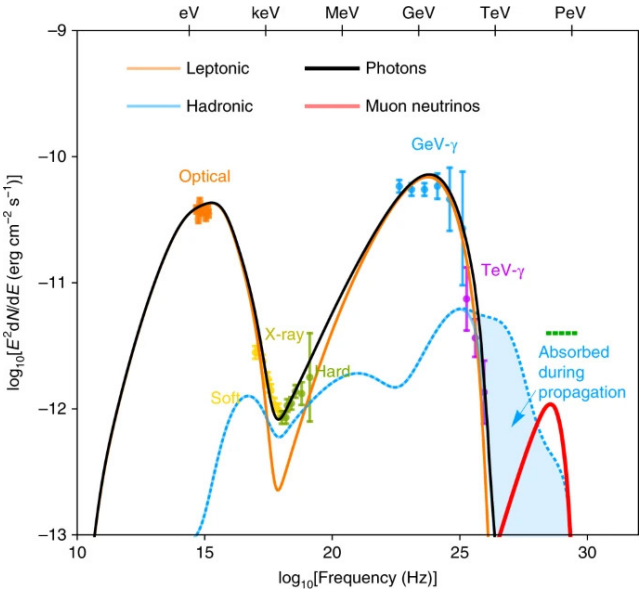

Figure 5.6: SED model of TXS 0506+056, from Gao et al. (2018). The SED is modelled using a hybrid approach that incorporates both leptonic and hadronic components. As high energy photons travel, they are absorbed by the EBL, represented by the blue shaded area. The data points represent the observed flux and spectrum during the flare event. The dashed horizontal green line marks the expected level and energy range of the incident neutrino flux to produce one muon neutrino in IceCube in 180 days.

A limit of `agnpy` is given by the possibility to include just leptonic processes and the only hadronic interaction is the proton synchrotron, but a $p\gamma$ interaction should be used in the modelling of PKS 1424+240 to explain the neutrino emission. Nevertheless, the only available open source that take into account hadronic process in the SED modelling is `AM`^{3} (Astrophysical Multi-Messenger Modelling), but the use of this code is beyond the scope of this thesis. Consequently, `agnpy` is the package used to model the SED of PKS 1424+240.
On the other hand, the hadronic component is expected to be a subdominant component with respect to the leptonic one; and this result is visible from the modelling done on the blazar TXS 0506+056 by Cerruti et al. (2011); Ansoldi et al. (2018); Gao et al. (2018); Petropoulou et al. (2020). The SED of TXS 0506+056 was modelled with a lepto-hadronic model in order to explain the correlation with the neutrino flux observed by IceCube. As it possible to see in the Fig. 5.6, the hadronic counterpart, represented by a light blue line, is subdominant. Since PKS 1424+240 and TXS 0506+056 share different similarities, it is expected from PKS 1424+240 a similar behavior and the already existent model for TXS 0506+056 can be used as starting point.
A second example of blazar modelled by including lepto-hadronic interactions is 3C279. Differently from PKS 1424+240, this object is a FSRQ (z=0.5362) and there is no evidence of neutrino emission yet. Nevertheless, in June 2015 3C279 was caught

in the brightest flare ever recorded at γ-ray energies. For this reason, the modeling of the SED was done with both leptonic and lepto-hadronic model, (Bottacini et al., 2016). In this case, the lepto-hadronic model describes accurately the SED, especially at VHE where the simple leptonic model is not fitting correctly, see Fig. 5.7 and Tab. 5.4. In quiescent states of 3C 279, leptonic models can usually reproduce the SED satisfactorily. The best fit used to model the spectrum is a log-parabola with a spectral index of 2.05 and the second peak position at $\sim 10^{22}$ Hz. Nonetheless, from the value arose from the model, see Tab. 5.4, it is clear that a lepto-hadronic model requires a higher value of the magnetic field to reconstruct correctly the SED. The magnetic field for the lepto-hadronic model is two order of magnitude larger than the one used for the leptonic model.

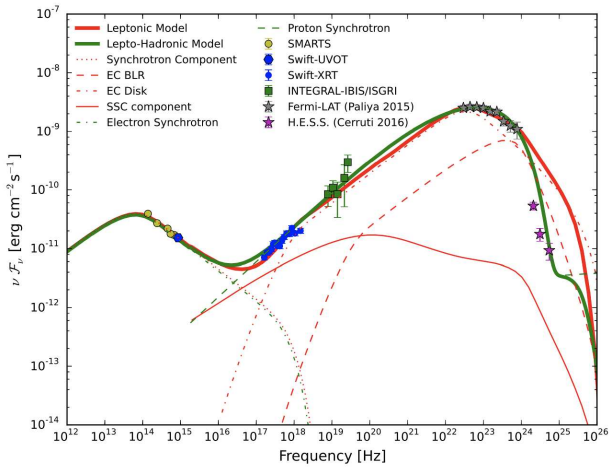

Figure 5.7: SED and models of 3C279, from Bottacini et al. (2016). Both models are displayed: the red line represents the leptonic model, while the green line the lepto-hadronic model. The major difference is related to VHE data from H.E.S.S.

Model	R [10^{16} cm]	B [G]	Γ	$\gamma_{\mathrm{min,e}}$	$\gamma_{\mathrm{max,e}}$	$\gamma_{\mathrm{min,p}}$ [GeV]	$\gamma_{\mathrm{max,p}}$ [GeV]
Leptonic	1	1	20	10^3	10^5		
Lepto-hadronic	1	100	20	10^2	10^4	10^3	6×10^6

Table 5.4: Results of fit parameters for 3C279, from Bottacini et al. (2016). The following quantities are reported: the model (leptonic and lepto-hadronic), the radius of the emitting region (R), the magnetic field (B), the bulk Lorentz factor (Γ), the minimum and maximum Lorentz factors for the electron distribution ($\gamma_{\mathrm{min,e}}$, $\gamma_{\mathrm{max,e}}$) and low and high-energy cut-offs of the proton spectrum in GeV ($\gamma_{\mathrm{min,p}}$, $\gamma_{\mathrm{max,p}}$).

Chapter 6

Conclusions

In this thesis, the blazar PKS 1424+240 was studied. This object is a BL Lac, a particular type of jetted AGN, whose jet is pointed toward the observer with a small angle with respect to the line of sight. PKS 1424+240 is located at redshift z=0.603, and it is classified as HBL, having the synchrotron peak position at $\sim 10^{15}$ Hz. This object was proposed as an extragalactic candidate for the emission of astrophysical neutrino by the IceCube Observatory, with a local significance of 3.7σ, making it the second most significant neutrino candidate source in the Northern sky, after the Seyfert galaxy NGC 1068 (4.2σ) and before the blazar TXS 0506+056 (3.5σ). Additionally, it shares several similarities with TXS 0506+056, which is responsible for the first extragalactic astrophysical neutrino association.

The MAGIC telescopes observed PKS 1424+240 at VHE in 2009, 2010, 2011, 2014 and 2015 and in the Spring 2017 the observation was triggered by the *Fermi* Gamma-ray Telescope, which detected a high value in the hardness of the spectrum, meaning a possible flaring state. Therefore, in this thesis MAGIC data of March 2017 were analyzed, following a standard MAGIC analysis, in order to check and confirm the enhanced state. From the comparison of archival MAGIC data, 2017 VHE emission is in agreement with a flare.

The flare was lately confirmed from the multiwavelength analysis. To properly characterize the behavior of PKS 1424+240 multiwavelength data were collected and a multiwavelength light curve was built. These data cover most of the electromagnetic spectrum, from radio up to VHE γ rays. Radio and optical data were a courtesy of the OVRO telescope, and the Tuorla Observatory, respectively; while X-ray and high energy γ-ray data are free to access from the repository of *Swift*-XRT and *Fermi*-LAT, respectively. Additionally, the neutrino events were also considered, these data are free to access from the IceCube repository. VHE γ-ray data arise from the analysis done for this thesis. The flare was evident in the X-ray and in the VHE γ-ray (MAGIC; $E > 100$ GeV) bands; it was not visible in the high energy γ-ray band since the binning time of the instrument, *Fermi*-LAT has minimum of 3-day binning, therefore the resulting flux is an averaged value. From the multiwavelength light curve and from the fractional variability arise that two different zones are re-

sponsible for the emission, one for the radio and optical bands, and another one for X-ray and γ-ray bands. This result was then used for the SED modelling.

To model the SED, simultaneous or quasi-simultaneous multiwavelength data are required. In order to confirm the need to use a two-zone model, as it was done in previous studies, a single-zone model was first applied. Then, since the fit was unsatisfactory and considering the results of the multiwavelength analysis, a two-zone model was used. This type of model associates the emission of the source to two different regions, one region is responsible for the emission in radio, optical and UV bands, and a second region is responsible for the emission in X-ray and γ-ray bands. The two-zone model was more in agreement with the SED data of PKS 1424+240. Both models were done by considering exclusively leptonic interaction, as the majority of model present in literature. The leptonic model is largely used, and offers better statistical performance compared to the lepto-hadronic model when applied to the same data set. Additionally, lepto-hadronic interaction are more complex since the large number of particles to take into account and the several processes to consider.
At the same time, PKS 1424+240 is a candidate for neutrino emission, and this cannot be explained by leptonic processes only. The particle content in the relativist jets is one of the open question related to blazar. Future model should consider lepto-hadronic processes to correctly describe the neutrino content. At the moment, open source software are limited to leptonic model, and as it was observed in the modelling of TXS 0506+056 the hadronic component might be subdominant with respect to the leptonic component under equivalent conditions, namely magnetic field and distribution density. This also arises from other blazars in which the hadronic model was attempted, the magnetic field was a hundred times stronger than the leptonic case.

In conclusion, PKS 1424+240 is an interesting source due to its characteristics, especially the distance and the possible neutrino connection. The MAGIC telescopes observed this blazar in more recent times, when the first telescope of the north CTAO, LST (Large Size Telescope, La Palma, Canary Island) was active. Stereoscopic data from MAGIC+LST can achieve more resolution in the lower part of VHE γ rays. The next generation of IACTs, started with LST, will achieve new results for a better comprehension of this blazar that has not been studied in detail as the other neutrino candidates, namely the Seyfert galaxy NGC 1068 and the blazar TXS 0506+056.

Acknowledgements

This research has made use of data from the OVRO 40-m monitoring program, (Richards et al., 2011), supported by private funding from the California Institute of Technology and the Max Planck Institute for Radio Astronomy, and by NASA grants NNX08AW31G, NNX11A043G, and NNX14AQ89G and NSF grants AST-0808050 and AST- 1109911.

The Tuorla Observatory blazar monitoring team is acknowledged for allowing the use of observational data reported in Tuorla Observatory blazar monitoring[1].

The Swift team is acknowledged for allowing the use of observational data reported in The Swift Observatory[2].

The Fermi team is acknowledged for allowing the use of observational data reported in Fermi LAT Light Curve Repository[3].

The MAGIC Collaboration is acknowledged for allowing the use of proprietary observational data. MAGIC results presented in this thesis have not undergone the internal review procedure of MAGIC publications.

The IceCube Collaboration is acknowledged for allowing the use of observational data reported in All-sky point-source IceCube data[4].

Dr. Davide Cerasole (INFN, University of Bari) is acknowledged for the analysis done on the *Swift* and *Fermi* data, and for the crosscheck analysis on MAGIC data.

[1] https://users.utu.fi/kani/1m/

[2] https://www.swift.ac.uk/user_objects/

[3] https://fermi.gsfc.nasa.gov/ssc/data/access/lat/LightCurveRepository/

[4] https://icecube.wisc.edu/data-releases/2021/01/all-sky-point-source-icecube-data-years-2008-2018/

Vorrei utilizzare l'ultime righe di questa tesi per ringraziare tutte le persone che in un modo o nell'altro mi hanno aiutato durante i miei anni universitari.
Ringrazio i miei genitori che pur non avendo idea di che cosa io stessi studiando mi hanno supportato e permesso di raggiungere importanti obbiettivi, anche se questo ha significato allontanarsi da casa e tornare solo ogni tanto.
Ringrazio la mia relatrice, Elisa, per essere stata sempre disponibile e per aver creduto nelle mie capacità. Ringrazio i correlatori, Giuseppe e Ilaria, per avermi spiegato con pazienza tutto quello che mi serviva. Ringrazio tutte le persone del gruppo HEAP per avermi incluso nel gruppo e avermi mostrato che cosa significa lavorare in un gruppo di ricerca. Ringrazio le compagne di ufficio e tutti i giovani della collaborazione per tutte le pause caffè e i momenti di svago che sono piú utili di quanto non si pensi.
Ringrazio tutti gli amici incontrati durante questi anni di università, chi c'è dal primo giorno e chi si è aggiunto dopo, ma è diventato velocemente importante. Le lezioni, gli esami, le pause pranzo e le serate per Padova non sarebbero state le stesse senza di voi. In particolare ringrazio la mia bella Tânia, le due scimmie Bart e Rob, e l'eccessivamente affettuoso Andrea.
In fine il più grande grazie va a JP, c'eri, ci sei e ci sarai sempre, *ik hou van je*.

Bibliography

Ave, Boyle, Gahbauer, Höppner, Hörandel, Ichimura, Müller, and Romero-Wolf. Composition of primary cosmic-ray nuclei at high energies. *The Astrophysical Journal*, 678(1):262, may 2008. doi: 10.1086/529424. URL https://dx.doi.org/10.1086/529424.

Spurio. *Particles and Astrophysics: A Multi-Messenger Approach*. Astronomy and Astrophysics Library. Springer International Publishing, 2014. ISBN 9783319080512. URL https://books.google.nl/books?id=4P67BAAAQBAJ.

Hess. Über Beobachtungen der durchdringenden Strahlung bei sieben Freiballonfahrten. *Phys. Z.*, 13:1084–1091, 1912.

Longair. *High Energy Astrophysics*. Cambridge University Press, 3 edition, 2011.

Evoli. The cosmic-ray energy spectrum, May 2023. URL https://doi.org/10.5281/zenodo.7948212.

Perkins. *Particle Astrophysics*. Oxford Master Series in Particle Physics, Astrophysics, and Cosmology. Oxford University Press, 2009. URL https://books.google.it/books?id=nI3dvwEACAAJ.

Greisen. End to the cosmic-ray spectrum? *Phys. Rev. Lett.*, 16:748–750, Apr 1966. doi: 10.1103/PhysRevLett.16.748. URL https://link.aps.org/doi/10.1103/PhysRevLett.16.748.

Kuzmin and Zatsepin. On cosmic-ray interactions with photons. *Canadian Journal of Physics*, 46(10):S617–S619, 1968. doi: 10.1139/p68-309. URL https://doi.org/10.1139/p68-309.

Rieger, Bosch-Ramon, and Duff. Fermi acceleration in astrophysical jets. In Josep M. Paredes, Olaf Reimer, and Diego F. Torres, editors, *The Multi-Messenger Approach to High-Energy Gamma-Ray Sources*, pages 119–125, Dordrecht, 2007. Springer Netherlands. ISBN 978-1-4020-6118-9.

Backes. Long-term observations of the tev blazar 1es1959+650. 06 2012. doi: 10.17877/DE290R-4809.

Rybicki and Lightman. *Radiative Processes in Astrophysics*. 1986.

Wright. Microbeam radiosurgery: An industrial perspective. *Physica Medica*, 7, 04 2015. doi: 10.1016/j.ejmp.2015.04.003.

Blumenthal and Gould. Bremsstrahlung, synchrotron radiation, and compton scattering of high-energy electrons traversing dilute gases. *Rev. Mod. Phys.*, 42:237–270, Apr 1970. doi: 10.1103/RevModPhys.42.237. URL https://link.aps.org/doi/10.1103/RevModPhys.42.237.

Ertley. Studying the polarization of hard x-ray solar flares with the gamma ray polarimeter experiment (grape). 01 2014.

Yang, Kafexhiu, and Aharonian. Exploring the shape of the -ray spectrum around the "0-bump". *Astronomy amp; Astrophysics*, 615:A108, July 2018. ISSN 1432-0746. doi: 10.1051/0004-6361/201730908. URL http://dx.doi.org/10.1051/0004-6361/201730908.

Nakamori et al. Observation of an extended very high energy gamma-ray emission from msh 15-52 with cangaroo-iii. *The Astrophysical Journal*, 677:297, 12 2008. doi: 10.1086/529029.

Kelner and Aharonian. Energy spectra of gamma rays, electrons, and neutrinos produced at interactions of relativistic protons with low energy radiation. *Phys. Rev. D*, 78:034013, Aug 2008. doi: 10.1103/PhysRevD.78.034013. URL https://link.aps.org/doi/10.1103/PhysRevD.78.034013.

Mastichiadis, Protheroe, and Kirk. Spectral and temporal signatures of ultra-relativistic protons in compact sources: I. effects of bethe-heitler pair production. *Astronomy amp; Astrophysics*, 433(3):765–776, March 2005. ISSN 1432-0746. doi: 10.1051/0004-6361:20042161. URL http://dx.doi.org/10.1051/0004-6361:20042161.

Cowan et al. Detection of the free neutrino: a confirmation. *Science*, 124(3212): 103–104, 1956. doi: 10.1126/science.124.3212.103. URL https://www.science.org/doi/abs/10.1126/science.124.3212.103.

Dass and Sarma. Neutrino oscillations and the atmospheric neutrino fluxes. *Phys. Rev. D*, 30:80–88, Jul 1984. doi: 10.1103/PhysRevD.30.80. URL https://link.aps.org/doi/10.1103/PhysRevD.30.80.

Dar, Mann, Melina, and Zajfman. Neutrino oscillations and the solar-neutrino problem. *Phys. Rev. D*, 35:3607–3620, Jun 1987. doi: 10.1103/PhysRevD.35.3607. URL https://link.aps.org/doi/10.1103/PhysRevD.35.3607.

Aartsen et al. Multimessenger observations of a flaring blazar coincident with high-energy neutrino icecube-170922a. *Science*, 361(6398), July 2018. ISSN 1095-9203. doi: 10.1126/science.aat1378. URL http://dx.doi.org/10.1126/science.aat1378.

Aartsen et al. Time-integrated neutrino source searches with 10 years of icecube data. *Phys. Rev. Lett.*, 124:051103, Feb 2020. doi: 10.1103/PhysRevLett.124.051103. URL https://link.aps.org/doi/10.1103/PhysRevLett.124.051103.

Abbasi et al. Search for multi-flare neutrino emissions in 10 yr of icecube data from a catalog of sources. *The Astrophysical Journal Letters*, 920(2):L45, oct 2021. doi: 10.3847/2041-8213/ac2c7b. URL https://dx.doi.org/10.3847/2041-8213/ac2c7b.

Abbasi et al. Evidence for neutrino emission from the nearby active galaxy ngc 1068. *Science*, 378(6619):538–543, 2022. doi: doi:10.1126/science.abg3395. URL https://www.science.org/doi/abs/10.1126/science.abg3395.

Cherenkov. Visible radiation produced by electrons moving in a medium with velocities exceeding that of light. *Phys. Rev.*, 52:378–379, Aug 1937. doi: 10.1103/PhysRev.52.378. URL https://link.aps.org/doi/10.1103/PhysRev.52.378.

de Naurois and Mazin. Ground-based detectors in very-high-energy gamma-ray astronomy. *Comptes Rendus. Physique*, 16(6–7):610–627, August 2015. ISSN 1878-1535. doi: 10.1016/j.crhy.2015.08.011. URL http://dx.doi.org/10.1016/j.crhy.2015.08.011.

Heitler. The quantum theory of radiation. 5, 1936.

López-Oramas. Multi-year campaign of the gamma-ray binary ls i +61◦ 303 and search for vhe emission from gamma-ray binary candidates with the magic telescopes. 04 2015. doi: 10.13140/RG.2.1.4140.4969.

Cao Zhen, della Volpe, and others. The large high altitude air shower observatory (lhaaso) science book (2021 edition). 2022.

Padovani, Alexander, et al. Active galactic nuclei: what's in a name? *The Astronomy and Astrophysics Review*, 25(1), August 2017. ISSN 1432-0754. doi: 10.1007/s00159-017-0102-9. URL http://dx.doi.org/10.1007/s00159-017-0102-9.

Urry and Padovani. Unified schemes for radio-loud active galactic nuclei. *Publications of the Astronomical Society of the Pacific*, 107:803, September 1995. ISSN 1538-3873. doi: 10.1086/133630. URL http://dx.doi.org/10.1086/133630.

Bonnoli, Ghisellini, Foschini, Tavecchio, and Ghirlanda. The gamma-ray brightest days of the blazars 3c454.3. 05 2010.

Bartoli, Bernardini, Bi, Bleve, Bolognino, Branchini, Budano, Melcarne, Camarri, Cao, Cardarelli, Catalanotti, Cattaneo, Chen, Chen, Chen, Creti, Cui, Dai, and Zizzi. Long-term monitoring on mrk 501 for its vhe gamma emission and a flare in october 2011. *The Astrophysical Journal*, 758, 09 2012. doi: 10.1088/0004-637X/758/1/2.

Fossati, Maraschi, Celotti, Comastri, and Ghisellini. A unifying view of the spectral energy distributions of blazars. *Monthly Notices of the Royal Astronomical Society*, 299(2):433–448, September 1998. ISSN 1365-2966. doi: 10.1046/j.1365-8711.1998.01828.x. URL http://dx.doi.org/10.1046/j.1365-8711.1998.01828.x.

Donato, Ghisellini, Tagliaferri, and Fossati. Hard x-ray properties of blazars. *Astronomy amp; Astrophysics*, 375(3):739–751, September 2001. ISSN 1432-0746. doi: 10.1051/0004-6361:20010675. URL http://dx.doi.org/10.1051/0004-6361:20010675.

Ghisellini, Righi, Costamante, Verbunt Osservatorio Astronomico di Brera, and Univ. dell'Insubria. The fermi blazar sequence. *Monthly Notices of the Royal Astronomical Society*, 469:255–266, 2017. URL https://api.semanticscholar.org/CorpusID:119236053.

Goldoni. Review of redshift values of bright AGNs with hard spectra in 4LAC catalog. April 2021. doi: 10.5281/zenodo.4721386. URL https://doi.org/10.5281/zenodo.4721386.

Condon et al. Optical identifications of Parkes sources with flat spectra. , 82:692–700, September 1977. doi: 10.1086/112109.

Impey and Tapia. New Blazars Discovered by Polarimetry. , 333:666, October 1988. doi: 10.1086/166775.

Fleming et al. Three New BL Lacertae Objects in the Palomar-Green Survey. , 106:1729, November 1993. doi: 10.1086/116760.

Acciari et al. Discovery of very high energy gamma rays from pks 1424+240 and multiwavelength constraints on its redshift. *The Astrophysical Journal*, 708(2):L100–L106, December 2009. ISSN 2041-8213. doi: 10.1088/2041-8205/708/2/l100. URL http://dx.doi.org/10.1088/2041-8205/708/2/L100.

Teshima. MAGIC observes very high energy gamma ray emission from PKS 1424 +240. *The Astronomer's Telegram*, 2098:1, June 2009.

Padovani, Boccardi, Falomo, and Giommi. Pks 1424+240: yet another masquerading bl lac object as a possible icecube neutrino source. *Monthly Notices of the Royal Astronomical Society*, 511(4):4697–4701, February 2022. ISSN 1365-2966. doi: 10.1093/mnras/stac376. URL http://dx.doi.org/10.1093/mnras/stac376.

Aleksić et al. The major upgrade of the MAGIC telescopes, Part I: The hardware improvements and the commissioning of the system. 72:61–75, 2016a. doi: 10.1016/j.astropartphys.2015.04.004",journal="Astropart.Phys.

Aleksić et al. The major upgrade of the MAGIC telescopes, Part II: A performance study using observations of the Crab Nebula. *Astropart. Phys.*, 72:76–94, 2016b. doi: 10.1016/j.astropartphys.2015.02.005.

Aleksić et al. Performance of the magic stereo system obtained with crab nebula data. *Astroparticle Physics*, 35(7):435–448, February 2012. ISSN 0927-6505. doi: 10.1016/j.astropartphys.2011.11.007. URL http://dx.doi.org/10.1016/j.astropartphys.2011.11.007.

Doro, Bastieri, et al. The reflective surface of the magic telescope. *Nuclear Instruments and Methods in Physics Research Section A: Accelerators, Spectrometers, Detectors and Associated Equipment*, 595(1):200–203, 2008. ISSN 0168-9002. doi: https://doi.org/10.1016/j.nima.2008.07.073. URL https://www.sciencedirect.com/science/article/pii/S0168900208009765. RICH 2007.

Biland, Garczarczyk, et al. The active mirror control of the magic telescope. 2007. URL https://arxiv.org/abs/0709.1574.

Borla Tridon, Goebel, et al. Performance of the camera of the magic ii telescope. 2009. URL https://arxiv.org/abs/0906.5448.

Berti. *Study of astrophysical transients with the MAGIC telescopes*. PhD thesis, Università degli Studi di Trieste, 2018. URL https://hdl.handle.net/11368/2918672.

Fruck et al. A novel lidar-based atmospheric calibration method for improving the data analysis of magic. 2014. URL https://arxiv.org/abs/1403.3591.

Bretz, Dorner, Wagner, and Sawallisch. The drive system of the major atmospheric gamma-ray imaging cherenkov telescope. *Astroparticle Physics*, 31(2):92–101, March 2009. ISSN 0927-6505. doi: 10.1016/j.astropartphys.2008.12.001. URL http://dx.doi.org/10.1016/j.astropartphys.2008.12.001.

Tescaro, López-Oramas, et al. The magic telescopes daq software and the on-the-fly online analysis client. 2013. URL https://arxiv.org/abs/1310.1565.

Fomin, Fennell, et al. New methods of atmospheric cherenkov imaging for gamma-ray astronomy. ii. the differential position method. *Astroparticle Physics*, 2(2):151–159, 1994. ISSN 0927-6505. doi: https://doi.org/10.1016/0927-6505(94)90037-X. URL https://www.sciencedirect.com/science/article/pii/092765059490037X.

López-Coto. Very-high-energy gamma-ray observations of pulsar wind nebulae and cataclysmic variable stars with magic and development of trigger systems for iacts. 01 2017. doi: 10.1007/978-3-319-44751-3.

Moralejo, Gaug, et al. Mars, the magic analysis and reconstruction software. 2009. URL https://arxiv.org/abs/0907.0943.

Majumdar, Moralejo, Bigongiari, Blanch, and Sobczynska. Monte Carlo simulation for the MAGIC telescope. 8 2005.

Heck, Knapp, Capdevielle, Schatz, and Thouw. CORSIKA: A Monte Carlo code to simulate extensive air showers. 2 1998.

Mirzoyan. On the Calibration Accuracy of Light Sensors in Atmospheric Cherenkov Fluorescence and Neutrino Experiments. 7:265, January 1997.

Aliu et al. Improving the performance of the single-dish cherenkov telescope magic through the use of signal timing. *Astroparticle Physics*, 30(6):293–305, January 2009. ISSN 0927-6505. doi: 10.1016/j.astropartphys.2008.10.003. URL `http://dx.doi.org/10.1016/j.astropartphys.2008.10.003`.

D. Garrido-Terrats. Limits to the violation of lorentz invariance using the emission of the crab pulsar at tev energies, discovered with archival data from the magic telescopes. *Universitat Autònoma de Barcelona. Departament de Física, PhD thesis*, 2015.

A. M. Hillas. Cerenkov Light Images of EAS Produced by Primary Gamma Rays and by Nuclei. In Jones, editor, *19th International Cosmic Ray Conference (ICRC19), Volume 3*, volume 3 of *International Cosmic Ray Conference*, page 445, August 1985.

Albert et al. Implementation of the random forest method for the imaging atmospheric cherenkov telescope magic. *Nuclear Instruments and Methods in Physics Research Section A: Accelerators, Spectrometers, Detectors and Associated Equipment*, 588(3):424–432, April 2008. ISSN 0168-9002. doi: 10.1016/j.nima.2007.11.068. URL `http://dx.doi.org/10.1016/j.nima.2007.11.068`.

Catalano, Leise, and Pfaff. Measuring resource inequality: The gini coefficient. *Numeracy*, 2, 07 2009. doi: 10.5038/1936-4660.2.2.4.

Li and Ma. Analysis methods for results in gamma-ray astronomy., September 1983.

A. N. Tikhonov and V. Y. Arsenin. Solutions of ill-posed problems. pages xiii+258, 1977. Translated from the Russian, Preface by translation editor Fritz John, Scripta Series in Mathematics.

Schmelling. The method of reduced cross-entropy a general approach to unfold probability distributions. *Nuclear Instruments and Methods in Physics Research Section A: Accelerators, Spectrometers, Detectors and Associated Equipment*, 340(2):400–412, 1994. ISSN 0168-9002. doi: https://doi.org/10.1016/0168-9002(94)90119-8. URL `https://www.sciencedirect.com/science/article/pii/0168900294901198`.

M. Bertero and de C. Mol. Iii super-resolution by data inversion, 1996. ISSN 0079-6638. URL `https://www.sciencedirect.com/science/article/pii/S0079663808703147`.

Domìnguez et al. Extragalactic background light inferred from AEGIS galaxy-SED-type fractions. , 410(4):2556–2578, February 2011. doi: 10.1111/j.1365-2966.2010.17631.x.

Aleksić et al. Magic long-term study of the distant tev blazar pks 1424+240 in a multiwavelength context. *AA*, 567:A135, 2014. doi: 10.1051/0004-6361/201423364. URL https://doi.org/10.1051/0004-6361/201423364.

Acciari et al. Measurement of the extragalactic background light using MAGIC and Fermi-LAT gamma-ray observations of blazars up to z = 1. , 486(3):4233–4251, July 2019. doi: 10.1093/mnras/stz943.

Acciari et al. Testing two-component models on very high-energy gamma-ray-emitting bl lac objects. *AA*, 640:A132, 2020. doi: 10.1051/0004-6361/202037811. URL https://doi.org/10.1051/0004-6361/202037811.

Schwab and Fischer. Maxwell, hertz, and german radio-wave history. *Proceedings of the IEEE*, 86(7):1312–1318, 1998. doi: 10.1109/5.681365.

Jansky. Electrical disturbances apparently of extraterrestrial origin. *Proceedings of the Institute of Radio Engineers*, 21(10):1387–1398, 1933. doi: 10.1109/JRPROC.1933.227458.

Smith. Astrophysical techniques, sixth edition, by c.r.kitchin. *Contemporary Physics*, 55, 10 2014. doi: 10.1080/00107514.2014.948932.

Tawalbeh and Al-Wardat. *Modified Orbital Elements of The Close Visual Binary Systems Hip11352, Hip70973, and Hip72479*. PhD thesis, 05 2018.

Arnaud, Smith, and Siemiginowska. *Handbook of X-ray Astronomy*. Cambridge Observing Handbooks for Research Astronomers. Cambridge University Press, 2011.

Röntgen. On a new kind of rays. *Science*, 3(59):227–231, 1896. doi: 10.1126/science.3.59.227. URL https://www.science.org/doi/abs/10.1126/science.3.59.227.

David N. Burrows et al. Swift X-Ray Telescope. In Flanagan and Oswald, editors, *X-Ray and Gamma-Ray Instrumentation for Astronomy XI*, volume 4140, pages 64 – 75. International Society for Optics and Photonics, SPIE, 2000. doi: 10.1117/12.409158. URL https://doi.org/10.1117/12.409158.

Atwood et al. The large area telescope on the fermi gamma-ray space telescope mission. *The Astrophysical Journal*, 697(2):1071, may 2009. doi: 10.1088/0004-637X/697/2/1071. URL https://dx.doi.org/10.1088/0004-637X/697/2/1071.

Carson. Glast: physics goals and instrument status. *Journal of Physics: Conference Series*, 60:115–118, March 2007. ISSN 1742-6596. doi: 10.1088/1742-6596/60/1/020. URL http://dx.doi.org/10.1088/1742-6596/60/1/020.

Schleicher et al. Fractional Variability—A Tool to Study Blazar Variability. *Galaxies*, 7(2):62, May 2019. doi: 10.3390/galaxies7020062.

Matteo Cerruti, Andreas Zech, Catherine Boisson, and Susumu Inoue. Lepto-hadronic modelling of blazar emission, 2011. URL https://arxiv.org/abs/1111.0557.

Ansoldi, Antonelli, Arcaro, et al. The Blazar TXS 0506+056 Associated with a High-energy Neutrino: Insights into Extragalactic Jets and Cosmic-Ray Acceleration. , 863(1):L10, August 2018. doi: 10.3847/2041-8213/aad083.

Gao, Fedynitch, Winter, and Pohl. Modelling the coincident observation of a high-energy neutrino and a bright blazar flare. *Nature Astronomy*, 3(1):88–92, November 2018. ISSN 2397-3366. doi: 10.1038/s41550-018-0610-1. URL http://dx.doi.org/10.1038/s41550-018-0610-1.

Petropoulou, Murase, Santander, et al. Multi-epoch modeling of txs 0506+056 and implications for long-term high-energy neutrino emission. *The Astrophysical Journal*, 891(2):115, mar 2020. doi: 10.3847/1538-4357/ab76d0. URL https://dx.doi.org/10.3847/1538-4357/ab76d0.

Boula and Mastichiadis. Expanding one-zone model for blazar emission. *AA*, 657: A20, 2022. doi: 10.1051/0004-6361/202142126. URL https://doi.org/10.1051/0004-6361/202142126.

Nigro, C., Sitarek, J., Gliwny, P., Sanchez, D., Tramacere, A., and Craig, M. agnpy: An open-source python package modelling the radiative processes of jetted active galactic nuclei. *AA*, 660:A18, 2022. doi: 10.1051/0004-6361/202142000. URL https://doi.org/10.1051/0004-6361/202142000.

L. Maraschi, G. Ghisellini, and A. Celotti. A jet model for the gamma-ray emitting blazar 3C 279. *Astrophys. J. Lett.*, 397:L5–L9, 1992. doi: 10.1086/186531.

Ghisellini and Tavecchio. The blazar sequence: a new perspective. *Monthly Notices of the Royal Astronomical Society*, 387(4):1669–1680, 07 2008. ISSN 0035-8711. doi: 10.1111/j.1365-2966.2008.13360.x. URL https://doi.org/10.1111/j.1365-2966.2008.13360.x.

Acciari et al. TeV and Multi-wavelength Observations of Mrk 421 in 2006-2008. , 738(1):25, September 2011. doi: 10.1088/0004-637X/738/1/25.

Aleksić et al. The 2009 multiwavelength campaign on Mrk 421: Variability and correlation studies. , 576:A126, April 2015. doi: 10.1051/0004-6361/201424216.

Tavecchio., Becerra-Gonzalez, Ghisellini, Stamerra, Bonnoli, Foschini, and Maraschi. On the origin of the γ-ray emission from the flaring blazar PKS 1222+216. , 534: A86, October 2011. doi: 10.1051/0004-6361/201117204.

Lorenzo Sironi and Anatoly Spitkovsky. Acceleration of particles at the termination shock of a relativistic striped wind. *The Astrophysical Journal*, 741(1):39, oct 2011. doi: 10.1088/0004-637X/741/1/39. URL https://dx.doi.org/10.1088/0004-637X/741/1/39.

Finke, Razzaque, and Dermer. Modeling the Extragalactic Background Light from Stars and Dust. , 712(1):238–249, March 2010. doi: 10.1088/0004-637X/712/1/238.

Franceschini, Rodighiero, and Vaccari. Extragalactic optical-infrared background radiation, its time evolution and the cosmic photon-photon opacity. , 487(3): 837–852, September 2008. doi: 10.1051/0004-6361:200809691.

Bottacini, Böttcher, Pian, and Collmar. 3C 279 in Outburst in 2015 June: A Broadband SED Study Based on the INTEGRAL Detection. , 832(1):17, November 2016. doi: 10.3847/0004-637X/832/1/17.

Richards, Max-Moerbeck, Pavlidou, et al. Blazars in the fermi era: The ovro 40 m telescope monitoring program. *The Astrophysical Journal Supplement Series*, 194 (2):29, may 2011. doi: 10.1088/0067-0049/194/2/29. URL `https://dx.doi.org/10.1088/0067-0049/194/2/29`.